ELECTRONIC AND MAGNETIC PHENOMENA OF INORGANIC AND ORGANIC LOW-DIMENSIONAL SOLIDS

By

BRIAN HOWARD WARD

A DISSERTATION PRESENTED TO THE GRADUATE SCHOOL
OF THE UNIVERSITY OF FLORIDA IN PARTIAL FULFILLMENT
OF THE REQUIREMENTS FOR THE DEGREE OF
DOCTOR OF PHILOSOPHY

UNIVERSITY OF FLORIDA

1997

To My Parents.

ACKNOWLEDGMENTS

I would like to thank my research advisor Dr. Daniel Talham for his suuport and guidance during my time here at the University of Florida. Many things have changed since I first arrived in Gainesville back in August 1992. Even through the most difficult times Dan Talham encouraged me to press on. Most importantly, I have learned from him how to approach research problems and formulate strategies which will result in a final product. I am also thankful to my Ph.D. committee member, Dr. Mark Meisel, for performing the magnetic susceptibility measurements on my materials, as well as the many insightful conversations on conduction and magnetism in solids. I am also grateful to Dr. Khalil Abboud for determining the X-ray structures of my compounds and for sitting on my Ph.D. committee. I am also thankful for his helpful discussions pertaining to crystallography as well as the countless times I have received his help when doing CSD searches and drawing crystal structure figures. I would like to thank the other members of my Ph.D. committee Dr. Gus Palenik and Dr. John Reynolds for their helpful comments at my oral examination and annual seminars. Also, I would like to thank Dr. Palenik for his insightful discussions concerning the chemistry presented in chapter 3 of this dissertation.

I must thank my high school chemistry teacher Ken Phillips who first sparked my interest in chemistry with his unique teaching style. I am also thankful to my undergraduate research adivsor Dr. Ken Goldsby who introduced me to research and for his enthusiasm about learning.

I would like to thank the past members of the Talham research group Drs. Houston Byrd, Scott Whipps, Liang-Keui Chou, and Candace Seip for their friendships while I was here. I would like to thank Gail Fanucci for her help in writing programs to fit data and her help running the high-field EPR in Tallahassee. Also I would like to thank her for the many conversations about research as well as being a good friend. I am grateful to Missy Petruska for her insights regarding the synthesis of organic compounds as well as synthesizing one of the molecules used. I would like to thank Garrett Granroth, a fellow graduate student in physics, for performing all of the transport measurments on my materials as well as helpful discussions on the attachment of wires to samples, conduction, and magnetism.

I want to give special recognition to my parents John and Dorothy Daniels and John and Eva Ward. They have shown me constant love, support, and encouragement throughout my entire life, no matter what the circumstances. I love all of them very dearly, and without them, I would not have made it this far.

TABLE OF CONTENTS

ACKNOWLEDGMENTS iii

ABSTRACT vii

CHAPTERS

1 BACKGROUND AND INTRODUCTION 1

Low-Dimensional Heisenberg Antiferromagnetic Materials 5
 Non-Integer Spin Systems 8
 Integer Spin Systems and the Haldane Gap Theory 10
 Haldane Gap Materials 13
Organic Conductors 18
 Early Organic Charge-Transfer Salts 18
 The TMTSF Conductors 22
 The BEDT-TTF Family of Conductors 23
 1:1 Cation-Radical Salts of the Donor BEDT-TTF 27
 Cation-Radical Salts Based on the Donor BEDO-TTF 31
Scope of Dissertation 34

2 SYNTHESIS, STRUCTURE, AND MAGNETISM OF MANGANESE (III) $S = 2$ HEISENBERG QUASI-LINEAR CHAIN ANTIFERROMAGNETS 36

Introduction 36
Experimental 39
Results and Discussion 44
 Synthesis of $[MnCl_3(bpy)]_n$ **(4)** 44
 Magnetic Data for **(4)** 46
 Synthesis and Structure of $[MnCl_3(phen)]_n$ **(5)** 53
 Static Susceptibility Data for **(5)** 55
 Synthesis and Structure of $MnCl_3(dmbpy){\cdot}CH_3CN$ **(6)** 63
Summary 68

3 NEW BEDT-TTF CATION-RADICAL SALTS INCORPORATING THE HYDROGEN DICHLORIDE ANION, α'-(BEDT-TTF)$_2$HCl$_2$, ε-(BEDT-TTF)HCl$_2$, AND ε'-(BEDT-TTF)HCl$_2$ 71

Introduction 71
Experimental 73
Results and Discussion 75
 Synthesis of α'-(BEDT-TTF)$_2$HCl$_2$ **(9)** and ε-(BEDT-TTF)HCl$_2$ **(10)** 75
 Crystal Structure of **(9)** 77
 Transport Properties of **(9)** 83

Magnetic Susceptibility Data for (9)....83
Crystal Structure of (10)....94
Magnetic Properties of (10)....94
Crystal Structure of ε'-(BEDT-TTF)HCl_2 (11)....96
Description of the HCl_2^- Anion....99
Summary....103

4 A NEW ORGANIC METAL BASED ON THE ORGANIC DONOR BEDO-TTF AND THE N, N', N"-TRICYANOGUANIDINATE DIANION, (BEDO-TTF)$_4$[C_4N_6]·H_2O....105

Introduction....105
Experimental....107
Results and Discussion....110
Synthesis and Structure of (BEDO-TTF)$_4$[C_4N_6]·H_2O (14)....110
Transport Properties of (14)....116
Tunnel Diode Oscillator Results for (14)....119
EPR Results for (14)....120
Magnetic Susceptibility Data for (14)....131
Nature of the Metal-to-Insulator transition in (14)....134
Summary....137

5 A NEW SALT OF THE ORGANIC DONOR BEDT-TTF INCORPORATING THE FERROCYANIDE ANION, β"-(BEDT-TTF)$_4$[Fe(CN)$_6$]·$2CH_2Cl_2$....139

Introduction....139
Experimental....142
Results and Discussion....145
Synthesis and Structure of β"-(BEDT-TTF)$_4$[Fe(CN)$_6$]·$2CH_2Cl_2$ (15)....145
Transport Properties of (15)....149
EPR Properties of (15)....154
Magnetic Susceptibility Results on (15)....162
Summary....166

APPENDIX....167
TABLES OF CRYSTALLOGRAPHIC DATA....168

LIST OF REFERENCES....204

BIOGRAPHICAL SKETCH....212

Abstract of Dissertation Presented to the Graduate School
of the University of Florida in Partial Fulfillment of the
Requirements for the Degree of Doctor of Philosophy

ELECTRONIC AND MAGNETIC PHENOMENA OF INORGANIC AND ORGANIC LOW-DIMENSIONAL SOLIDS

By

Brian Howard Ward

December, 1997

Chairman: Daniel R. Talham
Major Department: Chemistry

This dissertation presents experimental results from the synthesis, structure determination, transport, and magnetic characterizations of two classes of low-dimensional solids. The first class of solids, one-dimensional manganese(III) quasi-linear-chain materials, and the second class of solids, conducting organic cation-radical salts are investigated. The magnetic properties of the $S = 2$ quasi-linear-chain Heisenberg antiferromagnetic system (2,2'-bipyridine)trichloromanganese(III), $[MnCl_3(bpy)]_n$, reveal the absence of long-range magnetic order down to 30 mK, with no magnetization observed until a critical magnetic field is achieved. These results are interpreted as the first evidence of Haldane gap in an $S = 2$ quasi-linear-chain antiferromagnet. The crystal structures of two Mn(III) complexes, (1,10-phenanthroline)trichloromanganese(III), $[MnCl_3(phen)]_n$, and (4,4'-dimethyl-2,2'-bipyridine)trichloromanganese(III) acetonitrile solvate, $MnCl_3(dmbpy)\cdot CH_3CN$, were determined by X-ray diffraction. The structure of $[MnCl_3(phen)]_n$ contains quasi-linear-chains of Mn(III) ions bridged by chloride anions. From the magnetic susceptibility data, $[MnCl_3(phen)]_n$ is identified as a one-dimensional Heisenberg "canted" antiferromagnet.

The structure of $MnCl_3(dmbpy)\cdot CH_3CN$ consists of five-coordinate Mn(III) monomers with the bidentate dmbpy ligand occupying both axial and equatorial positions.

Salts of the π-donor *bis*(ethylenedithio)tetrathiafulvalene (BEDT-TTF) have been isolated with hydrogen dichloride (HCl_2^-) as the counterion. Two phases were obtained, α'-BEDT-$TTF_2(HCl_2)$ and ε-BEDT-TTF(HCl_2) by electrocrystallization from solvent mixtures containing $ClCH_2COCl$. α'-BEDT-$TTF_2(HCl_2)$ contains sheets of twisted BEDT-TTF dimers, and conductivity and magnetic susceptibility are consistent with a description of nearly localized $(BEDT\text{-}TTF)_2^+$ radicals. ε-BEDT-TTF(HCl_2), space group *C2/m*, undergoes an anion ordering structural phase transition near 200 K, resulting in a new low temperature phase ε'-BEDT-TTF(HCl_2) with space group $P2_1/c$. Below 170 K, ε'-BEDT-TTF(HCl_2) undergoes a paramagnetic to diamagnetic transition seen in EPR data. The HCl_2^- ion is linear in α'-BEDT-$TTF_2(HCl_2)$ but bent in ε-BEDT-TTF(HCl_2) and ε'-BEDT-TTF(HCl_2).

A new organic metal of the π-donor *bis*(ethylenedioxy)tetrathiafulvalene, $(BEDO\text{-}TTF)_4[C_4N_6]\cdot H_2O$, has been isolated as the N,N',N"-tricyanoguanidinate monohydrate salt. The crystal structure indicates two-dimensional behavior in the BEDO-TTF donor layer demonstrated by the close intermolecular C-H···O, S···S, and S···O contacts. The N,N',N"-tricyanoguanidinate monohydrate dianions are puckered and form dimers through hydrogen bonding with two water molecules, resulting in an infinite sheet of dianions. Four-probe resistance measurements and EPR measurements indicate metallic behavior down to 8.5 (±1) K where a metal-to-insulator transition occurs.

The new organic cation-radical salt, β"-$(BEDT\text{-}TTF)_4[Fe(CN)_6]\cdot 2CH_2Cl_2$, which incorporates the ferricyanide ($Fe(CN)_6^{-3}$) anion, is one the first BEDT-TTF cation-radical salt to incorporate a hexacyanometallate trianion, and it is also the first BEDT-TTF salt to possess donor cations with +0.75 oxidation states. The salt adopts the β" packing motif observed in BEDT-TTF cation-radical salts and behaves electrically as a semiconductor.

CHAPTER 1
BACKGROUND AND INTRODUCTION

Solid-state chemistry encompasses a wide range of methods and materials. These materials may be electrostatic, covalent, metallic, or molecular in regard to the nature of their chemical bonding.[1] When considering the phases or states of matter, the solid-state generally brings to mind high density and large volume materials. This idea of large density and large volume is correct and applies to numerous solid-state materials. However, there is a group of solid-state materials classified as low-dimensional solids. The classification of "low-dimensional" refers to the dimensionality of the chemical bonding in the system. Low-dimensional solids have highly anisotropic bonding schemes within the lattice framework.[2] For example, there are one-dimensional chains of atoms, one-dimensional stacks of molecules, or two-dimensional sheets of molecules giving the materials a column-like or layered structure. In these systems the bonding within a stack, chain, or layer may consist of strong electrostatic, covalent or metallic bonds, while between stacks or layers the interactions are weak van der Waals type.[2] Not only is the bonding in these systems anisotropic, but the interesting physical properties may also be anisotropic in nature. Transport, magnetic, and spectroscopic properties may be enhanced within the chain, stack, or layer. A great deal of attention has been devoted to understanding the physics and chemistry of low-dimensional solids in the last 25 years.[3,4]

Many of the low-dimensional solids are inorganic solid-state coordination compounds. Materials like (tetramethylammonium)manganese(II)chloride, $(H_3C)_4NMnCl_3$ (TMMC),[5] and potassium tetracyanoplatinate bromide hydrate $K_2[Pt(CN)_4]Br_{0.3}\cdot 3.2(H_2O)$ (KCP)[6] are examples of one-dimensional linear chain materials shown in Figures 1-1 and 1-2, respectively. TMMC has chains of Mn(II) ions linked by three bridging chloride anions, while KCP has linear chains of Pt(II) ions. Each material exhibits a unique property along the low-dimensional chain direction. TMMC is the classic example of a magnetic linear chain, with each Mn(II) ions containing five unpaired electrons to give an effective spin of $S = 5/2$. The spins on adjacent ions within a chain align themselves antiparallel to one another resulting in antiferromagnetic coupling along the chain.[7] However, there are no itinerant (free) electrons so the material is an insulator. Nearly all inorganic magnetic linear chain compounds are magnetic insulators.[7] On the other hand, $K_2[Pt(CN)_4]Br_{0.3}(H_2O)_x$, a linear chain material, is highly conductive along the chains of Pt(II) ions. This material is an insulator (i.e. $K_2[Pt(CN)_4]$) before it is doped with Br_2 because all electrons are involved in ionic bonding. In band theory terms, it is said the band comprised of the metal dz^2 orbitals is full. Doping results in partial oxidation of the Pt(II) ions which removes electrons from the band producing mobile electrons that can move up and down the chains.[8]

Another area of solid-state low-dimensional chemistry involves the use of molecules. Molecules bring to mind weak intermolecular forces, which may seem to contradict the goal behind low-dimensional solids. Keep in mind that discrete molecules can have unpaired spins as well as be oxidized or reduced to give free electrons making them interesting components in low-dimensional magnets and conductors. If these molecules are coupled with the appropriate supporting chemical blocks a whole new class of materials is formed, low-dimensional molecular solids. Indeed, there are such materials, and they do possess unique transport and magnetic properties. One group of molecular solids is the organic conductors which possess both interesting magnetic and transport phenomena, and these materials will be discussed in detail later. The exciting feature about molecular low-dimensional solids is the ability of the chemist to, in theory, synthesize molecules which will allow tunability of a specific property of the low-dimensional solid. The rest of this chapter will be devoted to a background study of two types of

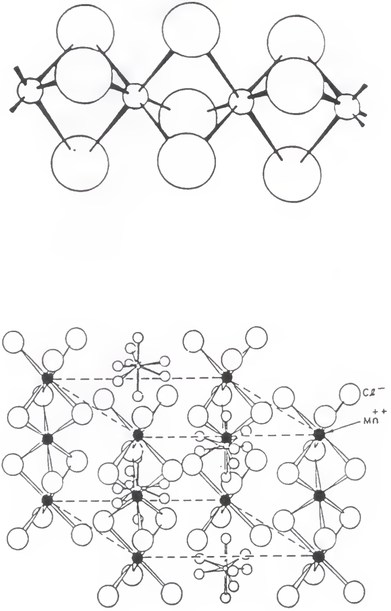

Figure 1-1. The structure of (tetramethylammonium)manganese(II)chloride (TMMC) consisting of infinite linear chains of manganese(II) ions bridged by three chloride ions one of which bridges the Mn(II) ions. The cavities between chains are filled with tetramethylammonium cations. TMMC is the classic example of a low-dimensional antiferromagnetic linear chain material. Figures taken from reference 5.

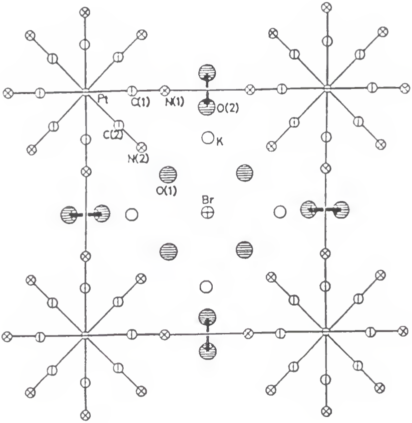

Figure 1-2. The chemical structure of the electrically conducting inorganic linear chain complex $K_2[Pt(CN)_4]Br_{0.3}{\cdot}3.2(H_2O)$. The potassium and bromide ions, and the water molecules are located in the cavities between the Pt(II) chains. Electrical conduction occurs due to the non-integer oxidation state of the Pt atoms and is greatest along the linear Pt chains. Figure taken from reference 6.

low-dimensional solids. The first group of materials is inorganic transition metal linear chain magnetic complexes, and the second group of materials is low-dimensional molecular organic conductors.

1-1 Low-Dimensional Heisenberg Antiferromagnetic Materials

Low-dimensional Heisenberg antiferromagnets can be classified as either one-dimensional or two-dimensional in nature. The name implies that the interesting magnetic properties exist along the one-dimensional stacks or chains, or in the two-dimensional sheets within the lattice. The materials of course contain unpaired electrons which have a spin quantum number, m_s, associated with them. The term Heisenberg is associated with the spin direction of the electron.[7] Just as a solid-state lattice has three principal crystallographic axes, the electron spin has three components, called "spin dimensionality." If a spin is isotropic, having interactions in all three principal directions (x, y, and z), then it is said to have Heisenberg spin dimensionality, while two- and one-dimensional spin systems are called XY and Ising systems, respectively.[7] In one-dimensional or two-dimensional magnetic materials, adjacent magnetic centers at times "sense" one another causing certain alignments of the spins producing what are called "exchange" interactions.

Several situations, which are illustrated in Figure 1-3, exist with regard to the arrangement of spins within a lattice: ferromagnetism, antiferromagnetism, canted antiferromagnetism, and ferrimagnetism. A system in which adjacent magnetic ions have their spin moments aligned parallel to one another resulting in a net magnetic moment is known as a ferromagnet, while those systems composed of a lattice with antiparallel spin moments are termed antiferromagnets, which possess no net magnetic moment.[7] It is the resulting magnetic moment of ferromagnets which make them useful as magnetic storage devices. Canted antiferromagnetism occurs when the spin moments of nearest neighbors are tilted. Because the spin moments are not fully antiparallel, a small net magnetic moment persists.[7] Ferrimagnetism occurs in systems containing two alternating effective spins, for example, $S = 1/2$ and $S = 5/2$.[7] The spins align antiparallel, but because of the different effective spin values, the magnetic moments do not cancel completely resulting in a net magnetic moment.

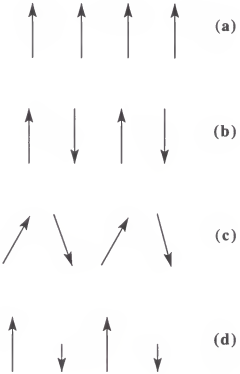

Figure 1-3. Types of magnetic behavior: (a) ferromagnetism, (b) antiferromagnetism, (c) canted antiferromagnetism, and (d) ferrimagnetism.

The focus of this section is low-dimensional Heisenberg antiferromagnets, specifically one-dimensional linear chain Heisenberg antiferromagnets. When a magnetic field, H, is applied to a magnetic material, a magnetization, M, is induced. The magnetic susceptibility of a material is written as

$$\chi = \frac{M}{H} . \qquad (1\text{-}1)$$

The magnetic susceptibility is most often expressed as the molar susceptibility in units of emu/mol. The magnetic susceptibility is a complicated sum of various terms two of which are the diamagnetic susceptibility, χ_{dia}, and the spin susceptibility, χ_{spin}. Due to paired core electrons, all materials inherently have some, albeit small, core diamagnetism. χ_{dia} can be calculated using Pascal's constants,[7] and subsequently subtracted from χ_{spin}. What is of interest when studying magnetic susceptibility is the spin susceptibility which results from the interaction of spins in the lattice. In a Heisenberg system the Hamiltonian is

$$H = -J\sum_{i}\vec{S}_i \cdot \vec{S}_{i+1} \tag{1-2}$$

where $\vec{S}_i$ and $\vec{S}_{i+1}$ are the nearest neighbor spin operators and J is the exchange coupling constant.[7] Recall that a system of localized spins will behave as a simple paramagnet with the low magnetic field susceptibility given by the Curie Law:

$$\chi = \frac{\mathrm{C}}{\mathrm{T}}, \tag{1-3}$$

$$\text{with } C = \frac{Ng^2\mu_B^2 S(S+1)}{3k_B} \tag{1-4}$$

where N is the number of spins, g is the g-value of the material, μ_B is the Bohr magneton, S is the effective spin, k_B is Boltzmann's constant, T is the temperature, and C is called the Curie constant. Most materials are not simple paramagnets but quite frequently behave as ferromagnets or antiferromagnets. The Curie law is modified in these cases in order to account for the added interactions and is known as the Curie-Weiss law shown in Equation 1-5, where θ is positive for ferromagnets and negative for antiferromagnets.

$$\chi = \frac{C}{(T-\theta)} \qquad (1\text{-}5)$$

Non-Integer Spin Systems

With all of these factors considered no exact solutions for the Heisenberg Hamiltonian exist,[7] but the work by Bonner and Fisher[9] led to some approximations which hold up very well for linear chain systems containing S = 1/2 spins. Bonner and Fisher calculated the maximum susceptibility,[9] $\chi_{\max}$, given by the expression

$$\frac{\chi_{\max}}{(Ng^2\mu_B^2 / J_{eff})} = 0.7346 \ , \qquad (1\text{-}6)$$

with a maximum temperature, $T_{\max}$, given by

$$T_{\max} \approx 1.282 J_{eff} / k_B \ . \qquad (1\text{-}7)$$

A plot of the Bonner-Fisher approximation is illustrated in Figure 1-4 and included in the plot are the approximations for other higher effective spin linear chain antiferromagnetic systems. Based on the work of Bonner and Fisher, Weng[10] derived an expression for an S = 1 linear chain Heisenberg antiferromagnetic system while others derived expressions for higher spin systems (S = 3/2, 2, 5/2, and 3).[11] These expressions made it possible to fit experimental data so the magnetic behavior could be characterized. The curves for the various systems shown in Figure 1-4, S = 1/2, 1, 3/2, 2, 3, and ∞, all show Curie-Weiss type behavior above $T_{\max}$ followed by the characteristic broad $\chi_{\max}$ due to antiferromagnetic exchange which decreases to a finite value at T = 0. Probably the most well known and well studied linear chain Heisenberg antiferromagnetic system is $(CH_3)_4NMnCl_3$, TMMC.[5,11] This complex, shown previously in Figure 1-1, consists of infinite linear chains of Mn(II) S = 5/2 ions coordinated by three chloride anions one of which bridges adjacent Mn(II) ions within the chain, while tetramethylammonium cations

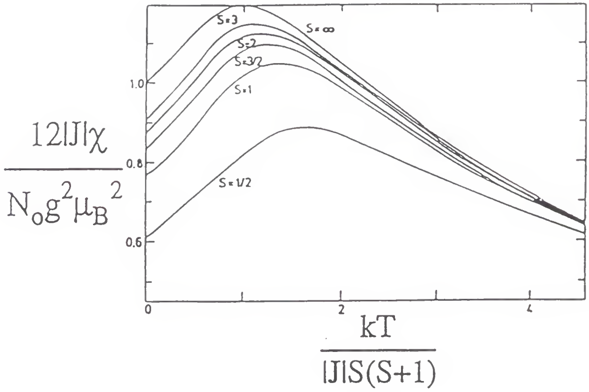

Figure 1-4. The Bonner-Fisher approximation of the susceptibility for an S =1/2 LCHAF, along with those calculated for S = 1, 3/2, 2, 3, and ∞. Taken from reference 7.

reside in the cavities between chains. The $\chi(T)$ for TMMC has the characteristic broad maximum indicative of antiferromagnetic coupling followed by a decrease to a finite susceptibility at lowest temperatures.[11]

Integer Spin Systems and the Haldane Gap Theory

Prior to 1983, all linear chain Heisenberg antiferromagnetic spin systems were thought to behave as described above. At $T = 0$ all systems have three-dimensional antiferromagnetic ordering of the lattice, where all spins are aligned antiparallel to one another with $S_{tot} = 0$.[7] However, many antiferromagnetic materials order well above this extreme temperature. Keep in mind that antiferromagnetic *ordering* is different than the antiferromagnetic *coupling* observed at higher temperatures. Antiferromagnetic *coupling* refers to nearest neighbor spins aligned antiparallel and is a short-range interaction. The signature for antiferromagnetic *coupling* seen in magnetic susceptibility data is a broad maximum. Antiferromagnetic *ordering* on the other hand is when the entire lattice, in all three dimensions, has its spins arranged in an antiparallel fashion, and it is long-range.

Again the theory upheld for linear chain Heisenberg antiferromagnets prior to 1983 stated that the ground state of integer and non-integer spin systems at $T = 0$ was antiparallel alignment of the spins with $S_{tot} = 0$, giving a non-magnetic state known as a singlet ground state. Directly above the ground state there existed a continuum of possible magnetic excited states, for example, where two adjacent spins might be parallel to one another known as a triplet excited state. However, in 1983 Haldane proposed a different scenario for integer spin linear chain Heisenberg antiferromagnets.[12,13] Haldane suggested, based on extensive theoretical calculations, that integer spin linear chain Heisenberg antiferromagnets possessed an energy gap between the $S_{tot} = 0$, non-magnetic ground state and the first excited states; that is, there is not a continuum of excited states directly above the ground state.[12,13] This difference is shown schematically in Figure 1-5. Haldane's work along with other theoretical calculations has resulted in a value of the Haldane gap energy, Δ, for S = 1 systems of $\Delta_{S=1} = 0.41|J|$, where J is the nearest-neighbor exchange energy.[13]

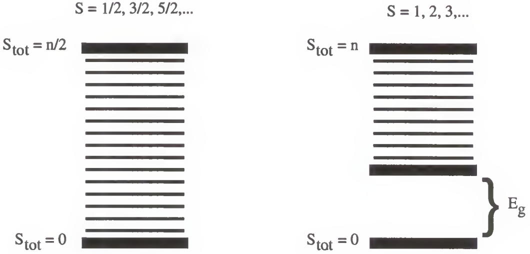

Figure 1-5. Schematic representation of the difference in non-integer and integer spin systems from Haldane's prediction. In this scheme n is the number of unpaired spins, $S_{tot} = 0$ is the singlet ground state where all spins in the lattice are aligned antiparallel, while the excited states lie above where some adjacent spins may be parallel to each other. E_g is the Haldane gap energy.

The prediction put forth by Haldane sparked a renewed interest in the study and synthesis of one-dimensional linear chain Heisenberg antiferromagnets, especially S = 1 complexes since they were the basis of his theoretical studies.[14-17] Haldane's proposal contained several key points concerning the nature of the materials which would possess such an energy gap. First, the behavior of most magnetic complexes is much more complicated than shown by the Heisenberg Hamiltonian in Equation 1-2. Other terms exist because the complexes do not behave isotropically. The Hamiltonian[14] is better written if it includes terms for both single-ion anisotropy, D, and exchange anisotropy, η as:

$$H = J\sum_i \left(S_i^x S_{i+1}^x + S_i^y S_{i+1}^y + \eta S_i^z S_{i+1}^z\right) + D\sum_i \left(S_i^z\right)^2 \qquad (1\text{-}8)$$

Single-ion anisotropy, D, results from distortions of the lattice structure which induce changes in the energy splitting of molecular orbitals.[18] For example, the ligand crystal fields may cost the central magnetic cation extra energy; so to lower the energy, the once degenerate molecular orbitals split, which might result in singly occupied orbitals. If the single-ion anisotropy is positive and large, this will result in spin pairing by adjacent magnetic centers giving a non-magnetic $S = 0$ ground state. Also included in the Hamiltonian is a term for exchange anisotropy, η, which is perturbation on J, the exchange energy.[14] Another effect not included in the above Hamiltonian is exchange between adjacent linear chains, J'. If $J \approx J'$, then the results would be three-dimensional long-range magnetic order. In order to maintain the low-dimensionality in the system, interchain exchange interactions should be minimal.

With both single-ion anisotropy and exchange anisotropy effects in mind, it is clear that Haldane gap materials need to have small single-ion anisotropy terms as well as large J/J' ratios. In other words, there can be no energy gap due to single-ion anisotropy and no three-dimensional long-range antiferromagnetic ordering, because both of these effects will destroy the Haldane phase. Experimental evidence from both temperature dependent susceptibility studies[19] and high-field magnetization measurements[16] can help rule out three-dimensional magnetic ordering and large D phases as well as support the Haldane phase. In three-dimensional ordered systems the $\chi(T)$ data will exhibit Curie-like behavior at high temperatures, a broad maximum due to antiferromagnetic exchange at lower temperatures, followed by a decrease in χ to a finite value at the lowest temperatures, a result of three-dimensional magnetic ordering caused by large J' interchain exchange. In large D phases the high-field magnetization data will show a non-magnetic ground state at low fields followed by a *gradual* increase in magnetization at some critical field, H_c, resulting in a net magnetization.[18]

The Haldane phases show characteristically different behavior in both of these experiments. In Haldane phase systems the temperature dependence of the magnetic susceptibility again shows the Curie-like behavior at high temperatures followed by the broad maximum due to antiferromagnetic exchange.[14] However, below T_{max} the $\chi(T)$ data tend toward zero as T approaches zero, resulting in a non-magnetic S = 0 ground state. When considering the high-field magnetization experiment for a Haldane gap material, there is a non-magnetic state at the lowest magnetic fields as there is in a large D phase. When a Haldane phase material reaches its critical field, H_c , there is *sharp* transition to a magnetic state rather than the *gradual* onset of magnetization seen in the large D phase.[18] Magnetic susceptibility and high-field magnetization are only two of the many techniques used to characterize the presence of a magnetic gap in these types of systems.

Haldane Gap Materials

With the theory of non-integer linear chain Heisenberg systems and a new theory for integer spin systems, physicists put forth considerable effort to establish collaborations with chemists so that experimental evidence could be gathered. Physicists have the ability to characterize the magnetic phenomena of materials, but rely on the chemists to synthesize and characterize the structures of potentially interesting materials. The linear chain compounds $Ni(C_2H_8N_2)_2NO_2(ClO_4)$ (NENP),[20] $Ni(C_3H_{10}N_2)_2NO_2(ClO_4)$ (NINO),[14] $Ni(C_3H_{10}N_2)_2N_3(ClO_4)$ (NINAZ),[16,21] and $(CH_3)_4NNi(NO_2)_3$ (TMNIN)[22,23] are examples of Ni(II) S = 1 complexes which incorporate both nitrite (NO_2^-) and azide (N_3^-) ions as bridging ligands between Ni(II) centers. Numerous other linear chain Heisenberg antiferromagnets exist, but due to large single-ion anisotropy and/or three-dimensional long-range magnetic order, are not well suited as Haldane gap candidates. The materials NENP,[19] NINO,[19] NINAZ[16], and TMNIN[23] have shown experimental evidence for Haldane gaps and are particularly easily studied because the gapped state is accessible at relatively high temperatures (i.e. > 1 K). The temperature is important because at T = 0 all linear chain Heisenberg antiferromagnets are in an ordered state, so the gap should be accessible before three-dimensional ordering occurs. Of the four above mentioned materials, NENP is the most well characterized Haldane gap material. The crystal structure of NENP[20] is shown in Figure 1-6 highlighting the one-dimensional chain structure of the material. There are Ni(II) ions coordinated by two ethylenediamine ligands in the four equatorial positions while the axial positions are occupied by nitrite anions which bridge adjacent nickel ions. Each Ni(II) ion is bridged at one end via a nitrogen atom, and the other end is bridged via one of the two oxygen atoms of the nitrite anion. The perchlorate anions balance charge and reside in the cavities between Ni(II) chains. The perchlorate anions help separate the chains which results in a large intrachain exchange constant, J, while the interchain exchange constant, J', is much smaller giving $J'/J \approx 4 \times 10^{-4}$.[17] The temperature dependent magnetic susceptibility and the magnetic field dependent magnetization for NENP are shown in Figure 1-7 taken from Avenel *et al.*[17] and Katsumata *et al.*[18] The χ(T) data show the broad maximum due to antiferromagnetic exchange at about 50 K, while below 50 K the susceptibility approaches zero as T approaches zero. The high-field magnetization data, M(H), taken at T = 1.3 K, show a non-magnetic state for all three principal axes followed by spontaneous magnetization at a critical field, H_c, for all orientations. Both methods show experimental evidence for the presence of a Haldane gap in NENP. Proton NMR, neutron diffraction, and high-field EPR have been performed also, giving additional support for the presence of a Haldane gap.[24]

Another rather extensively studied S = 1 linear chain Heisenberg antiferromagnet is TMNIN, tetramethylammoniumnickel(II)nitrite. The single crystal X-ray structure of TMNIN was determined by Chou *et al.*,[23] here at the University of Florida, and two views of the structure are shown in Figure 1-8 looking down the chain axis and perpendicular to the chain axis. Each Ni(II) ion is chemically distinct along the chain. One type of Ni(II) ion is octahedrally coordinated by six nitrite oxygen atoms, while the adjacent Ni(II) ion is octahedrally coordinated by six nitrite nitrogen atoms. Each chain is well separated by six tetramethylammonium cations with an intrachain Ni-Ni distance of 3.541 Å and an interchain Ni-Ni distance of 9.1029 Å. The well separated chains help to

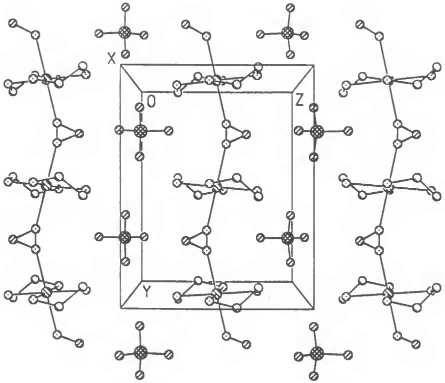

Figure 1-6. X-ray crystal structure of NENP highlighting the Ni(II) linear chains separated by perchlorate anions. Two bidentate ethylenediamine ligands occupy the four equatorial coordination sites around each Ni(II), while the nitrite ligands occupy the axial sites bridging adjacent Ni(II) ions. Structure taken from reference 20.

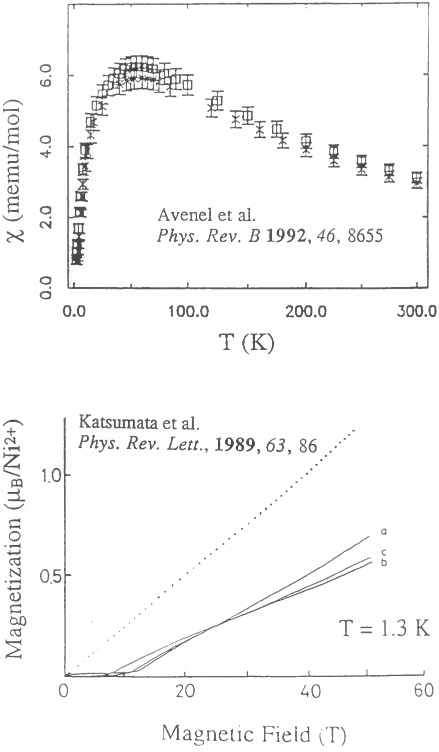

Figure 1-7. The temperature dependent magnetic susceptibility (top) and the magnetic field dependent magnetization (bottom) for NENP. The $\chi(T)$ data show a broad maximum due to antiferromagnetic coupling with the susceptibility approaching zero as T approaches zero, characteristic of a singlet ground state. Taken from references 17 and 18.

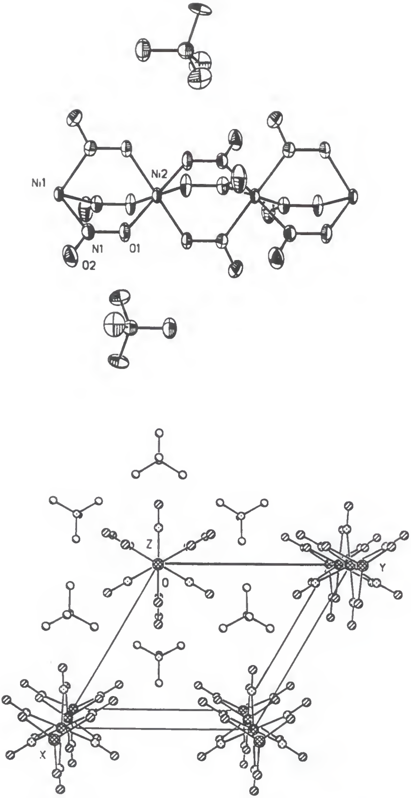

Figure 1-8. The single crystal X-ray structure of TMNIN. The top view is an ORTEP drawing of the structure showing the three different nitrite ligands coordinated to the Ni(II) ions which bridge metal centers. The bottom view is along the chain axis showing the separation of the chains by the tetramethylammonium cations. Taken from reference 23.

prevent any long-range three-dimensional magnetic order from occurring in TMNIN. The temperature dependent magnetic susceptibility for an aligned mosaic of crystals of TMNIN[22,23] with the magnetic field both parallel and perpendicular to the chain axis is plotted in Figure 1-9. The susceptibility gradually increases and passes through a broad maximum at approximately 14 K where it decreases and approaches zero as T approaches zero. This behavior is characteristic of the presence of a singlet, non-magnetic ground state, evidence of a Haldane gap phase. In both NENP and TMNIN the values of the Haldane gap, Δ, are consistent with the calculated values.[25]

With $S = 1$ linear Heisenberg chains receiving much attention, other integer spin systems were neglected. Recently, theoretical calculations by Schollwöck and Jolicœur have been performed on $S = 2$ linear chain Heisenberg antiferromagnetic systems.[26] There results indicate a range of values for the Haldane gap energy, $\Delta_{S=2} = 0.085 \pm 0.005|J|$, where J is the magnetic exchange parameter.[26] With only theoretical results available, experimental interest in $S = 2$ linear chain Heisenberg antiferromagnetic materials sparked, and the results of the experimentation are discussed in Chapter 2.

1-2 Organic Conductors

Early Organic Charge-Transfer Salts

Electrical conduction spans over 24 orders of magnitude, from metals like Cu and Au with room temperature conductivities of 10^5 to 10^6 $\Omega^{-1}\text{cm}^{-1}$, to semiconductors such as GaAs and Si with conductivities of 10^{-3} to 10^2 $\Omega^{-1}\text{cm}^{-1}$, and electrical insulators such as Teflon and sulfur with room temperature conductivities of 10^{-9} to 10^{-18} $\Omega^{-1}\text{cm}^{-1}$.[27] The term "organic conductor" sounds contradictory, because most pure organic materials are electrical insulators with room temperature conductivities on the order of 10^{-10} $\Omega^{-1}\text{cm}^{-1}$. In the mid-1950s organic materials began being explored for their conducting properties.[28] Organic charge-transfer salts were shown to have semiconducting behavior with conductivities of 10^{-6} to 10^{-3} $\Omega^{-1}\text{cm}^{-1}$.[29] Charge-transfer salts can consist of organic

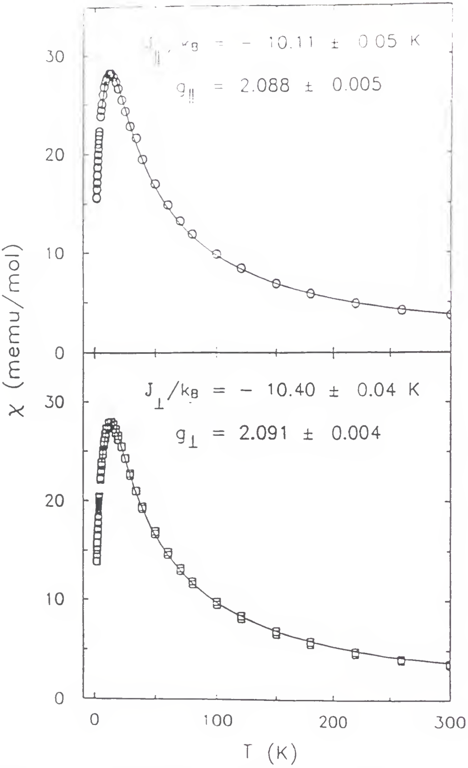

Figure 1-9. The temperature dependent magnetic susceptibility for an aligned single crystal sample of TMNIN with the magnetic field both parallel and perpendicular to the chain axis. As T approaches zero, the susceptibility approaches zero, indicative a singlet non-magnetic ground state. The data are consistent with the presence of a gapped phase. Taken from reference 23.

π-electron donors with organic π-electron acceptors or inorganic anions, while salts between organic π-electron acceptors with alkali metals also form. Transfer of charge is achieved because of the similar redox potentials of the donors and acceptors. Scientists explored this area rather heavily, and in the 1960's a novel π-electron acceptor tetracyano-*p* - quino-dimethane, TCNQ, was synthesized, and charge-transfer salts of TCNQ with alkali metals possessed room temperature conductivities of $10^{-4}\ \Omega^{-1}\text{cm}^{-1}$ to $10^{-6}\ \Omega^{-1}\text{cm}^{-1}$.[29] These conductivities are four to six orders of magnitude greater than many other organic materials. In addition, TCNQ charge-transfer salts with alkylammonium cations were shown to have conductivities of $10^{2}\ \Omega^{-1}\text{cm}^{-1}$.[29] During this active time of research and development of organic based conductors, a new π-electron donor tetrathiafulvalene,[30] TTF, was synthesized. Charge-transfer salts of TTF and halide counterions were shown to have conductivities of $0.2\ \Omega^{-1}\text{cm}^{-1}$.[31] Soon thereafter in 1972 the first organic conductor with metallic-like conduction, TTF-TCNQ (Figure 1-10), was synthesized by Ferraris *et al.*[32] Single crystals of TTF-TCNQ exhibited room temperature conductivities of $5 \times 10^{2}\ \Omega^{-1}\text{cm}^{-1}$.[32] In the charge-transfer salts of the π-electron acceptor TCNQ and the π-electron donor TTF the transport properties lie within the one-dimensional organic columns of these materials making the conductivity highly anisotropic, with the largest conductivity along the stacks of organic molecules. The crystal structures of salts composed of these π-electron acceptors and donors contain segregated stacks of the planar organic entities. Along theses stacks there is good π-molecular orbital overlap, and in the case of TTF good overlap between the molecular orbitals of the large polarizable sulfur atoms. However, what made the TTF-TCNQ salt different from the previous organic charge-transfer salts was the oxidation states of the donor and acceptor. The earlier alkali metal and alkylammonium salts of TCNQ had integer oxidation states of +1 and -1 as well as the (TTF)Cl material. TTF-TCNQ contained non-integer oxidation states or, rather, partial charge-transfer between the donor and acceptor. To get partial charge-transfer the redox potentials of the donor and acceptor need to be similar. If the redox potentials are not similar, as in the case of the alkali metal and alkylammonium cations with TCNQ, there will be full charge-transfer an electron.[28]

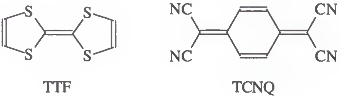

Figure 1-10. Structures of the π-electron donor TTF and the π-electron acceptor TCNQ.

The phenomenon of partial oxidation or non-integer oxidation states is a requirement in the design of metallic-like conduction in organic materials as it is in other non-organic based conducting materials. In solids, band theory is used to describe the electronic structure present. Band theory in solids is similar to molecular orbital theory but with many atoms (~10^{20} atoms). As with molecular orbital theory, in band theory there is a totally symmetric linear combination of orbitals and a totally asymmetric linear combination of orbitals. The symmetry of the oribtals making up the band dictates the energy of the linear combinations. In some cases the totally symmetric combination is lowest in energy with the totally antisymmetric highest in energy, while in other situations, the symmetric is highest in energy and the antisymmetric lowest in energy. In solids the electronic states (orbitals) between these two extremes are very close in energy to one another and form a continuum of electronic states called a band. The bands are filled-up with electrons from the lowest energy level to the highest level. Bands containing electrons are termed valence bands, while empty ones are conduction bands. If the valence band is partially empty, this allows a mechanism for electrons to migrate to low-lying unoccupied excited states which allows the electrons to conduct through the solid. Partial oxidation of donors and acceptors in organic materials produce partially filled bands. In TTF-TCNQ for example, there is charge-transfer of 0.59 electrons from the donor TTF to the acceptor TCNQ, which is possible due to the delocalization of the electrons through the extended π-framework of the molecules.[27]

The TMTSF Conductors

With the discovery of the organic metal TTF-TCNQ came a renewed interest in the quest for other conducting and even superconducting organic materials. In 1974, Klaus Bechgaard and Dwaine Cowan[33] synthesized a new π-donor, tetramethyltetraselenafulvalene (TMTSF), depicted in Figure 1-11, which exhibited the characteristic features seen in TTF. TMTSF is planar with a conjugated π-orbital framework and large, highly polarizable selenium atoms. Cation-radical salts, synthesized by Bechgaard and Jérome,[34,35] with the formula $(TMTSF)_2X$, incorporating inorganic anions such as PF_6^-, AsF_6^-, TaF_6^-, SbF_6^-, ReO_4^-, and ClO_4^- exhibited high room temperature conductivities ($5 \times 10^2\ \Omega^{-1}cm^{-1}$) which increased up to as much as two orders of magnitude as the temperature decreased. In fact, in the salts with PF_6^-, AsF_6^-, TaF_6^-, SbF_6^-, and ReO_4^- anions, the resistance at approximately 1 K under 12 kbar went to zero, suggesting the existence of superconductivity in these organic based materials. Shortly after this discovery, $(TMTSF)_2ClO_4$ was found to go superconducting at 1.2 K at ambient pressure.[36] All of these materials like TTF-TCNQ consisted of layers of organic donor molecules. In the TMTSF salts the donor layers are separated by layers of inorganic anions. Again, the greatest interaction between donor molecules is along the stacks giving rise to highly anisotropic conductivity, with the conductivity along the stacks being the greatest.[37] The stoichiometry of these materials is two TMTSF molecules for every monoanion, resulting in an effective charge on each TMTSF molecule of +1/2 keeping with the partial oxidation state requirement for conductivity.

The TMTSF series of cation-radical salts were synthesized in an electrochemical cell using constant current methods.[34-36] The cell, shown in Figure 1-12, is known as an H-cell which has two compartments separated by porous fritted glass.[38] Both compartments contain a solution of the inorganic anion (electrolyte) while the anode compartment contains the neutral donor TMTSF. Each cell compartment holds a platinum electrode which is connected to a constant current supply. The donor is electrochemically oxidized at the anode and anions from the electrolyte result in the precipitation of single crystals of the cation-radical salts at the anode. The electrochemical method of producing organic cation-radical salts is widely used because it results in highly pure single crystals useful in a variety of physical property characterization techniques.

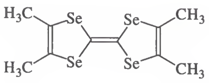

TMTSF

Figure 1-11. The structure of the organic π-electron donor TMTSF.

The BEDT-TTF Family of Conductors

The advent of organic superconductivity initiated the quest for new, more highly specialized organic donor molecules. The design of organic donor molecules remained the same, synthesis of planar molecules with extended π-framework and large polarizable atoms. In 1983 the donor *bis*(ethylenedithio)tetrathiafulvalene,[39] BEDT-TTF (Figure 1-13) was found to form a cation-radical salt with the perrhenate anion, ReO_4^-, $(BEDT\text{-}TTF)_2ReO_4$ which displayed superconductivity at 2 K under 4 kbar pressure.[40] This salt was the first example of an organic superconductor with a sulfur based organic donor. BEDT-TTF based cation-radical salts differ structurally from the TTF and TMTSF families. Again both the TTF and TMTSF materials form one-dimensional stacks of donors leading to high conductivity in one dimension. The crystal structures of the BEDT-TTF conductors and superconductors consist of two-dimensional sheets of donor

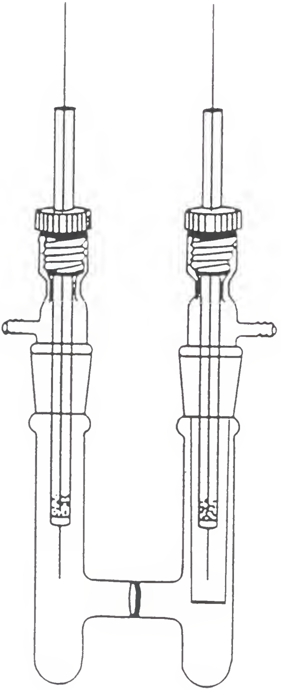

Figure 1-12. Typical two compartment H-cell used in the constant-current electrocrystallization of organic cation-radical salts. Taken from reference 38.

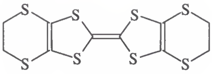

BEDT-TTF

Figure 1-13. The structure of the organic π-electron donor BEDT-TTF.

molecules. The side-by-side sulfur atom orbital overlap is greater than the overlap along the columns of donor molecules. Conductivity is large within the two-dimensional sheets,[41] but rather small along the stacks. The stoichiometry of the BEDT-TTF based conductors and superconductors with monoanions is 2:1 with a +1/2 charge on each BEDT-TTF cation. Many times crystal structures of the BEDT-TTF materials reveal that the donors are dimerized, in which case there is one electron delocalized between two molecules resulting in the 2:1 stoichiometry as well as partial oxidation states and partially filled conduction bands. To date the BEDT-TTF family of cation-radical salts has resulted in over 50 superconductors which is the largest number in any of the organic cation-radical salt families.[4]

The two-dimensional nature of the donor layers in BEDT-TTF based salts allows for more degrees of freedom resulting in a variety of crystal phases. The BEDT-TTF packing style adopted dictates the physical properties observed in the material. The various packing styles are designated by a Greek letter.[4,38] For example, the β-phase[3] (Figure 1-14) salts form with corrugated sheets of donors, high conductivities, and many of the salts undergo a superconducting transition at low temperatures. The α-phase[3] (Figure 1-14) materials form donor sheets with a "herringbone" arrangement, resulting in conductors which undergo a metal-to-insulator transition below room temperature, while the α'-phase salts[42] are weak semiconductors at room temperature with charge localization due to Mott-Hubbard type interactions. Another BEDT-TTF phase, the κ-phase,[3] is made up of

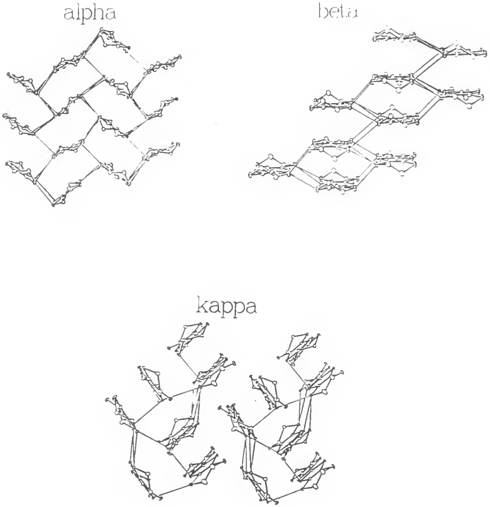

Figure 1-14. The donor layers for the α-, β-, and κ- phases of $(BEDT\text{-}TTF)_2I_3$. The α-phase forms "zig-zag" layers of donor molecules, while the β-phase forms columns of donor molecules which have a high degree of overlap with molecules in adjacent columns forming a highly conducting two-dimensional plane. The κ- phase also forms two-dimensional sheets containing orthogonal dimers which lead to species with high conductivities. Taken from reference 3.

conducting, superconducting, and semiconducting materials. The κ-phase (Figure 1-14) materials form sheets of orthogonal BEDT-TTF dimers separated by layers of counterions. The BEDT-TTF salt with the highest superconducting transition temperature belongs to the κ-phase, κ-$(BEDT\text{-}TTF)_2Cu[N(CN)_2]Cl$, with a superconducting transition temperature of 12.8 K under a pressure of 0.3 kbar.[43] Recently, in 1995, the first organic superconductor of BEDT-TTF with a magnetic counterion was synthesized by Peter Day's group.[44] The salt, β-$(BEDT\text{-}TTF)_4[(H_2O)Fe(C_2O_4)_3]\cdot C_6H_5CN$, contains paramagnetic Fe(III) ions and has a superconducting transition temperature of 7 K. This salt contains BEDT-TTF donors in a 4:1 ratio with the counterion.[44] The donor layers have five crystallographically unique BEDT-TTF molecules, while the anion layer is made up of Fe(III) ions surrounded by three oxalate groups with benzonitrile and water molecules residing in the cavities. BEDT-TTF salts can adopt numerous crystal packing motifs as well as a variety of stoichiometries resulting in materials with diverse physical properties.

1:1 Cation-Radical Salts of the Donor BEDT-TTF

Most of the conducting and superconducting cation-radical salts in the BEDT-TTF family form with a 2:1 donor:anion stoichiometry with monovalent anions.[4] While the most commonly studied organic cation-radical salts are those where the formal oxidation state of the donor is +1/2, other oxidation states of BEDT-TTF are known. Recently, the first cation-radical salts of BEDT-TTF where BEDT-TTF exists solely as +2 ions have been prepared, showing that high-oxidation state salts of BEDT-TTF are stable.[45] In the BEDT-TTF family of cation-radical salts there exists a class of materials which form with a 1:1 donor:anion stoichiometry with monovalent anions. A survey of this class of BEDT-TTF materials has resulted in 20 BEDT-TTF salts with 1:1 stoichiometry. The materials are listed in Table 1-1 and included are the crystal system, space group, central C=C bond distance (if given in the literature), and transport properties (if given).

In this list of 1:1 BEDT-TTF salts it is interesting to note that 1:1 salts exist with a variety of counterions of differing geometries. There are linear triatomic counterions

Table 1-1. The BEDT-TTF (denoted as "ET") 1:1 cation-radical salts and selected crystallographic and physical property data.

Salt Formula	**Crystal System**	**Space Group**	**C=C Bond Length (Å)**	**Transport Property**
$(ET)PF_6$[54]	Monoclinic	$C2_1/c$		semiconductor
δ-$(ET)PF_6$[55]	Triclinic	$P\bar{1}$	1.381(8)	
ε-$(ET)PF_6$[56]	Monoclinic	$C2/m$	1.396(9)	
ζ-$(ET)PF_6$[63]	Triclinic	$P\bar{1}$		semiconductor
$(ET)PF_6 \cdot 0.5CH_2Cl_2$[57]	Triclinic	$P\bar{1}$	1.378	semiconductor
$(ET)PF_6 \cdot 0.5THF$[50]	Triclinic	$P\bar{1}$	1.379(6)	
ε-$(ET)ClO_4$[50]	Monoclinic	$C2/m$	1.390(7)	
$(ET)ReO_4 \cdot 0.5THF$[51]	Monoclinic	$P2/c$	1.375(28)	semiconductor
$(ET)IO_4 \cdot 0.5THF$[51]	Monoclinic	$P2/c$	1.38(3)	semiconductor
$(ET)Ag_4(CN)_5$[60]	orthorhombic	F_{ddd}		
$(ET)AuBr_2Cl_2$[52]	orthorhombic	P_{nnm}		semiconductor
$(ET)AuCl_2$[48]	Triclinic	$P\bar{1}$	1.37(6)	semiconductor
$(ET)(AuCl_2)AuCl_4$[58]	Monoclinic	$C2/m$	1.40(2)	semiconductor
$(ET)BiI_4$[59]	Triclinic	$P\bar{1}$	1.373(12)	semiconductor
$(ET)CuCl_2$[47]	Triclinic	$P\bar{1}$	1.382(6)	
$(ET)FeBr_4$[53]	Triclinic	$P\bar{1}$	1.383(15)	semiconductor
$(ET)HgBr_3$[49]	Triclinic	$P\bar{1}$	1.37	semiconductor
$ET(Ni(dmit)_2)$[61]	Triclinic	$P\bar{1}$		semiconductor
ε-$(ET)HCl_2$[46]	Monoclinic	$C2/m$	1.390(4)	
ε'-$(ET)HCl_2$[46]	Monoclinic	$P2_1/c$	1.388(4)	

(HCl_2^- and $CuCl_2^-$, and $AuCl_2^-$),[46-48] trigonal planar ($HgBr_3^-$),[49] tetrahedral (ClO_4^-, ReO_4^-, IO_4^-, $AuBr_2Cl_2^-$, $FeBr_4^-$),[50-53] octahedral (PF_6^-),[50,54-57] mixed systems ($AuCl_2^-/AuCl_4^-$),[58] a polymeric network (BiI_4^- and $Ag_4CN_5^-$),[59,60] and one salt with acceptor molecules ($Ni(dmit)_2$).[61] A recurring feature seen in the 1:1 cation-radical salts of BEDT-TTF is the semiconducting behavior observed. Despite the fact that many of these salts form columns, two-dimensional, and even three-dimensional arrays (i.e. the $Ag_4CN_5^-$ salt) of donor molecules, the absence of good sulfur orbital overlap between adjacent molecules within a column or sheet decreases the degree of electron delocalization and thus a path for conduction. In fact in some of the salts there are no true stacks or sheets of donor molecules.[53,62] The absence of stacks of BEDT-TTF cations has been said to be due Coulomb repulsion between the relatively large charges residing on the molecules.

Within the BEDT-TTF salts having 1:1 stoichiometry three of those materials pack with a motif designated as the ε-phase.[46,50,56] Two BEDT-TTF salts with 2:1 stoichiometry and with linear triatomic halide anions have also been designated as ε-phase materials, but this ε-phase is unique for the linear triatomic halides. All three of the known ε-phase BEDT-TTF 1:1 salts, ε-(BEDT-TTF)PF_6,[56] ε-(BEDT-TTF)ClO_4,[50] and ε-(BEDT-TTF)HCl_2,[46] crystallize in the monoclinic system *C2/m* . Also in each case the terminal ethylene groups on the BEDT-TTF molecules and the counterions are located on *2/m* sites with the ethylene groups disordered about the mirror plane while the counterions are disordered about a center of inversion. In each case there are columns of face-to-face BEDT-TTF cations with the molecules situated in a bond-over-ring arrangement, but no dimerization between molecules in a column occurs. Each monocation is discrete and has one close contact between outer ring sulfurs on adjacent cations.

Within the BEDT-TTF family of 1:1 salts with the octahedral counterion hexafluorophosphate, PF_6^-, there are several phases. There is the previously mentioned ε-(BEDT-TTF)PF_6,[56] along with (BEDT-TTF)PF_6,[54] δ-(BEDT-TTF)PF_6,[55] ζ-(BEDT-TTF)PF_6,[63] (BEDT-TTF)PF_6·0.5CH_2Cl_2,[57] and (BEDT-TTF)PF_6·0.5THF.[50] The δ-phase, and the two solvated phases, CH_2Cl_2 and THF, all contain BEDT-TTF dimers separated by layers of PF_6^- counterions and solvent molecules in two cases. In both the δ-phase and the THF solvated system the BEDT-TTF dimers are arranged face to face. The CH_2Cl_2 solvated phase contains BEDT-TTF dimers in a bond-over-ring configuration and the dimers within a column are slipped relative to one another. The ζ-phase on the other hand is made up of discrete BEDT-TTF monocations separated by layers of counterions. The BEDT-TTF family of 1:1 salts with the PF_6^- counterion conveys an interesting point about the cation-radical salts derived from the donor BEDT-TTF donor. The BEDT-TTF donor molecule can form many different phases and structures with the same inorganic counterion.

The other BEDT-TTF salts, excluding the ε-phases and the PF_6^- materials, form materials which are also characterized by their mode of BEDT-TTF cation packing. The 1:1 salts with the anions BiI_4^-,[59] $FeBr_4^-$,[53] $HgBr_3^-$,[49] IO_4^-, and ReO_4^-,[51] form salts with layers of BEDT-TTF dimers, while salts with the anions $AuCl_2^-$,[48] $AuBr_2Cl_2^-$,[52] $AuCl_2AuCl_4^-$,[58] $CuCl_2^-$,[47] HCl_2^-,[46] and Ni(dmit)$_2^-$ form with layers of discrete BEDT-TTF cations.

Looking at the salts contained in Table 1-1, there are many BEDT-TTF materials with a variety of inorganic anions and acceptor molecules which form 1:1 salts. Of the salts for which conductivity data are known, the trend is evident, the 1:1 materials are semiconductors, and those with no conductivity data given can be assumed to be semiconductors as well. The electronic structure of these materials is greatly affected by the integer charge residing on the BEDT-TTF molecules. The HOMO of the BEDT-TTF neutral molecule contains two electrons which in terms of band theory is a full band. If one electron is removed, the HOMO and consequently the conduction band are only half full, which is inherently unstable and results in an electronic reorganization at the Fermi level (the highest occupied level in the band). This reduced interaction between electrons at or near the Fermi level is energetically more favorable and serves to localize the electrons in low electric potential wells. Electrical conduction must then be "activated" thermally in order to occur. Materials of this type of electronic behavior are referred to as Mott-Hubbard insulators.[53,62,63] These materials represent a class of organic-cation radical salts which have similar transport properties but are unique and interesting from a structural point of view. With the majority of the hundreds of known organic cation-radical salts of BEDT-TTF possessing +1/2 oxidation state on the BEDT-TTF molecules, with a few (described above) having +1 oxidation state, along with the handful of examples containing BEDT-TTF^{+2} molecules, our interest was in forming non-integer charges between +1/2 and +1 along with those between +1 and +2. Using the methods derived for synthesizing the +2 oxidation state salts of BEDT-TTF,[45] several new 1:1 salts including interesting hydrogen dichloride (HCl_2^-) salts are discussed in Chapter 3.

Cation-Radical Salts Based on the Donor BEDO-TTF

Solid-state chemists working in the area of conducting organic cation-radical salts modify the electron donors and counterions used in order to synthesize new conducting materials. In the past decade many new electron donors have been presented in the literature, but probably one of the most fruitful new donors has been *bis(*ethylenedioxy) tetrathiafulvalene (BEDO-TTF), shown in Figure 1-14, first synthesized by Suzuki *et al.* in 1989.[64,65] BEDO-TTF, like its predecessors, is a planar, conjugated, extended π-orbital molecule. As BEDT-TTF salts, BEDO-TTF materials form complexes with inorganic counterions as well as organic acceptors which are comprised of two-dimensional sheets of BEDO-TTF donor molecules separated by sheets of counterions. To date over 50 BEDO-TTF salts have been synthesized and exhibit metallic conductivity, while only two superconductors and two semiconductors exist.[66] The BEDO-TTF molecule has oxygen atoms in the outer rings. The incorporation of these oxygen atoms at the peripherary of the BEDO-TTF molecules is believed to be responsible for the large number of metallic complexes formed. BEDO-TTF has a lower oxidation potential than BEDT-TTF, making it

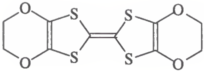

Figure 1-15. The structure of the organic π-electron donor BEDO-TTF.

a better electron donor.[67] Also, the greater electron-donating ability of the oxygen atoms versus the sulfur atoms helps put charge back on the central C=C bond in the HOMO. The greater electronegativity of oxygen also serves to stabilize the donor molecule network in these salts. Nearly every salt of the BEDO-TTF donor molecule forms with the same donor molecule packing arrangement, and the donor layer of the salt $(BEDO\text{-}TTF)_2ReO_4{\cdot}H_2O$ is shown in Figure 1-16. The formation of only one packing motif has been attributed to the numerous short O···O and C-H···O contacts between BEDO-TTF molecules within a donor layer.[66] The contacts are not only close, but the overlap of oxygen and sulfur orbitals on adjacent molecules is very good. The good orbital overlap between molecules results in BEDO-TTF materials with wide conduction bands like those seen in conventional metals. The BEDT-TTF family of materials are unlike the BEDO-TTF materials with poor overlap resulting in narrow bands. However the small number of superconductors formed with BEDO-TTF is likely due to the wide conduction bands present. Wide conduction bands have a lower density of states at the Fermi level than do narrow bands, which reduces the electron/lattice interactions needed to form Cooper-pairs. This proposal is likely true since there are over 50 superconductors known with the electron donor BEDT-TTF.[4] The fact still remains that BEDO-TTF is an excellent electron donor which has a high incidence for producing organic metals. Knowing that BEDO-TTF has a strong tendency to form organic metals, our interest was in producing new high-oxidation state salts of BEDO-TTF which incorporated high-valent anions in the lattice. Nearly 100% of the known BEDO-TTF cation-radical salts form with

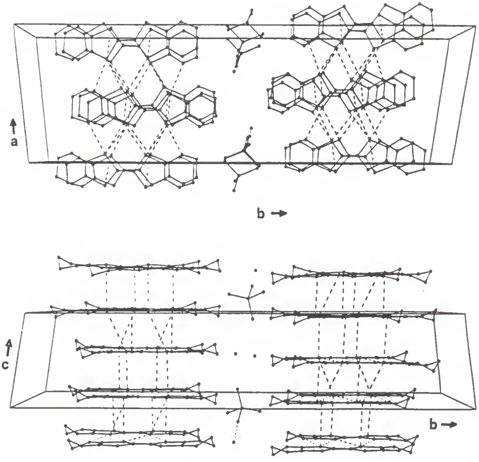

Figure 1-16. The BEDO-TTF donor layer for (BEDO-TTF)$_2$ReO$_4$·H$_2$O. The packing style adopted by perrhenate salt is the style observed in most BEDO-TTF cation-radical salts and is designated the "I$_3$" motif from the salt (BEDO-TTF)$_{2.4}$I$_3$. This style is characterized by BEDO-TTF molecules aligned side-by-side forming a 2D array with close S···O, S···S, and C-H···O contacts. Taken from reference 66.

BEDO-TTF$^{+1/2}$ molecules, while the majority of the salts are with monovalent inorganic anions or organic acceptors.[66] This study resulted in the isolation of a new metallic BEDO-TTF salt containing the high carbon/nitrogen N,N',N"-tricyanoguanidinate dianion ($C_4N_6^{-2}$) discussed in Chapter 4.

1-3 Scope of Dissertation

The work presented in this dissertation focuses on two types of low-dimensional solids. The first group of solid-state materials are inorganic transition metal linear chain magnetic complexes, while the second group are low-dimensional organic conductors. In Chapter 2 we discuss the syntheses, structures, and magnetic properties of a group of linear chain Heisenberg antiferromagnetic complexes possessing Mn(II) ions with an effective spin of $S = 2$. The experimental results show conclusive evidence for the first $S = 2$ linear chain Heisenberg antiferromagnet Haldane gap complex 2,2'-bipyridinetrichloromanganese(III), $[MnCl_3(C_{10}H_8N_2)]_n$. Another $S = 2$ linear chain Heisenberg antiferromagnet 1,10-phenanthrolinetrichloromanganese(III), $[MnCl_3(C_{12}H_8N_2)]_n$, was characterized by X-ray crystallography showing the polymeric linear chain structure, while the magnetic studies indicate the presence of a magnetic phase transition at low temperature to a "canted" antiferromagnetic state. A novel five-coordinate $S = 2$ manganese(III) complex 4,4'-dimethyl-2,2'-bipyridinetrichloromanganese(III) acetonitrile solvate, $MnCl_3(C_{12}H_{12}N_2)\cdot CH_3CN$, was characterized by X-ray crystallography and the results show interesting coordination around the manganese(III) center as well as an interesting packing motif.

The remaining three chapters discuss the syntheses, X-ray structures, and physical properties of novel low-dimensional organic cation-radical salts. We set out to isolate new organic cation-radical salts containing high-oxidation state donor cations as well as incorporation of high-valent anions. In Chapter 3 we discuss the crystal structures, transport and magnetic properties of the first BEDT-TTF cation-radical salts isolated with the hydrogen dichloride anion. Two phases, a 2:1, α'-(BEDT-TTF)$_2$HCl$_2$, and a 1:1, ε-(BEDT-TTF)HCl$_2$, are obtained from the same electrocrystallization cell. The salts are interesting because of their precipitation with the hydrogen dichloride anion, which only a handful of salts are known to form. In Chapter 4 we discuss the results of the synthesis, transport, and EPR measurements performed on a new organic metal based on the π-electron organic donor BEDO-TTF, (BEDO-TTF)$_4$[C$_4$N$_6$]·H$_2$O, which incorporates a new high carbon/nitrogen dianion N,N',N"-tricyanoguanidinate ($C_4N_6^{-2}$). This salt is metallic down to ~8 K where it undergoes a metal-to-insulator transition. A complete study of the temperature and angular dependent EPR behavior of (BEDO-TTF)$_4$[C$_4$N$_6$]·H$_2$O is also discussed. In the final section, Chapter 5, we discuss the X-ray structure, transport, EPR, and magnetic susceptibility results for the first BEDT-TTF cation-radical salt to contain both BEDT-TTF$^{+3/4}$ cations and a hexacyanometallate trianion (Fe(CN)$_6^{-3}$), β"-(BEDT-TTF)$_4$[Fe(CN)$_6$] ·2CH$_2$Cl$_2$. This salt contains a highly two-dimensional BEDT-TTF cation network which conforms to the β"-packing motif observed in BEDT-TTF salts. The BEDT-TTF molecules are tetramerized both along the columns and within the sheets of donor molecules. β"-(BEDT-TTF)$_4$[Fe(CN)$_6$] ·2CH$_2$Cl$_2$ behaves electrically as a semiconductor with a room temperature conductivity of 0.35 Ω^{-1}cm^{-1}. The tetramerization of the BEDT-TTF molecules dictates both the electrical and magnetic properties observed in this material.

CHAPTER 2
SYNTHESIS, STRUCTURE, AND MAGNETISM OF MANGANESE(III) S = 2 HEISENBERG QUASI-LINEAR CHAIN ANTIFERROMAGNETS

2-1 Introduction

In recent years much theoretical and experimental research has been focused on understanding the difference between linear chain Heisenberg antiferromagnets (LCHA's) of integer spin versus non-integer spin. The research was initiated in order to verify the theory proposed by Haldane in 1983[12,13] termed the Haldane gap theory. Haldane's belief was that an energy gap existed between the ground state and the first excited states for an integer spin (S = 1, 2, 3...) LCHA system, whereas no such gap exists in non-integer (S = 1/2, 3/2, 5/2...) systems. LCHA systems can be described by the Hamiltonian[7] :

$$H = -J\sum_{i} \vec{S}_i \cdot \vec{S}_{i+1} \qquad (2\text{-}1)$$

where J is the antiferromagnetic exchange constant between magnetic centers within a single chain and $\vec{S}_i$ and $\vec{S}_{i+1}$ are nearest neighbor spins. This energy gap between the ground state and the first excited state is unique to a special case of integer spin LCHA's. Imagine in the solid-state that these infinite linear chains are packed next to one another in an ordered array. This arrangement is known to be the case with evidence from X-ray crystallography. In these linear chain materials there is also antiferromagnetic exchange between chains termed J'. If J and J' are comparable, it is likely that the material will have three-dimensional long-range antiferromagnetic ordering at some transition temperature known as the Néel temperature.[7] For a system to be a potential Haldane material no long-range order can exist above the gap temperature because the material would no longer behave one-dimensionally. All LCHA materials order antiferromagnetically,[7] but most Haldane materials order well below the Haldane gap. For a Haldane system this implies $J > J'$. In these Haldane systems the behavior of the temperature dependent susceptibility and the magnetic field dependent magnetization data is unique to the integer spin Heisenberg antiferromagnets. The magnetic susceptibility shows the characteristic broad maximum due to antiferromagnetic exchange followed by a decrease towards zero as the temperature approaches zero. The magnetization data at low field show no net magnetization, but as a sweep is made to higher fields a critical field is attained at which point the magnetization increases. The magnetic susceptibility tending toward zero and the absence of magnetization below a critical field are both evidence of a non-magnetic state, while the higher temperature susceptibility data and the stronger field magnetization data are characteristic of a magnetic state. The premise behind the Haldane gap theory is a singlet, spin paired, non-magnetic, S = 0 ground state separated by an energy gap above which lies a triplet, magnetic (unpaired spins) excited state.[12,13]

Initially much of the effort was focused on theoretical calculations to determine values of the gap energy, especially for the case of an S = 1 linear chain Heisenberg antiferromagnet. The theoretical studies seemed to support Haldane's prediction of an energy gap, but these calculated values needed to be verified with experimental evidence. The quest to find S = 1 linear chain Heisenberg antiferromagnets exploded and the search resulted in numerous materials, four complexes of which have been intensely studied. The linear chain materials $Ni(C_2H_8N_2)_2NO_2(ClO_4)$ (NENP),[20] $Ni(C_3H_{10}N_2)_2NO_2(ClO_4)$ (NINO),[14] $Ni(C_3H_{10}N_2)_2N_3(ClO_4)$ (NINAZ),[16,21] and $(CH_3)_4NNi(NO_2)_3$ (TMNIN)[22,23] are all Ni(II) S = 1 complexes which incorporate both nitrite (NO_2^-) and azide (N_3^-) as bridging ligands between Ni(II) centers. These materials have been studied using temperature dependent magnetic susceptibility, magnetic field dependent magnetization, high-field ESR, neutron diffraction, and proton nuclear magnetic resonance methods.[26] All of the experimental results agree quite well with the theoretical prediction of the energy of the Haldane gap for an S = 1 LCHA: $\Delta = 0.41|J|$,[25] where J is the exchange energy.

The study of S = 1 LCHA's both theoretically and experimentally is thorough and well documented,[14,17-19,25] however integer spin LCHA's with S > 1 (e.g. 2, 3...) have not been extensively studied experimentally. Recently, numerous theoretical studies on S = 2 spin chains have been performed using models of varying chain length and the results indicate a Haldane gap energy, Δ, for an S =2 LCHA: $\Delta = 0.08|J|$, $0.055|J| \pm 0.015$, $0.05|J|$, $0.085|J|.\pm 0.005$, and $0.049|J| \pm 0.018$,[26] where J is the exchange energy. These values show the gap energy to be considerably lower than in S = 1 systems. The real S = 2 systems studied however, all show three-dimensional antiferromagnetic ordering at temperatures above the Haldane phase.[68,69] One compound, anhydrous chromium(II) chloride has recently been studied and the magnetic susceptibility results seem to back-up the existence of S = 2 linear chains of Cr(II) cations;[69] however, no data supporting the existence of a Haldane gap has been published. Our interest in S = 2 materials stemmed from earlier work at the University of Florida on the S = 1 Haldane materials NENP, TMNIN, and NINAZ.[17,22,23] A thorough search of the literature resulted in several S = 2 manganese(III) complexes which were initially promising as Haldane materials. The inorganic manganese(III) materials 2,2'-bipyridinetrichloromanganese(III) (**4**), and 1,10-phenanthrolinetrichloromanganese(III) (**5**) are examples of S = 2 linear chain antiferromagnets,[70,71] while (4,4'-dimethyl-2,2'-bipyridine)trichloromanganese(III) acetonitrile solvate (**6**) is a new five-coordinate manganese(III) complex. Complexes **4** and **5** had only been characterized magnetically down to 100 K,[70,71] but the data supported the presence of antiferromagnetic, polymeric (chain) materials. The crystal structure of **4** was solved in 1990[72] proving the existence of infinite manganese(III) chains bridged by chloride ions. In this work, complex **4** was characterized by a variety of techniques in order to determine the presence of energy gap between the non-magnetic ground state and the first excited states (i.e. a Haldane gap). The results of variable temperature magnetic susceptibility, high-field magnetization, and electron paramagnetic resonance support the existence of a Haldane phase in **4**. The crystal structure of complex **5** was determined in this work, and the structure contains infinite manganese(III) chains coordinated by phenanthroline and chloride ligands. Magnetic susceptibility results reveal antiferromagnetic exchange interactions followed by a transition to a "canted" antiferromagnetic state where the spin moments do not cancel one another completely resulting in a net magnetic moment. At lowest temperatures, **5** becomes diamagnetic. The preliminary results on the diamagnetic nature of **5** are presented, but future work remains in order to fully understand the diamagnetic transition. Compound **6** was synthesized in the attempt isolate an $S = 2$ manganese(III) linear chain which would possess larger cavities between chains due to the bulkier methyl substituted bipyridine ligand. A new five-coordinate manganese(III) complex **6** was made and its crystal structure solved. Complex **6** contains manganese(III) ions coordinated by three chloride anions and one dimethylbipyridine (dmbpy) ligand. The complex forms columns of dimerized units which pack with the dmbpy ligands alternating from side-to-side. The columns are separated by acetonitrile molecules. Complex **6** is a new example in a scarce group of five-coordinate manganese(III) complexes. The following chapter presents the synthesis, characterization, and magnetic results of work completed on these manganese(III) inorganic complexes.

2-2 Experimental Section

Materials. Manganese(II) acetate tetrahydrate ($Mn(CH_3COO)_2{\cdot}4H_2O$), potassium permanganate ($KMnO_4$), acetic acid (CH_3COOH), trimethylchlorosilane ($(CH_3)_3SiCl$), and acetonitrile (CH_3CN) were purchased from Fisher Scientific (Orlando, FL). The molecules 2,2'-bipyridine ($C_{10}H_8N_2$), 4,4'-dimethyl-2,2'-bipyridine ($C_{12}H_{12}N_2$), and 1,10-phenanthroline ($C_{12}H_8N_2$) were purchased from Aldrich Chemical Co. (Milwaukee, WI) and used without further purification. Trimethylchlorosilane was dried over molecular sieves for three days prior to use, while acetonitrile was dried over P_2O_5 and distilled before use. Throughout the text 2,2'-bipyridine, 1,10-phenanthroline, and 4,4'-dimethyl-2,2'-bipyridine will be referred to as bpy, phen, and dmbpy respectively.

Preparation of $Mn_{12}O_{12}(CH_3COO)_{16}(H_2O)_4 \cdot 2CH_3COOH \cdot 4H_2O$ (1). The method of Lis[73] was employed to form this manganese cluster compound. In a 400 mL beaker 8.0 g (32.6 mmol) of $Mn(CH_3COO)_2 \cdot 4H_2O$ (**2**) was added to 80 mL of 60% CH_3COOH and heated until dissolution. The mixture was cooled to room temperature. Meanwhile 2.0 g (12.6 mmol) of $KMnO_4$ (**3**) was dissolved in a minimum (~20 mL) of 60% CH_3COOH and added dropwise to the cooled solution **2**. The resulting mixture was heated slowly to 60°C followed by slow cooling. After two days the solution was filtered through a Büchner funnel and the red-brown solid **1** collected and dried in the air overnight. Yield 7.251 g; 30% yield. Analysis calculated for $C_{36}H_{72}Mn_{12}O_{56}$: C, 20.98; H, 3.52. Found: C, 20.37; H, 3.37.

Preparation of (2,2'-bipyridine)trichloromanganese(III) $[MnCl_3(bpy)]_n$ (4). Compound **1** (0.2 g, 0.097 mmol) was added to 50 mL of acetonitrile and stirred until dissolution. While stirring the solution, 0.44 mL (3.5 mmol) of trimethylchlorosilane was added dropwise resulting in a "purple solution".[72] The "purple solution" was filtered through a Büchner funnel and the "purple filtrate" retained. A 30 mL acetonitrile solution of 0.183 g (1.2 mmol) 2,2'-bipyridine (bpy) was layered on top of the "purple filtrate" and the solution was covered with a KimWipe and left untouched to allow crystallization to occur. After 7 days brick-red, plate-like crystals of **4** were collected by filtration on a Büchner funnel, washed with cold acetonitrile, and dried in the air for several hours followed by storage in a dessicator. Yield: 0.181 g; 50% yield. Analysis calculated for $C_{10}H_8Cl_3MnN_2$: C, 37.83; H, 2.54; N, 8.82. Found: C, 37.78; H, 2.35; N, 8.60.

Preparation of (1,10-phenanthroline)trichloromanganese(III) $[MnCl_3(phen)]_n$ (5) Compound **1** (0.2 g, 0.097 mmol) was added to 50 mL of acetonitrile and stirred until dissolution. While stirring the solution **1** 0.44 mL (3.5 mmol) of trimethylchlorosilane was added dropwise resulting in a "purple solution". The "purple solution" was filtered through a Büchner funnel and the "purple filtrate" retained. A 30 mL acetonitrile solution of 0.126 g (0.67 mmol) 1,10-phenanthroline was layered on top of the "purple filtrate" and the solution was covered with a KimWipe and left untouched to allow crystallization to occur. After 3 days brick-red, rectangular, plate-like crystals of **5** were collected by filtration on a Büchner funnel, washed with cold acetonitrile, and dried in the air for several hours followed by storage in a dessicator. Yield: 0.263 g; 66% yield. Analysis calculated for $C_{12}H_8Cl_3MnN_2$: C, 42.20; H, 2.36; N, 8.20. Found: C, 43.52; H, 2.44; N, 8.39.

Preparation of (4,4'-dimethyl-2,2'-bipyridine)trichloromanganese(III) acetonitrile solvate [$MnCl_3$(dmbpy)·(CH_3CN) (**6**). Compound **1** (0.2 g, 0.097 mmol) was added to 50 mL of acetonitrile and stirred until dissolution. While stirring the solution **1** 0.44 mL (3.5 mmol) of trimethylchlorosilane was added dropwise resulting in a "purple solution". The "purple solution" was filtered through a Büchner funnel and the "purple filtrate" retained. A 30 mL acetonitrile solution of 0.180 g (0.977 mmol) 4,4'-dimethyl-2,2'-bipyridine was layered on top of the "purple filtrate" and the solution was covered with a KimWipe and left untouched to allow crystallization to occur. After 7 days long, deep blue, rod-like crystals of **6** were collected by filtration on a Büchner funnel, washed with cold acetonitrile, and dried in the air. After several minutes the crystals decomposed into a black powder, presumably due to loss of the acetonitrile solvent molecule. Further batches synthesized were collected by filtration inside an $N_{2(g)}$ purged dry bag. Yield: 0.205 g; 46% yield. Analysis calculated for $C_{14}H_{15}Cl_3MnN_3$: C, 41.71; H, 3.50; N, 8.11. Found: C, 41.81; H, 3.40; N, 7.99.

Preparation of (2,2'-bipyridine)trichloroaquomanganese(III) $MnCl_3(bpy)H_2O$ (**7**). To a 600 mL beaker was added 10.0 g of $KMnO_4$ to 100 mL of 10 M HCl. The mixture was allowed to react at room temperature for approximately 10 minutes. A "brown" thick solution results containing a mixed valent solution of Mn(III) and Mn(IV) anionic chloride complexes.[70,71] To 15 mL of the "brown" solution was added a solution of 1.0 g (6.4

mmol) of 2,2'-bipyridine in 5 mL of 10 M HCl and 15 mL water with stirring. Within a few minutes a red/brown microcrystalline solid of **7** precipitated which was collected on a Büchner funnel and washed with 2 M HCl, acetone, and ether followed by vacuum drying. Yield: 1.131 g; 53% yield. Analysis calculated for $C_{10}H_{10}Cl_3MnN_2O$: C, 35.8; H, 3.0; N, 8.35. Found: C, 35.88; H, 2.97; N, 8.25.

Preparation of (1,10-phenanthroline)trichloroaquomanganese(III) $MnCl_3(phen)H_2O$ (8). To a 600 mL beaker was added 10.0 g of $KMnO_4$ to 100 mL of 10 M HCl. The mixture was allowed to react at room temperature for approximately 10 minutes. A "brown" thick solution results containing a mixed valent solution of Mn(III) and Mn(IV) anionic chloride complexes.[70,71] To 100 mL of the "brown" solution was added a solution of 0.70 g (3.53 mmol) of 1,10-phenanthroline monohydrate in 7.5 mL of 10 M HCl with stirring. After several minutes a red microcrystalline solid of **8** precipitated which was collected on a Büchner funnel and washed with 5 M HCl and acetone followed by vacuum drying. Yield: 1.078 g; 84% yield. Analysis calculated for $C_{12}H_{10}Cl_3MnN_2O$: C, 40.1; H, 2.8; N, 7.8. Found: C, 40.47; H, 2.76; N, 7.79.

Crystallographic data collection and structure determination of (4,4'-dimethyl-2,2'-bipyridine)trichloromanganese(III) acetonitrile solvate $[MnCl_3(dmbpy)\cdot(CH_3CN)$ (6). Crystallographic data for (**6**) are listed in Appendix Tables A-1 through A-3. Data were collected at 173 K on a Siemens SMART PLATFORM equipped with a CCD area detector and a graphite monochromator utilizing MoK_α radiation ($\lambda = 0.71073$ Å). Cell parameters were refined using 8132 reflections. A hemisphere of data (1381 frames) was collected using the ω-scan method (0.3° frame width). The first 50 frames were remeasured at the end of data collection to monitor instrument and crystal stability (maximum correction on I was < 1 %). ψ-scan absorption corrections were applied based on the entire data set.

The structure was solved by Direct Methods in *SHELXTL5*,[74] and refined using full-matrix least squares. The non-H atoms were treated anisotropically, whereas the hydrogen atoms were calculated in ideal positions and were riding on their respective carbon atoms. A total of 197 parameters were refined in the final cycle of refinement using 3476 reflections with $I > 2\sigma(I)$ to yield R_1 and wR_2 of 0.030 and 0.076 , respectively. Refinement was done using F^2.

Static susceptibility and high-field magnetization measurements on **4**, **5**, **7**, and **8**. Static susceptibility measurements were performed using a Quantum Design MPMS SQUID magnetometer on powder-like samples (30 - 70 mg) of **4**, **5**, **7**, and **8** as well as on approximately 2.4 mg of 90 oriented single crystals **4** in a static magnetic field of 1 kG. The single crystals of **4** were held together by gluing them to weighing paper using clear fingernail polish. The sample was placed in a #5 gel capsule which was held in a straw during the experiment. A similar arrangement of weighing paper and fingernail polish was made and measured in order to serve as a background. The background signals arising from the gel cap, straw, and weighing paper/fingernail polish arrangement were subtracted from the data.

High-field magnetization measurements were performed at the National High Magnetic Field Laboratory (NHMFL) in Tallahassee, FL by Professor Mark Meisel and his graduate student Garrett Granroth. The magnetization measurements were made using a single crystal Si cantilever magnetometer[26] mounted in the mixing chamber of a commercial dilution refrigerator. Several single crystals of **4** (approximate mass 200 μg) were studied at 30 ± 5 mK and 1.4 ± 0.2 K in magnetic fields up to 16 T (T = tesla). A small temperature independent diamagnetic background was subtracted from the data.

EPR measurements of **4**. Electron paramagnetic resonance (EPR) spectra of five aligned single crystals of **4** were recorded on a Bruker (Billerica, MA) ER 200D spectrometer at 9.26 GHz modified with a digital signal channel and a digital field controller equipped with an Oxford Instruments (Witney, England) ITC 503 temperature controller and ESR 900 cryostat. The sample was held on the cut edge of a quartz rod using a trace amount of vacuum grease to hold the material in place. Data were collected using a U.S. EPR (Clarksville, MD) SPEX300 data acquisition program.

2-3 Results and Discussion

Synthesis and Structure of [$MnCl_3(bpy)]_n$ (**4**).

The crystal structure of (2,2'-bipyridine)trichloromanganese(III) was published in 1991 by Perlepes *et al* [72] so only a brief discussion of the important features of the structure will be described. Microcrystals with typical size 0.09 mm x 0.4 mm x 0.9 mm have been grown using Perlepes' method with some modifications in order to obtain sufficiently large single crystals. An excess of trimethylchlorosilane was added to a concentrated solution of **1** to give a "purple solution". This "purple solution" has been said to contain '$MnCl_3$'[72]. Upon addition of a dilute solution of the ligand 2,2'-bipyridine, followed by slow evaporation over a period of 7 days, X-ray quality single crystals can be harvested. Growing single crystals of the chain compounds is important so the orientation dependent magnetic studies can be performed.

A packing diagram of **4** is shown in Figure 2-1 highlighting the linear chain nature of the material. Complex **4** consists of infinite quasi-linear chains of Mn(III) atoms along the *c*-axis, linked by bridging chloride ligands with two more chlorides and bipyridine nitrogen atoms occupying the other 4 coordination sites. The crystals are rectangular in shape and the long axis of the crystal corresponds to the crystallographic *c* axis which is the chain axis. High-spin Mn(III) complexes have octahedral coordination with the d-orbitals splitting into the $^5T_{2g}$ and ^5E_g terms. With this type of d-orbital splitting a Jahn-Teller distortion is expected in order to remove the degeneracy of the ^5E_g term.[75] This distortion results in elongation of the axial (i.e. bridging) Mn-Cl bonds to give a half-filled dz^2 orbital as the HOMO.[75]

Other important features of **4** are the Mn-Mn *intra*chain and *inter*chain distances. A desirable quality of this complex is the shorter Mn-Mn *intra*chain distance compared to the Mn-Mn *inter*chain distance. In the search for Haldane gap materials, complexes which have long-range antiferromagnetic ordering are to be avoided. Antiferromagnetic (AF) coupling and antiferromagnetic ordering are distinctly different phenomena. AF coupling

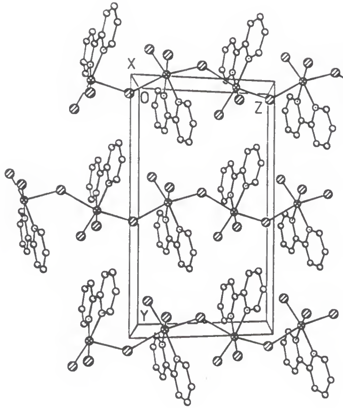

Figure 2-1. The packing diagram for **4** highlighting the infinite chains present. The bipyridine ligands alternate from left to right along the chains. The axial Mn-Cl bonds are elongated as a result of a Jahn-Teller distortion.

implies nearest neighbor spins aligning themselves antiparallel to one another, while the spins several ions removed may not be aligned in an antiparallel (AF) fashion. AF ordering on the other hand is transition to a state in which all of the spins in the entire lattice (all three dimensions) align themselves in an antiparallel manner. This type of behavior would contradict the premise behind the work which is to study the magnetism of low dimensional solids.

What type of lattice interactions then would favor AF ordering and which would favor AF coupling? Strong *intra*chain and *inter*chain interactions would most likely lead to long-range order. In **4** the Mn-Mn *intra*chain distance is 4.83 Å[72] with strong Mn-Mn interactions via overlap of the Mn dz^2 orbitals through the chloride bridge. The shortest Mn-Mn *inter*chain distance is 7.96 Å[72] which is considerably larger than the *intra*chain distance. Therefore since this *inter*chain distance is large and no ligands bridge the chains, magnetic exchange between chains is expected to be negligible. Furthermore, the Mn-Cl-Mn bond angle of 135°[72] is consistent with antiferromagnetic exchange. The $S = 2$ quasi-linear chain complex $[MnCl_3(bpy)]_n$ from a structural perspective meets the requirements needed to be a Haldane gap material. The following section will elaborate on the experimental evidence which supports the presence of a Haldane gap in the quasi-linear chain compound $[MnCl_3(bpy)]_n$.

Static Susceptibility, EPR, and High-Field Magnetization Data for $[MnCl_3(bpy)]_n$ (4).

The static magnetic susceptibility measurements were performed using both a powder sample and the aligned single crystals sample described above. Initially a powder (i.e. randomly oriented) susceptibility measurement was performed using 15.65 mg of **4**. The temperature dependence of the magnetic susceptibility $\chi(T)$ is plotted in Figure 2-2 for the powder sample measured in a magnetic field of 1 kG. The susceptibility results show a broad peak near 100 K and a kink at approximately 12 K. At the lowest temperatures $\chi(T)$ exhibits a strong upturn indicative of Curie-like impurities. Subsequent magnetic susceptibility runs were initiated on fresh powder samples giving the same results as previously seen. The kink at 12 K was possibly (a) evidence for antiferromagnetic ordering of the Mn(III) ions, or (b) magnetic phenomenon from some other impurity specimen. Of the two, (b) was highly possible. The synthesis[70,71] of **4** is known to produce a six-coordinate hydrated monomeric by-product, **7**, depicted in Figure 2-3. Complex **7** was synthesized by published procedures[70,71] and magnetic susceptibility measurements were performed. The temperature dependence of the magnetic susceptibility $\chi(T)$ for **7** is plotted in Figure 2-4. The susceptibility data exhibit Curie-Weiss (simple paramagnet) behavior as the temperature is lowered followed by a narrow maximum in susceptibility at 5 K indicative of weak antiferromagnetic coupling with $\chi(T)$ approaching a finite value as T approaches 0 K, evidence of antiferromagnetic ordering in the system. However, no anomalous behavior was present at 12 K, proving the kink at 12 K in the susceptibility data for **4** was not due to $MnCl_3(bpy)(H_2O)$ impurities. The anomaly at 12 K appears to be a consequence of using a randomly oriented powder sample which might contain trace amounts of magnetic impurities. In order to understand the nature of the kink experiments on aligned single crystal samples were considered. Using an aligned single crystal sample helps reduce the trace amounts of extrinsic impurities associated with powder samples.

The oriented single crystal sample of **4** was studied with the crystal face (*ab* plane) aligned both perpendicular and parallel to the static magnetic field (i.e. perpendicular and parallel to the chain axis). The temperature dependence of the magnetic susceptibility $\chi(T)$ is plotted in Figure 2-5 both perpendicular and parallel to the chains. The $\chi(T)$ results show a broad peak near 100 K and anisotropy below 80 K such that $\chi_{perp} > \chi_{par}$. At lowest temperatures a strong upturn in $\chi(T)$ exists and is thought to be associated with a Curie-like impurity. The broad maximum near 100 K is the expected behavior for a linear chain Heisenberg antiferromagnet. Also as stated in the introduction, section 2-1, Haldane gap materials must show no evidence of long range antiferromagnetic ordering. In the present case of $[MnCl_3(bpy)]_n$, the $\chi(T)$ data display no signs of long range

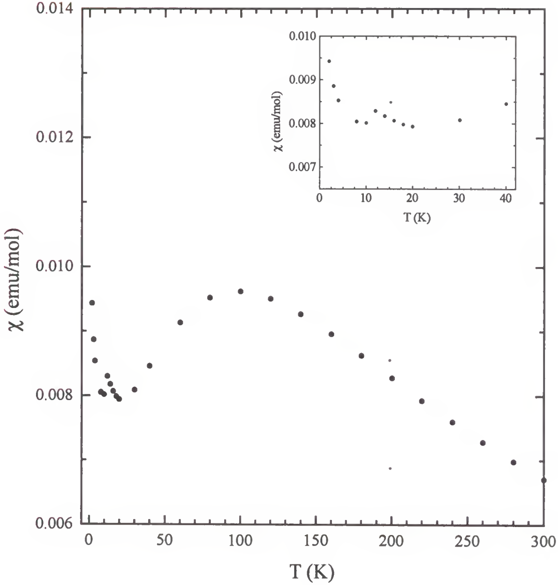

Figure 2-2. The temperature dependence of the magnetic susceptibility χ(T) for a powder sample of **4** measured in a magnetic field of 1 kG. The results show a broad maximum at 100 K indicative of antiferromagnetic coupling and a kink at 12 K, but no long-range order down to 2 K.

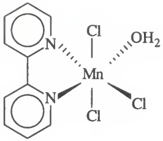

Figure 2-3. The structure of the monomeric complex **7**.

antiferromagnetic ordering down to the lowest temperature measured. The χ(T) data have been fit using

$$\chi(T) = \chi(0) + \frac{\mathrm{C}}{\mathrm{T}} + \chi_{LCHA}(S = 2, g, J, T), \quad (2\text{-}2)$$

where C/T represents the Curie contribution at low temperatures and χ_{LCHA} (S = 2, *g*, *J*, T) represents the S = 2 linear chain Heisenberg antiferromagnetic calculations of Weng,[10] as parameterized by Hiller *et al.*[76] shown in Equation 2-3 below

$$\chi_{LCHA} = \left(\frac{N\mu_{\beta}^{2} g^{2}}{kT} \right) \left[\frac{A + Bx^{2}}{1 + Cx + Dx^{3}} \right], \quad (2\text{-}3)$$

where *N* is the number of spins, μ_B is the Bohr magneton, *k* is the Boltzmann constant, T is the temperature, $x = |J| / kT$, A = 2.0000, B = 71.938, C = 10.482, and D = 955.56. The results of the fit are shown by the solid line in Figure 2-2. The fit gave a Curie constant of 47.5 ± 0.05 memu-K/mol, *J* = 34.8 ± 1.6 K and g = 2.04 ± 0.04. The value of the Curie constant can be attributed to a small concentration of impurity spins, while the value of *J* is consistent with antiferromagnetic exchange in linear chain materials, and the value of *g* agrees with known values of *g* for Mn(III) complexes.

To explore the nature of the Curie-like impurities evident in the magnetometry results, X-band EPR experiments on an aligned mosaic of crystals of **4** were performed from 4 to 60 K with the crystal faces (chain axis) aligned perpendicular and parallel to the static magnetic field. The signal observed is due to Mn^{2+} spins (S = 5/2) and not Mn^{3+} spins (S = 2). At the X-band EPR experiment frequency of approximately 9.25 GHz the resonance due to Mn^{3+} spins is not observable because the energy levels of the singlet ground state and the first excited triplet state are considerably higher in energy compared to those of Mn^{2+}. The purpose of the EPR experiment was to quantitatively determine the level of impurity in the material.

The resonance observed was calibrated against a widely used standard, α, α'-diphenyl-β-picryl hydrazyl (DPPH)[77] at 4 K. For a purely Lorentzian EPR signal the area under the resonance is proportional to the number of spins present in the sample. Knowing the number of spins present in the DPPH standard, the sample being tested can be calibrated to the DPPH standard, and a value for the number of spins present in the sample extracted. The signal observed is consistent with a concentration of approximately 0.05±0.03% Mn^{2+} spins ($S = 5/2$, $g = 2$). This value is more than an order of magnitude smaller than needed to explain the low temperature behavior of the static susceptibility data. The remaining intrinsic impurities contributing to the Curie tail are thought to be due to S = 1 end chain spins. The presence of end chain spins has been observed in S = 1 one-dimensional linear chain systems whose end chain spins end with S = 1/2 spins, an the phenomenon has been explained using the valence bond solid (VBS) model.[78]

The field dependence of the magnetization $M(H)$ was performed at the National High Magnetic Field Laboratory (NHMFL) in Tallahassee, Florida. The purpose of the high field magnetization study was to search for the existence of a transition from a non-magnetic to a magnetic state at some critical field which would be evidence of a gapped phase (i.e. Haldane gap). Magnetization experiments were performed on single crystals by sweeping magnetic fields from 0 to 16 T (Tesla) at both 30 ± 5 mK and 1.4 ± 0.2 K. The

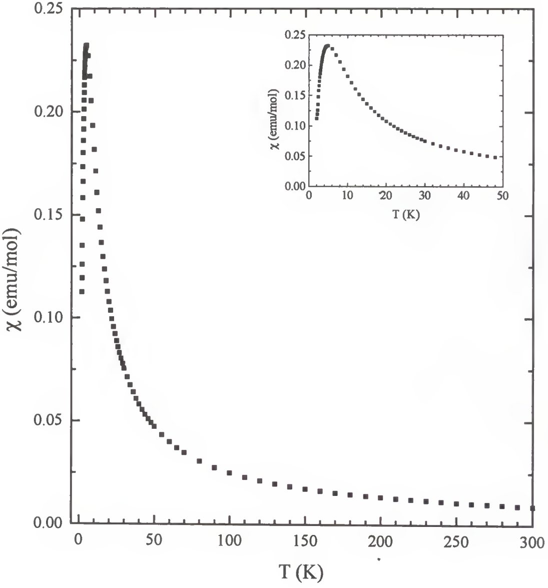

Figure 2-4. The temperature dependence of the magnetic susceptibility χ(T) for a powder sample of **7** measured in a magnetic field of 1 kG. The data show Curie-like behavior to low temperatures with no kink present at 12 K. A narrow maximum at 5 K exists evidence for weak antiferromagnetic correlations.

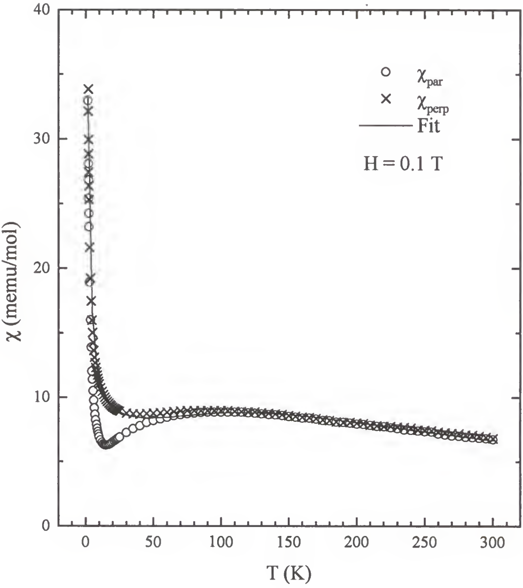

Figure 2-5. The temperature dependence of the magnetic susceptibility χ(T) for an aligned single crystal sample of **4** measured in a magnetic field of 1 kG for the chains both parallel and perpendicular to the static magnetic field. The maximum at 100 K is evidence of antiferromagnetic coupling in low-dimensional systems, with no anomaly at 12 K.

field dependence of the magnetization $M(H)$ is plotted in Figure 2-6. The magnetic field was applied both perpendicular and parallel to the chains. The $M(H)$ results at 30 mK in both orientations show the presence of a non-magnetic state at lowest fields followed by the continuous onset of magnetization above a critical field H_c the value of which is different for the perpendicular and parallel orientations. For the perpendicular orientation $H_{c(perp)}$ = 1.2 ± 0.2 T, and for the parallel orientation $H_{c(par)}$ = 1.8 ± 0.2 T.

In both orientations there were no indications of three-dimensional long-range ordering or any other anomalies in fields up to 16 T. Three-dimensional long-range ordering would have been characterized by hysteresis or a spin-flop transition. Hysteresis is characterized by a the presence of a remnant magnetization as the field is swept back down to zero tesla. A spin-flop transition will appear as a kink in the M vs. H plot and is due to some of the antiferromagnetically coupled spins (i.e. aligned antiparallel) in the magnetic lattice orienting themselves parallel to one another resulting in an increase in the magnetization. Neither of these phenomena were observed in the high field magnetization studies. The presence of a critical field, H_c , for both the perpendicular and parallel orientations, marking the transition from a non-magnetic state to a magnetic state is evidence of a Haldane gap phase in $[MnCl_3(bpy)]_n$.

Synthesis and Structure of $[MnCl_3(phen)]_n$ (5).

The Mn(III) complex **5** was synthesized in the attempt to isolate another S = 2 linear chain complex whose temperature dependent magnetic properties could be studied. Like the isostructural $[MnCl_3(bpy)]_n$ **4** complex, the magnetics of complex **5** have been studied by Goodwin and Sylva down to approximately 120 K.[70,71] Complex **5** like complex **4** behaved antiferromagnetically with a Weiss constant of -183 K. The premise behind looking at $[MnCl_3(phen)]_n$ was 1,10-phenanthroline is a somewhat larger ligand. This characteristic could space the chains further apart which would decrease *J'* between the chains and hopefully enhance *J* within the chain. The crystal structure had not been solved when we started our work. A crystal structure was necessary to help prove the

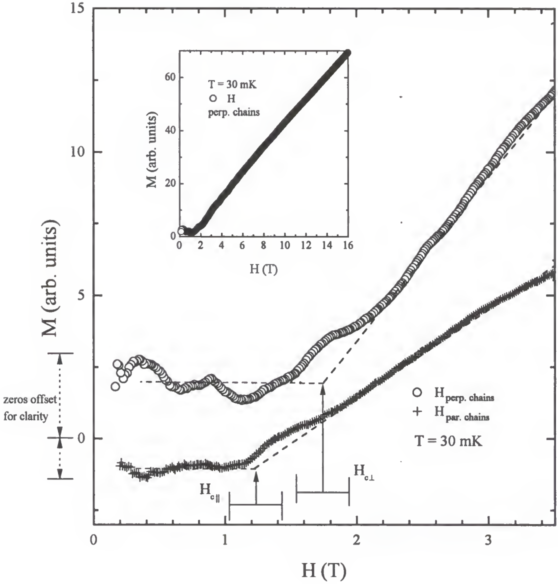

Figure 2-6. The high-field magnetization data for **4** with the chains both parallel and perpendicular to the magnetic field. The sample is diamagnetic in both orientations until a critical field, H_C, is attained at which time the magnetization increases linearly with increasing magnetic field.

infinite chain structure of the complex. Red/brown microcrystals were grown using the method outlined by Perlepes *et al.*[72] using 1,10-phenanthroline rather than 2,2'-bipyridine as the ligand. Picking a single crystal from the batch, a crystal structure was solved, however the refinement was not within the acceptable error limit. The preliminary structure did show that the red/brown crystalline material was the quasi-linear chain complex **5** and a view of the structure perpendicular to the chains is shown in Figure 2-7.

The structure consists of infinite linear chains of octahedrally coordinated Mn(III) ions with two chloride ligands and one bidentate 1,10-phenanthroline ligand occupying the equatorial positions while two chlorides occupy the axial positions and act as the bridges between adjacent Mn(III) ions. As in **4**, **5** is axially elongated with Mn-Cl bond lengths of 2.673 Å and 2.574 Å, while the equatorial Mn-Cl and Mn-N bond lengths are 2.238 Å, 2.244 Å, and 2.061 Å, 2.066 Å respectively. Also, the Mn-Cl-Mn bond angle is 134.4° which is consistent with antiferromagnetic exchange between Mn(III) metal centers through the chloride bridge. The shortest *intra*chain Mn-Mn distance in **5** is 4.838 Å which is the same as in **4**, while the shortest *inter*chain distance is 9.189 Å. This *inter*chain distance is considerably longer in **5** than in **4** (7.96 Å) which is should decrease the magnetic exchange interaction, *J'* between chains. The substitution of the larger 1,10-phenanthroline in place of 2,2'-bipyridine indeed separated the chains which should have some effects on the magnetic properties which will be discussed in the following section.

Static Susceptibility Data for $[MnCl_3(phen)]_n$ (**5**).

Static susceptibility measurements were performed only on powder samples of $[MnCl_3(phen)]_n$ because the single crystals of the material were smaller than the lower limit size needed for alignment. The temperature dependence of the susceptibility $\chi(T)$ is plotted in Figure 2-8 measured in a magnetic field of 1 kG. The susceptibility results show a broad peak near 80 K and a significant increase in $\chi(T)$ at approximately 22 K which goes through a maximum at 11 K followed by a decrease to a finite value at lowest temperatures. This kink in $\chi(T)$ is indicative of some form of magnetic ordering. The broad maximum at

80 K is characteristic of antiferromagnetic coupling in one-dimensional magnetic systems, however the sudden increase in $\chi(T)$ at approximately 22 K is not behavior associated with antiferromagnetism. The increase in $\chi(T)$ in an antiferromagnetically coupled system is evidence that the system is not purely antiferromagnetic; that is, the unpaired spins on adjacent Mn(III) ions are not aligned anti-parallel to one another, but rather they are tilted at some angle. This type of behavior in magnetic systems is termed "canted" antiferromagnetism. Effectively the spins adjacent to one another do not cancel one another resulting in a net magnetization. Using Equation 2-4

$$\mathrm{M} = N\mu_{ferro}\mathrm{H} \tag{2-4}$$

where M is magnetization, N is the number of spins in the sample, H is the magnetic field, and μ_{ferro} is the ferromagnetic magnetic moment the net ferromagnetic moment can be obtained. The value of μ_{ferro} is an indication of the degree of canted antiferromagnetism in the system. Taking $\mathrm{M} = 3.31 \times 10^{-3}$ emu, $\mathrm{H} = 1$ kG, and $N = 5.69 \times 10^{19}$ spins a value of 6.3×10^{-3} μ_β is obtained for μ_{ferro}. This value is extremely small for an effective magnetic moment, but is consistent with the presence of "canted" antiferromagnetism.

As in the case of **4**, the six-coordinate hydrated monomeric complex of **7**, $MnCl_3(phen)(H_2O)$ **8**, was synthesized by published procedures[70,71] in order to determine if it was the source of the anomaly at 22 K in the $\chi(T)$ data. Complex **8** is isostructural with the 2,2'-bipyridine analog, **7**, described previously. The temperature dependence of the magnetic susceptibility $\chi(T)$ for **8** is plotted in Figure 2-9. The data show **8** behaves as a simple paramagnet to the lowest temperatures followed by a narrow maximum at 4.5 K indicative of weak antiferromagnetic coupling, while below 4.5 K the material appears to order antiferromagnetically, with $\chi(T)$ approaching a finite value as T approaches 0. In the temperature range 20 to 25 K no kink or other unusual behavior is evident in the data,

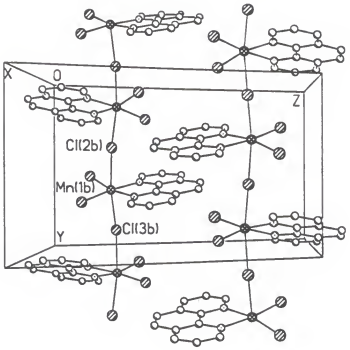

Figure 2-7. The packing diagram for **5**. The structure consists of infinite quasi-linear Mn(III) chains linked by bridging chloride anions. The bidentate 1,10-phenanthroline ligands alternate from left to right down the chains.

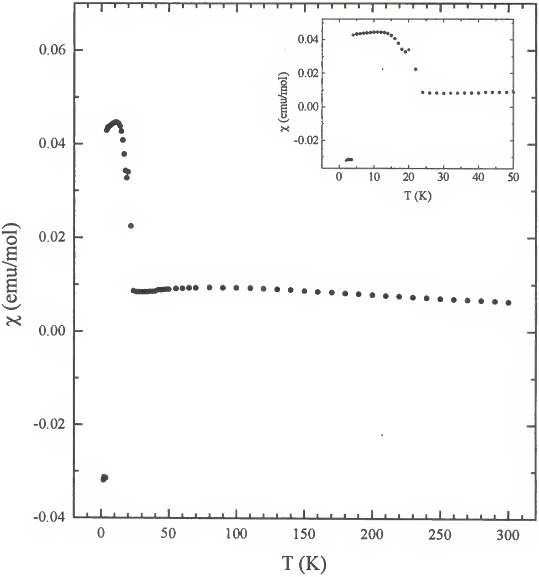

Figure 2-8. The temperature dependence of the magnetic susceptibility χ(T) for **5** measured in a magnetic field of 0.1 T. The data show a broad maximum at 80 K indicative of antiferromagnetic coupling followed by a sharp increase in χ(T) at 22 K evidence of canted antiferromagnetism in this material. A small diamagnetic signal occurs at the lowest temperatures due to remnant magnetic fields which align the spins downward.

proving that the anomaly in the $\chi(T)$ data of **5** was not a result of $MnCl_3(phen)H_2O$,**8**, impurities.

The magnetization as a function of temperature M(T) for a polycrystalline sample of **5** was probed at temperatures below 35 K. Several runs were made with the sample field cooled (FC) and zero-field cooled (ZFC). The magnetization data taken in a field of 10 mT (where T is Tesla) is plotted in Figure 2-10. First the sample is ZFC to 2 K, and once this temperature is reached, the field is increased to 10 mT. When the field is constant (stabilized), the temperature is increased and the magnetization recorded. The sample was also FC to 5 K in a field of 10 mT. After the field is stabilized at 5 K the temperature is increased and the magnetization recorded. When **5** is zero field cooled, the data show that it is diamagnetic at the lowest temperatures with M = -0.004 emu. After the field of 0.01 T is applied, the sample has a constant diamagnetism until approximately 15 K at which point the magnetization becomes less negative and by 16 K the magnetization is positive and is continuing to increase. The magnetization increases to a value of approximately 0.006 emu at 19 K at which point the value decreases to 0.0015 emu at 22 K. Above 22 K the magnetization remains constant at 0.0015 emu. When the sample is FC in 0.01 T to 2 K the results are different. As the temperature increases, **5** is paramagnetic with a magnetization of 0.009 emu. The magnetization is approximately constant to 15 K at which point M begins to decrease slowly followed by a rapid decrease at 19 K, until it reaches a constant value of 0.0015 emu at 22 K. The application of a magnetic field while cooling the sample (FC) quenches the diamagnetism, leaving the sample paramagnetic. ZFC and FC runs were performed on **5** in magnetic fields of 10 mT, 0.2 T, 0.5 T, 1 T, 2 T, and 5 T. The magnetization recorded after ZFC and FC are plotted in Figure 2-11 as the difference, $\Delta M_{FC\text{-}ZFC}$, of the ZFC and FC data. The data for **5** taken in the above six magnetic fields reveal that the transition temperature is shifted as the magnetic field strength is varied. When **5** is ZFC the diamagnetic state is quenched at lower temperatures in stronger magnetic fields.

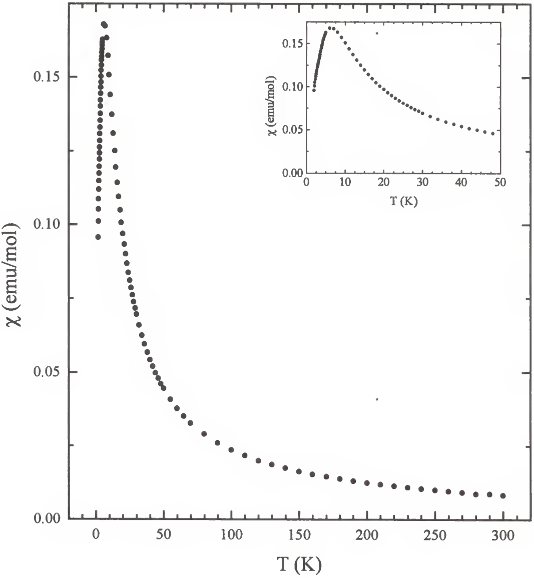

Figure 2-9. The temperature dependence of the magnetic susceptibility χ(T) for **8** measured in a field of 0.1 T. The data show Curie-like behavior down to low temperatures with a narrow maximum at 4.5 K evidence of weak antiferromagnetic correlations. No anomalous behavior exists at 22 K.

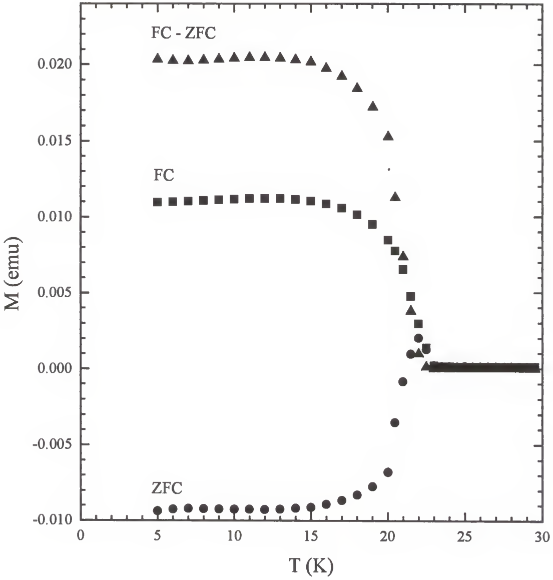

Figure 2-10. The FC and ZFC magnetization data for **5** measured in a magnetic field of 10 mT. The squares are the field cooled data, the circles are the zero-field cooled data, and the triangles are the field cooled data minus the zero-field cooled data. The point at which the slope of the curve changes is the transition point.

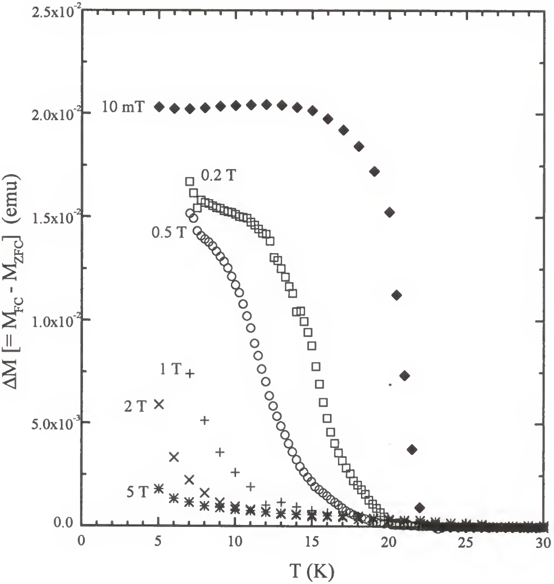

Figure 2-11. The difference magnetization ($\Delta M_{FC\text{-}ZFC}$) data for **5** measured in a magnetic fields of 10 mT, 0.2 T, 0.5 T, 1 T, 2 T, and 5 T. The point at which the slope of the curve changes is the transition point.

Synthesis and Structure of (4,4'-dimethyl-2,2'-bipyridine)trichloromanganese(III) acetonitrile solvate $[MnCl_3(dmbpy)]\cdot(CH_3CN)$ (6).

After the realization of the presence of a Haldane gap in an S = 2 quasi-linear antiferromagnetic chain material[26] our efforts focused on synthesizing novel S = 2 chain compounds which could be studied for their possible Haldane-like properties. Intuitively the quickest route to new materials was modification of existing S = 2 chain materials. For example, $[MnCl_3(bpy)]_n$ or $[MnCl_3(phen)]_n$ could be modified by adding substituents onto the bidentate ligands. This type of modification could be advantageous to the design of S = 2 linear chain Haldane gap materials. The addition of substituents to the peripherary of the bidentate ligands could increase the interchain distance, and spacing the chains further apart via bulkier ligands is one possible way to suppress long-range three-dimensional magnetic order.

In keeping with the systems we had already studied, we wished to modify existing manganese(III) linear chain compounds. Several manganese(III) antiferromagnetic chain compounds, including **4** and **5**, exist in the literature such as azido *bis*(pentane-2,4-dionato)manganese(III) $[Mn(acac)_2N_3]_n$,[79] (thiocyanato)*bis*(pentane-2,4-dionato)manganese(III) $[Mn(acac)_2NCS]_n$,[80] and *bis*(acetato)(N,N'-disalicylidene-2-hydroxy-propylenediamine)manganese(III) ($[Mn(2\text{-}OH\text{-}SALPN)OAc]_n$,[81] along with the two materials described previously in this work. Among all of the linear chain compounds listed here, only **4** and **5** do not order antiferromagnetically. Modification of the coordinating ligands in the materials which undergo antiferromagnetic order could alter the magnetic behavior, while modification of the known Haldane gap material **4** could enhance the features of the Haldane phase or possibly quench the phase. With these considerations in mind modification of the 2,2'-bipyridine ligand in **4** was undertaken.

Following the identical procedure used to isolate **4**, we attempted to isolate the dimethyl substituted bipyridine linear chain compound. After seven days of crystallization, large, black, needle-like crystals of **6** could be seen in the beaker. These crystals were collected on a Büchner funnel and washed with cold acetonitrile. After approximately five minutes of air drying the crystals had decomposed considerably. The initial conclusion was that the crystals were X-ray quality and more should be grown and collected in an inert atmosphere. The crystal structure of the black needle-like crystals was determined and the structure is shown in Figure 2-12, and the crystallographic data for **6** is contained in Appendix Tables A-1 through A-3.

The crystal structure shows the complex to be monomeric, five-coordinate and solvated by acetonitrile molecules. The complex is coordinated by three chloride ligands as well as one bidentate 4,4'-dimethyl-2,2'-bipyridine ligand and in the cavities between monomers reside acetonitrile solvent molecules. Also the 4,4'-dimethyl-2,2'-bipyridine ligand occupies one axial and one equatorial coordination site on the Mn(III) metal center. The fact that **6** has a distorted trigonal bipyramidal geometry is unusual considering that generally Mn(III) complexes are tetragonally distorted octahedron. Figure 2-13 shows a packing diagram of the complexes looking down the *a* axis. The five-coordinate manganese(III) molecules form columns separated by acetonitrile solvent molecules. The spacing between manganese(III) ions is not uniform. Within a column, adjacent complexes form dimer pairs. The distance between Mn(III) centers within a dimer unit is 6.704 (1) Å, while the distance between Mn(III) centers between dimers is 7.713 (1) Å. Another interesting feature of the columns is the alternating stacking motif adopted. This packing style has the $MnCl_3$ units alternating from one side to the other which causes the relatively planar 4,4'-dimethyl-2,2'-bipyridine ligands to stack on top of one another.

The strategy was to crystallize a new inorganic linear chain material whose chains were very well separated from one another to ensure no long-range order effects. The complex crystallized as a monomer, and one plausible explanation for this outcome is the geometry around the Mn(III) ion. A view of the crystal structure of the linear chain complex **4**, looking down the chain axis (*c* axis) shown in Figure 2-14, highlights the occupation of the equatorial positions by the bidentate bipyridine ligand and two chloride

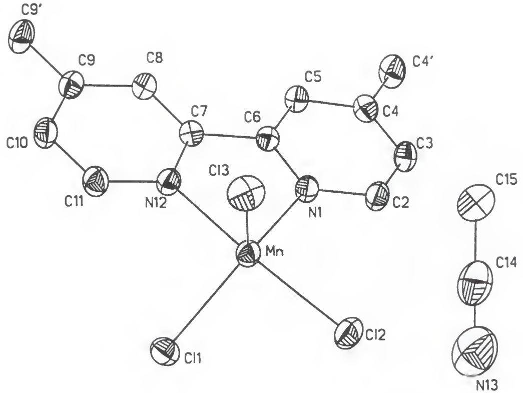

Figure 2-12. An ORTEP drawing of the crystal structure for **6**. The complex consists of five-coordinate Mn(III) ions with chloride anions occupying two equatorial sites and one axial site, while the 4,4'-dimethyl-2,2'-bipyridine ligand occupies both axial and equatorial coordination sites. Acetonitrile solvent molecules reside in the cavities between $MnCl_3$(dmbpy) complexes.

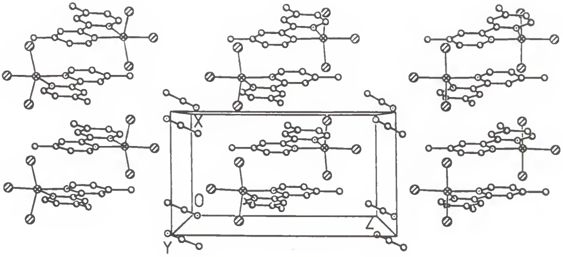

Figure 2-13. The packing diagram for **6** highlighting the columns of $MnCl_3$(dmbpy) complexes separated by acetonitrile molecules. The $MnCl_3$ units alternate from left to right while the dmbpy ligands stack on top of one another.

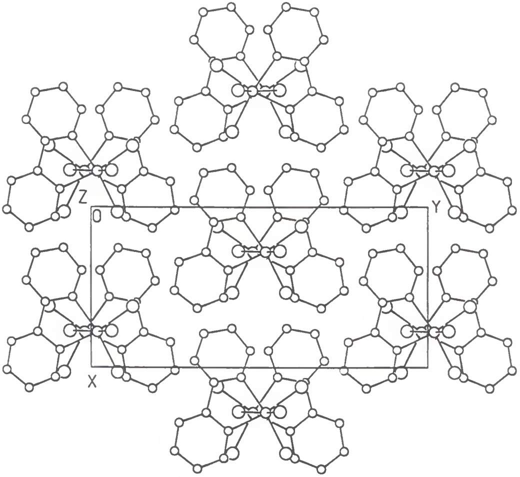

Figure 2-14. The packing diagram for **4** projected down the *a* axis. The 2,2'-bipyridine Ligands alternate from left to right and occupy equatorial coordination sites around the Mn(III) ions. This coordination arrangement allows for axial bridging of the Mn(III) centers via the chloride anions.

anions. To achieve a close-packed structure the bipyridine ligands alternate from side-to-side, leaving the remaining chloride anions in the axial positions available for bridging between Mn(III) centers. In **6** the 4,4'-dimethyl-2,2'-bipyridine ligand occupies axial and equatorial positions around the Mn(III) center. This does not rule out a linear chain structure as a possible configuration; it would be a zig-zag chain rather than a linear chain because the bridging chloride anions would be *cis* to one another, decreasing the Mn-Cl-Mn angle. A polymeric (chain) material was not attained, but a monomeric solvated structure formed. The geometry around each Mn(III) ion is trigonal bipyramidal, and each column is separated by acetonitrile molecules perhaps to stabilize the structure from an electrical charge point of view. The pendant chloride anions on adjacent chains face one another due to alternating stack motif within a single chain. The close proximity of "like" charges on the chloride anions would be unstable, and the material would likely not precipitate. With the inclusion of the acetonitrile solvent molecules the columns are separated by neutral species, shielding the terminal chlorides in adjacent stacks from one another.

Larger solvent molecules, such as butyronitrile and benzonitrile, were tried with the thought that they would separate the chains by an even larger distance which consequently might lead to the formation of chain structure. However, the formation of a chain complex was not the outcome. Complex **6** is unique from the view that it consists of five-coordinate Mn(III) ions with the bidentate ligand occupying both axial and equatorial positions, which alters the geometry resulting in a distorted trigonal bipyramidal structure.

Summary 2-4

Three manganese(III) complexes, $[MnCl_3(bpy)]_n$, $[MnCl_3(phen)]_n$, and $[MnCl_3(dmbpy)]\cdot(CH_3CN)$ were synthesized and studied by a variety of physical methods. All three structures have been characterized by X-ray crystallography with structures of the latter two complexes, $[MnCl_3(phen)]_n$, and $[MnCl_3(dmbpy)]\cdot(CH_3CN)$, solved as a part of the presented work.

$[MnCl_3(bpy)]_n$ is a linear chain, $S = 2$, Heisenberg system. Magnetic susceptibility on both single crystal samples and powder samples show the material to behave as a one-dimensional Heisenberg antiferromagnet. The high-field magnetization data show that at lowest fields **4** is diamagnetic but there exists a critical field, H_c, where the material becomes magnetic. The system shows no evidence for three-dimensional long-range antiferromagnetic order from both susceptibility and magnetization data down to 30 mK. The results are interpreted as the first evidence for a Haldane gap in an $S = 2$ chain antiferromagnet with a gap energy, Δ, of $\Delta_{S=2} = 0.07 \pm 0.02|J|$ which is in good agreement with the theoretical results.

$[MnCl_3(phen)]_n$ is also a Mn(III) $S = 2$ linear chain complex with supporting evidence from the X-ray crystallography data. $[MnCl_3(phen)]_n$, like $[MnCl_3(bpy)]_n$, is a one-dimensional Heisenberg antiferromagnet as seen by broad maximum at 100 K in the SQUID magnetometry, however, at approximately 20 K **5** shows a magnetic phase transition from an antiferromagnet coupled state (i.e. some nearest neighbor spins aligned antiparallel) to a state where the spins are tilted known as a "canted" antiferromagnet. The spin canting results in a net magnetic moment of 6.3×10^{-3} μ_B, which is consistent with "canted" antiferromagnetism. Magnetization data taken at a variety of magnetic field strengths show that **5** is diamagnetic at lowest temperatures (i.e. 2 K) and as the temperature increases the sample becomes magnetic, with each data set at each field strength having a characteristic critical temperature. Research is ongoing to determine if the origin of the diamagnetism in **5**.

The complex, $[MnCl_3(dmbpy)]\cdot(CH_3CN)$ was synthesized and its X-ray crystal structure solved. Complex **6** consists of monomeric five-coordinate Mn(III) units which form columns separated by acetonitrile solvent molecules. The material is unique from a geometric point of view. Most Mn(III) coordination complexes are six-coordinate octahedra. Complex **6**, however, is five-coordinate containing 4,4'-dimethyl-2,2'-bipyridine (dmbpy) ligands which occupy both axial and equatorial coordination sites. The $MnCl_3$ units alternate from left to right within a column so as to allow the 4,4'-dimethyl-2,2'-bipyridine ligands to stack on top of one another.

CHAPTER 3

NEW BEDT-TTF CATION-RADICAL SALTS INCORPORATING THE HYDROGEN DICHLORIDE ANION, α'-(BEDT-TTF)$_2$HCl$_2$, ε-(BEDT-TTF)HCl$_2$, AND ε'-(BEDT-TTF)HCl$_2$

3-1 Introduction

The organic π-donor *bis*(ethylenedithio)tetrathiafulvalene (BEDT-TTF) is the basis of a large number of conducting and superconducting cation-radical molecular solids.[3,27,43,82-85] Conductivity in these materials occurs via the donor-ion network[27,38] that results from close intermolecular contacts in the solid. The donor-ion networks are often stacks or sheets that are separated by layers of counterions. The most common route to pure crystalline samples of conducting cation-radical salts is through electrochemical oxidation of the donor in the presence of an appropriate counterion. Salts are generally formed where the oxidation state of the donor ranges from $+^1/_2$ to +1, and all of the current superconducting examples have donor oxidation states of $+^1/_2$ or $+^2/_3$.[4,84] Recently, in our lab the first dication salts of BEDT-TTF have been isolated as the tetrafluoroborate and perchlorate salts.[45,86] In these solids the donor BEDT-TTF exists only as the dication. The salts were prepared by electrocrystallization from an oxidizing solvent mixture such that BEDT-TTF is first chemically oxidized to the monocation in solution followed by electrochemical oxidation to the dication.

Solids where the donor oxidation state is between +1 and +2 could also be conductors with potentially interesting properties. These materials would have degrees of band filling different from the presently known materials. Good overlap between donors is necessary in order to achieve band formation, and it is clear based on the number of cation-radical salts that for small, monomeric anions, 2:1 and 3:1 donor:anion stoichiometries sufficiently provide the donor ion density needed to achieve good overlap. If high-oxidation state materials are to be isolated, the stoichiometries of these salts require divalent, trivalent, and tetravalent anions. A problem with incorporating these inorganic anions is producing a sufficient concentration of the anions in organic solvents. This is remedied with the use of alkali and alkali-earth metal salts and the appropriate crown ethers to pull the inorganic salts into the organic media.

Using the route to isolate the dication salts of BEDT-TTF, attempts to prepare further examples of high-oxidation state cation-radical salts have now resulted in the isolation of the first hydrogen dichloride (HCl_2^-) salts of BEDT-TTF. Two morphologies α'-$(BEDT\text{-}TTF)_2HCl_2$, **(9)**, ε-$(BEDT\text{-}TTF)HCl_2$, **(10)**, form simultaneously in the electrocrystallization cell. The 2:1 salt conforms to the α' morphology[42,87,88] found in BEDT-TTF cation-radical salts consisting of stacks of BEDT-TTF dimers twisted about the central C=C bond. The physical properties of the 2:1 salt are quite similar to the existing α'-$(BEDT\text{-}TTF)_2X$ salts,[42,87,88] and **9** incorporates the shortest linear anion in the series. Room temperature transport and temperature dependent magnetic susceptibility measurements show **9** is a weak semiconductor that behaves as a localized Mott-Hubbard system. Salt **10**, which belongs to the *C2/m* space group and conforms to the ε-morphology[50] found in BEDT-TTF materials, undergoes an anion ordering structural phase transition near 200 K resulting in a new low temperature phase ε'-$(BEDT\text{-}TTF)HCl_2$, **(11)** with space group $P2_1/c$. EPR integrated area and linewidth data for **10** show evidence of the anion ordering transition near 200 K. Below 170 K, **11** undergoes a paramagnetic to diamagnetic transition also seen in the EPR data. The HCl_2^- ion is linear in **9** but bent in **10** and **11**. The crystal structures and physical properties of the new hydrogen dichloride BEDT-TTF salts are described.

3-2 Experimental Section

Materials. BEDT-TTF was synthesized by the method of Larsen and Lenior.[89] Sodium phosphate (Na_3PO_4) and sodium chloride (NaCl) were obtained from Aldrich Chemical Co. (Milwaukee, WI) and used without further purification. Benzonitrile (C_6H_5CN, 99%), chloroacetylchloride ($ClCH_2COCl$, 98%), and 1,4,7,10,13-pentaoxacyclopentadecane or 15-crown-5 ($C_{10}H_{20}O_5$, 98%) were purchased from Aldrich Chemical Co. (Milwaukee, WI). Benzonitrile was purified by distillation and chloroacetylchloride and 15-crown-5 were used without further purification. Methylene chloride (CH_2Cl_2, 99.9%) was purchased from Fisher Scientific (Orlando, FL). Methylene chloride was dried over P_2O_5 and distilled before use.

Preparation of α'-(BEDT-TTF)$_2$HCl$_2$ **(9)** and BEDT-TTF(HCl$_2$) **(10)**. *Method 1:* BEDT-TTF (7.5 mg) was placed in the working arm of a two-electrode H-cell and dissolved in 30 mL of 9.75 mM sodium phosphate in 10% $ClCH_2COCl$/benzonitrile containing 10 drops of 15-crown-5. A constant current density of 0.90 μA/cm^2 was maintained at room temperature between the platinum working electrode and counter electrode that were separated by two glass frits. After a few days needles of **9** and platelets of **10** could be seen on the electrode surface and at the bottom of the H-cell. No phosphate containing salts were obtained, but small brown plates of **9** and large black needles of **10** were collected after 21 days. *Method 2:* BEDT-TTF (7.5 mg) was placed in the working arm of a two-electrode H-cell and dissolved in 30 mL of 11.4 mM sodium chloride in 10% $ClCH_2COCl$/methylene chloride containing 10 drops of 15-crown-5 and oxidized as described above. The cells were maintained at room temperature with a constant current density of 0.90 μA/cm^2, and as above, both crystal forms were observed within a few days and were harvested after 11 days.

Crystallographic data collection and structure determination. Crystallographic data for α'-(BEDT-TTF)$_2$HCl$_2$ **9**, ε-BEDT-TTF(HCl$_2$) **10**, and ε'-BEDT-TTF(HCl$_2$) **11** are listed in Appendix Tables B-1 through B-6. Data were collected at 113 K for **9**, at 233 K for **10**, and at 173 K for **11** on a Siemens SMART PLATFORM equipped with a CCD area detector and a graphite monochromator utilizing MoK$_\alpha$ radiation ($\lambda = 0.71073$ Å). Cell parameters were refined using 4947, 2211, and 6521 reflections for **9**, **10**, and **11**, respectively. A hemisphere of data for each structure (1381 frames) was collected using the ω-scan method (0.3° frame width). The first 50 frames were remeasured at the end of data collection to monitor instrument and crystal stability (maximum correction on I was < 1 %). Absorption corrections were applied based on the ψ-scan using the entire data sets.

All structures were solved by Direct Methods in *SHELXTL5*,[74] and refined using full-matrix least squares on F^2. In compound **9**, the asymmetric unit consists of one half a BEDT-TTF cation and one HCl_2 anion. The non-H atoms were refined with anisotropic thermal parameters whereas the H atoms were refined with isotropic thermal parameters, except those associated with C14 and C16. One of the -CH_2CH_2- (C14-C16) units in **9** is disordered and was refined in two partial units. Their site occupation factors refined to 0.76(1) and 0.24(1) and their H atoms were refined riding on the C atoms to which they are bonded. In compound **10**, the asymmetric unit consists of one quarter of a BEDT-TTF cation and a quarter of an HCl_2 anion, each located at a 2/m symmetry site. The CH_2 units are disordered and their occupation factors were fixed at 50% because of symmetry. The Cl atoms were also disordered and their occupation factors were fixed at 50% because of symmetry. The non-H atoms were treated anisotropically, whereas the hydrogen atoms were calculated in ideal positions and were riding on their respective carbon atoms. In compound **11**, the asymmetric unit consists of BEDT-TTF and HCl_2^- ion in a 1:1 ratio. The non-H atoms were treated anisotropically, whereas the hydrogen atoms were calculated in ideal positions and were riding on their respective carbon atoms.

EPR measurements. An aligned mosaic of crystals of **9** and a single crystal sample of **10** were mounted on a cut edge of a quartz rod and EPR spectra were recorded on a Bruker (Billerica, MA) ER-200D spectrometer modified with a digital signal channel and a digital field controller equipped with an Oxford Instruments (Witney, England) ITC 503 temperature controller and ESR 900 cryostat supplied with an AuFe/Ch thermocouple. The temperature-dependent electron paramagnetic resonance data were obtained at 9.27 GHz with 100 kHz modulation. Data were collected using a U.S. EPR (Clarksville, MD) SPEX300 data acquisition program.

SQUID magnetometry measurements. Susceptibility measurements were performed using a Quantum Design MPMS SQUID magnetometer operating at 0.1 T on 31.25 mg sample of salt **9**. A Teflon tube and plastic straw were used as sample holder during the measurements. The background signals arising from the Teflon tube and straw were measured independently and subtracted from the raw data. Due to the atmospheric instability of salts **10** and **11**, magnetic susceptibility measurements were not performed.

Transport measurements. Due to the instability of the materials in air and under evacuated conditions, room temperature conductivity was measured only on the most robust compound, **9**. The conductivity was measured by a four-probe method using narrow gauge (0.0127 mm diameter) gold wires affixed in a linear arrangement to a single plate-like crystal (0.59 x 0.45 x 0.03 mm^3) using fast-drying gold paint.

3-3 Results and Discussion

Synthesis of α'-(BEDT-TTF)$_2$HCl$_2$ (9)and ε-(BEDT-TTF)HCl$_2$ (10)

The BEDT-TTF hydrogen dichloride salts were isolated during attempts to synthesize high-oxidation state salts of BEDT-TTF with high-valent counterions. The currently known high-oxidation state salts of BEDT-TTF, where BEDT-TTF exists only as the dication,[45] include the tetrafluoroborate and perchlorate salts, with the perchlorate salt shown in Figure 3-1. Since the counterions are monovalent, a high density are needed to compensate charge resulting in a structure where each BEDT-TTF dication is surrounded by six counterions in a distorted octahedron. The high concentration of anions around each donor molecule gives poor contact along and between stacks of donors. Incorporation of high valent anions into the crystal lattice should provide charge compensation for the high-

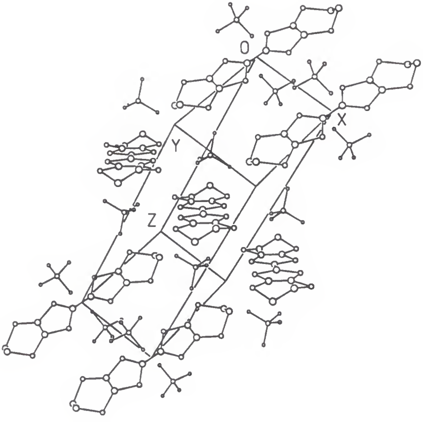

Figure 3-1. The packing diagram for the first dication salt of the π-electron donor BEDT-TTF, BEDT-TTF$(ClO_4)_2$, including both anions and cations. Taken from reference 45.

oxidation state of the donor cations without a large concentration of anion species in the lattice.

The hydrogen dichloride BEDT-TTF salts were first obtained from a standard constant-current electrocrystallization cell using a 10% $ClCH_2COCl$/benzonitrile solvent mixture with Na_3PO_4 as the supporting electrolyte. Salts **1** and **2** were subsequently prepared using a 10% $ClCH_2COCl$/methylene chloride solvent mixture with NaCl as the supporting electrolyte. The hydrogen dichloride anion is believed to form after reduction and homolytic bond cleavage of $ClCH_2COCl$ to generate a number of products including $Cl^{\cdot}$, Cl^-, and CH_2CO. Unlike experiments using ClO_4^- and BF_4^- electrolytes, no high-oxidation state salts were isolated instead, the 1:1 and 2:1 BEDT-TTF hydrogen dichloride salts precipitate with the hydrogen dichloride anion formed *in situ* .

Crystal Structure of α'-$(BEDT\text{-}TTF)_2HCl_2$ (9).

Crystals of α'-$(BEDT\text{-}TTF)_2HCl_2$, **9**, form as thin, square, brown plates and crystallize in the monoclinic space group *P2/c* . Figure 3-2 shows the packing diagram for **9** including both anions and cations, with crystallographic data contained in Appendix Tables B-1 through B-3. There are two characteristic features of the α'-$(BEDT\text{-}TTF)_2X$ salts. First, the BEDT-TTF cations form stacks of twisted dimers that align side-by-side to produce the donor ion sheet as illustrated in Figure 3-3 . Second, the counterions are linear and previously reported examples include symmetric or asymmetric triatomic ($AuBr_2^-$, $CuCl_2^-$, $IAuBr^-$), or pentaatomic ($Ag(CN)_2^-$, $Au(CN)_2^-$) anions.[42,87,88] Figure 3-4 plots cell volume versus anion length of the α'-$(BEDT\text{-}TTF)_2X$ materials. Compared to other α'-$(BEDT\text{-}TTF)_2X$ salts,[42,87,88] **9** incorporates the shortest linear anion (6.75 Å) in the series, and consequently the unit cell volume is the smallest in the series at 1523.90(4) $Å^3$. The unit cell axes *a, b,* and *c* are all shorter in length than the other α'-$(BEDT\text{-}TTF)_2X$ materials indicating that the "chemical compression" of the unit cell is nearly isotropic as illustrated in Figure 3-5. Figure 3-6 shows the intermolecular interactions within the BEDT-TTF network of cations. There are short S···S contacts within the twisted dimers

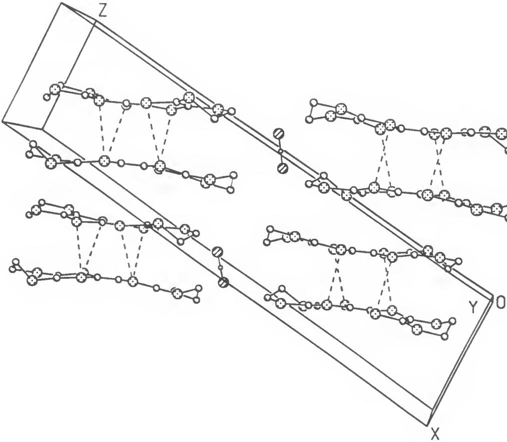

Figure 3-2. The packing diagram for **9** including both anions and cations. Sheets of BEDT-TTF cations are separated by layers of hydrogen dichloride anions. The hydrogen dichloride anions are symmetric and linear. The cation sheets are composed of columns of BEDT-TTF$^{+1/2}$ dimers. There is poor orbital overlap between cations within a column, while there is good overlap between cations in adjacent columns within the sheet.

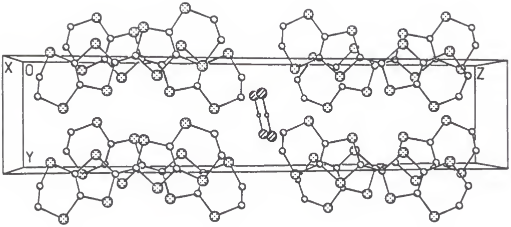

Figure 3-3. A view of **9** down the *a* axis showing that the BEDT-TTF dimers are not in registry, but are twisted about the central fulvalene C=C bond. This type of dimer arrangement is characteristic of α'-(BEDT-TTF)$_2$X salts.

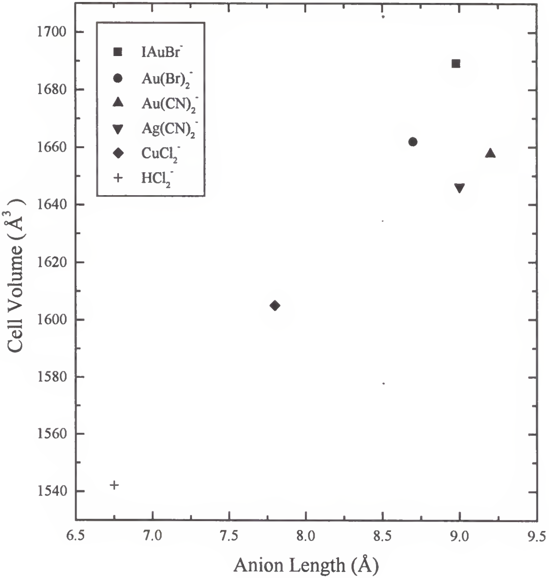

Figure 3-4. Plot of unit cell volume vs. anion length in the α'-(BEDT-TTF)$_2$X salts.

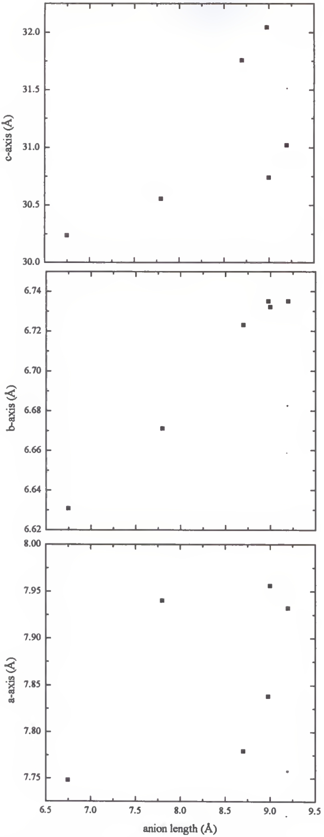

Figure 3-5. Anion length dependence of the unit cell axes lengths *a*, *b*, and *c* for the α'-(BEDT-TTF)$_2$X salts.

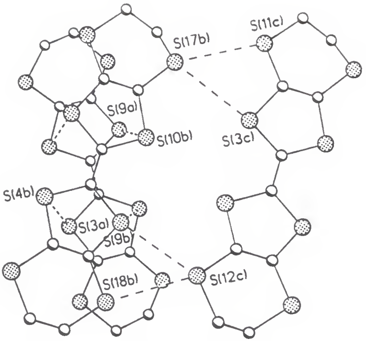

Figure 3-6. A view of three BEDT-TTF ions, at 113 K, in **9** looking nearly down the stacking axis showing the intra- and intermolecular S···S close contacts.

Table 3-1. Inter- and intrastack S···S contact distances at 113 K for **9**.

Interstack S···S Contacts*	**Distance (Å)**
S3c - S17b	3.450
S9b - S12c	3.388
S11c - S17b	3.429
S12c - S18b	3.406
Intrastack S-S Contacts*	
S3a - S4b	3.560
S9a -S10b	3.601

*Refer to Figure 3-6.

(intrastack), but the twist, together with poor contact between dimer pairs along the stack, results in poor overlap along the *a* axis of the α'-(BEDT-TTF)$_2$X phases.[42] Between adjacent BEDT-TTF cation stacks (interstack contacts), there are many S···S contacts less than twice the van der Waals radii sum of sulfur (3.6 Å) between inner and outer ring S atoms. The contacts, due to the parallel and coplanar arrangement of BEDT-TTF cations, lead to quasi-one-dimensional electronic and magnetic descriptions of the α'-(BEDT-TTF)$_2$X phase.[42,90] Salt **9** has a hydrophobic environment surrounding each hydrogen dichloride anion with numerous Cl-H interactions between the anion and the ethylene hydrogen atoms on the BEDT-TTF cations. This arrangement forms a cage around each HCl_2^- ion that helps stabilize the anion. The few known examples of salts of the hydrogen dichloride anion all have a similar hydrophobic environment that has been suggested as a necessary requirement for its stabilization.[91-94]

Donor-ion bond lengths have been used to assign oxidation states in charge-transfer salts of BEDT-TTF.[95-99] The central C=C bond of the fulvalene core of BEDT-TTF is most sensitive to changes in oxidation state, increasing in length with higher oxidation states. The central C=C bond length of 1.371(4) Å for **9** is consistent with a donor oxidation state of +1/2 and the 2:1 stoichiometry observed with the HCl_2^- counterion.

Transport Properties of α'-(BEDT-TTF)$_2$HCl$_2$ (9).

The room temperature conductivities of the α'-(BEDT-TTF)$_2$X salts where X = $AuBr_2^-$, $Ag(CN)_2^-$, $CuCl_2^-$, and $IAuBr^-$ are ~0.1, ~0.03, ~0.04, and $1.5 \times 10^{-4}\ \Omega^{-1}\cdot cm^{-1}$, respectively.[88,90] The transport properties and the magnetic properties of the α' materials are indicative of semiconducting behavior. The room temperature four-probe resistance measurement on a single crystal of **9** shows that the hydrogen dichloride salt is also semiconducting with a value of $6 \pm 2 \times 10^{-4}\ \Omega^{-1}\cdot cm^{-1}$.

Magnetic Susceptibility and EPR Data for α'-(BEDT-TTF)$_2$HCl$_2$ (9)

The temperature dependence of the molar susceptibility, $\chi(T)$, for **9** is plotted in Figure 3-7. The data have been corrected for a diamagnetic core contribution, calculated

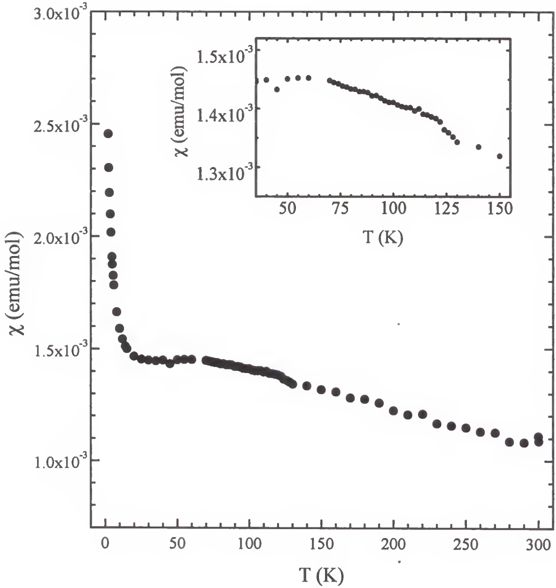

Figure 3-7. The temperature dependence of the magnetic susceptibility $\chi(T)$ measured in a magnetic field of 1 kG for a 31.25 mg batch of randomly oriented crystals of **9**. The $\chi(T)$ results show paramagnetic behavior at high temperatures with a broad maximum near 65 K, characteristic of short range antiferromagnetic coupling in low-dimensional systems, and a strong upturn for $T < 30$ K due to paramagnetic impurities from decomposition of the hydrogen dichloride anions.

using Pascal's constants,[7] of 433.5 x 10^{-6} emu/mol for α'-(BEDT-TTF)$_2$(HCl$_2$). The room temperature value for the corrected susceptibility is 1.1 x 10^{-3} emu/mol for **9** which is slightly smaller than the "spin-only" value of 1.25 x 10^{-3} emu/mol for an S = 1/2 spin system. The lower χ(300K) value is evidence of antiferromagnetic exchange between (BEDT-TTF)$^{+}{}_2$ dimers. Three temperature regimes are apparent in the static susceptibility data plotted in Figure 3-7. The susceptibility increases gradually as the temperature is lowered from room temperature down to 125 K (region 1) where there is a slight jump in χ. Between 125 K and 30 K (region 2), χ goes through a broad maximum centered near 65 K. At the lowest temperatures (T < 20 K), the data are dominated by a Curie-like impurity (region 3). The three regimes present in the susceptibility data for **9** correlate with the electron paramagnetic resonance (EPR) integrated signal area (which is proportional to the spin magnetic susceptibility), and linewidth (ΔH_{p-p}) data which are plotted in Figures 3-8 and 3-9. The EPR data were measured from 4 to 298 K of an aligned mosaic of crystals with the static magnetic field approximately perpendicular to the crystallographic *a* axis. As the temperature is lowered, the area increases gradually from room temperature down to 125 K (region 1). Below 125 K the area decreases by a factor of two to a minimum at 50 K (region 2),while below 40 K (region 3) the integrated area data are dominated by a Curie-like impurity. The linewidth is independent of temperature in region 1 with a value of 39 G. As the temperature is lowered through region 2, the linewidth gradually decreases to 31 G at 40 K, followed by a rapid decrease in region 3 to 7.08 G at 4 K, also a consequence of the Curie-like impurity. Normal linewidth behavior for the α' materials[42] is a constant linewidth until antiferromagnet correlations begin to take affect at which point the linewidth broadens due to anisotropic magnetic exchange among BEDT-TTF dimers in the one-dimensional columns and the two-dimensional sheets. In **9** the antiferromagnet correlations are masked by the Curie-like impurity which alternatively causes the linewidth to decrease.

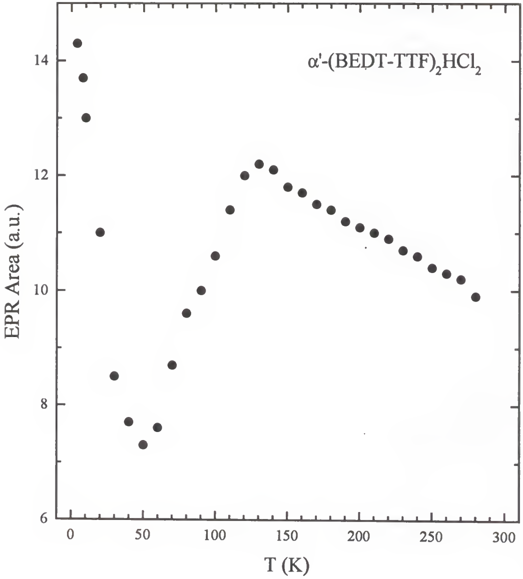

Figure 3-8. Temperature dependence of the integrated area of the EPR resonance for an aligned mosaic of crystals of **9** with the static magnetic field perpendicular to the crystal faces.

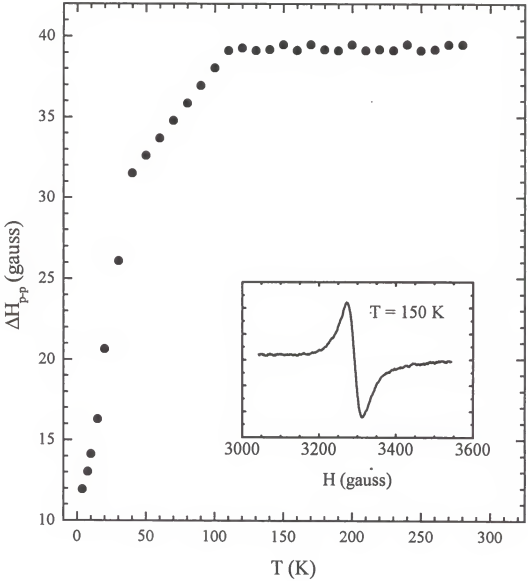

Figure 3-9. The EPR linewidth, $\Delta H_{p\text{-}p}$, for an aligned mosaic of crystals of **9** with the static magnetic field perpendicular to the crystal faces. A representative EPR spectrum at 150 K is shown in the inset .

To investigate the origin of the 125 K anomaly seen in the magnetic data, the X-ray structure was redetermined at 113 K. The low temperature X-ray structure reveals no major changes relative to the structure determined at 173 K. In particular the BEDT-TTF terminal ethylene groups are still disordered at 113 K. All of the crystallographic axes undergo a slight compression by a few tenths of an angstrom which shorten the $S\cdots S$ contacts between BEDT-TTF cations. However, we cannot say if the slight compression is associated with the magnetic anomaly at 125 K.

The previously studied members of the α'-(BEDT-TTF)$_2$X family have all been described as localized Mott-Hubbard systems with antiferromagnetic exchange between (BEDT-TTF)$^+_2$ dimers.[42] Compound **9** behaves similarly. In molecular conductors such as the BEDT-TTF cation-radical salts, the conduction electrons are delocalized over all the BEDT-TTF molecules in the lattice. The electrons occupy sites in the conduction band and are promoted to empty levels above the Fermi level (highest occupied level) resulting in conduction. If the energy of an electron sitting below the Fermi level is lower (more stable) than the energy needed for promotion, the electron will remain on that site. The electron is said to be localized.[1] Localization of the conduction electrons results in a decrease in conductivity which can lead to a metal-to-insulator transition. Two important types of electron localization in solid-state materials are Anderson and Mott-Hubbard localization. Anderson-type localization occurs as a result of impurities in the lattice. This type of localization is frequent in non-crystalline, amorphous solids, but could occur in crystalline samples of low purity. Mott-Hubbard localization is frequently seen in crystalline solids such as the BEDT-TTF salts. Take a system with a conduction band that has N levels which can hold two electrons each. If the system has N electrons then its band is half full. A Mott-Hubbard transition occurs when there is large on-site electron-electron Coulomb repulsion which disfavors doubly occupied sites. These repulsions result in an energy gap opening at the Fermi level with reorganization of the electrons, each site now being singly occupied forming an antiferromagnetically coupled insulator.[1] The energy of this arrangement is lower than the energy required to promote electrons to unoccupied sites, so the electrons are said to be localized. Conduction now must be activated by an electron "hopping" mechanism. The α'-(BEDT-TTF)$_2$X family of materials form (BEDT-TTF)$^+{}_2$ dimers, and due to large Coulomb repulsion the electrons are localized on the dimers resulting in an antiferromagnetic array of electrons with activated conduction (i.e. semiconductors).[42]

The room temperature EPR linewidth of 39 G is consistent with the other α'-(BEDT-TTF)$_2$X salts.[42,100] The gradual increase in χ(T) to a broad maximum as the temperature is lowered is a characteristic of antiferromagnetic interactions in a low-dimensional lattice and is also seen in other α'-(BEDT-TTF)$_2$X salts.[42] Although the general features are present, the susceptibility data are not easily fit to the commonly employed models for ideal one-dimensional chains or two-dimensional quadratic layer antiferromagnets. The data are complicated by the transition at 125 K, the thermal compression of the lattice at low temperature, and the considerable impurity contribution that arises from the unstable HCl_2^- anion. Nevertheless, the conductivity and magnetic data are similar to the other α'-(BEDT-TTF)$_2$X salts.

Despite the complications in the data some attempts to fit the data for **9** are shown in Figure 3-10. The two-dimensional Quadratic Layer Heisenberg Antiferromagnet, (QLAF)[101] model was employed in these fits. The QLAF model is based on the Heisenberg Hamiltonian defined as

$$H = 2J\sum \vec{S}_i\vec{S}_{i+1} \tag{3-1}$$

where J is the nearest neighbor Heisenberg exchange constant and $\vec{S}_i$ and $\vec{S}_{i+1}$ are nearest neighbor spins. The experimental magnetic data for **9** have been fit to the two-dimensional QLAF model[101] written as

$$Ng^2\mu_B^2 / \chi|J| = 3\theta + \sum_{n=1}^{\infty} C_n / \theta^{n-1} \tag{3-2}$$

where N is the number of spins, μ_B is the Bohr magneton, k is the Boltzmann constant, $\theta = k\,T/|J|S(S+1)$, and the plot is a series expansion to six terms in J/T using the constants calculated by Rushbrook and Wood for an S = 1/2 system, while the low temperature data, 4 - 25 K, have been fit to the Curie law. To obtain the QLAF fit the experimental g value of 2.002 was used and the values for $2J$ were varied. Two fits were performed, one which was the sum of the QLAF expression and a Curie (C/T) contribution, and a second expression made up of three terms. Respectively, these fitting expressions may be written as

$$\chi_{total} = \chi_{Curie} + \chi_{QLAF} \tag{3-3}$$

$$\chi_{total} = \chi_o + \chi_{Curie} + \chi_{QLAF} \tag{3-4}$$

where χ_o is a temperature independent paramagnetism term, χ_{Curie} accounts for any Curie (C/T) behavior and χ_{QLAF} is the QLAF term from Equation 3-2. The best fit of the data using Equation 3-3 had a magnetic exchange energy of $2J = 114 \pm 5$ K ($J = 57$ K)and Curie constant $C = 0.02$ emu-K/mol, while using Equation 3-4 $\chi_o = 1.42 \times 10^{-4}$ emu/mol, $2J = 131 \pm 5$ K ($J = 65$ K), and $C = 0.0257 \pm 0.001$ emu-K/mol. These values are slightly larger than those reported by Obertelli *et al.* for the other α'-(BEDT-TTF)$_2$X salts (e.g. $J = 35$ - 56 K). Again, the considerable impurity contribution that arises from the unstable HCl_2^- anion may erroneously contribute to the larger value of J. However, the short length of the hydrogen dichloride anion allowing for a large degree of lattice compressibility along with the numerous close intermolecular S···S contacts could both

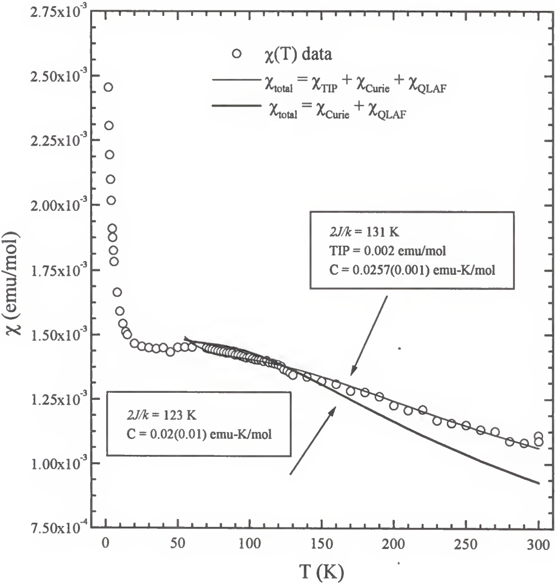

Figure 3-10. Fits of the susceptibility data for **9** using Equations 3-3 (dark solid line) and 3-4 (solid line).

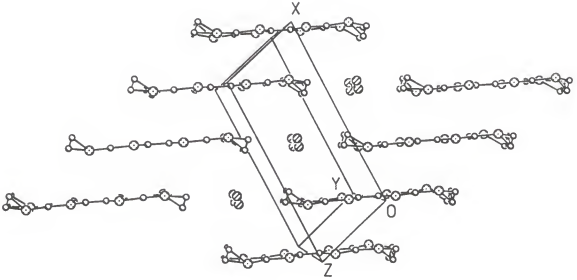

Figure 3-11. The packing diagram for **10** including both anions and cations. There are columns of BEDT-TTF cations with hydrogen dichloride anions sitting between the columns.

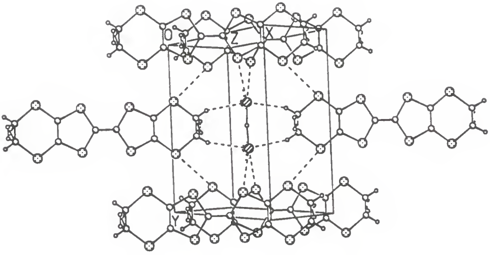

Figure 3-12. Another view of the crystal structure for **10**. The BEDT-TTF monocations pack in a bond-over-ring arrangement. Each HCl_2^-anion is surrounded by a hydrophobic pocket formed from ethylene hydrogen atoms and sulfur atoms of the BEDT-TTF molecules. The CH_2 units of the cations are disordered about the mirror plane and the HCl_2^-anions are disordered about a center of inversion.

serve to enhance antiferromagnetic coupling at higher temperatures resulting in a larger exchange constant.

Crystal Structure of ε-BEDT-TTF(HCl_2) (10).

Crystals of **10** form as shiny, black, four-sided needles that are air-sensitive and degrade within minutes of exposure to air. Crystallographic data taken at 233 K for **10**, which crystallizes in the monoclinic space group *C2/m* , are presented in Appendix Tables B-4 through B-6. Figures 3-11 and 3-12 show two perspectives of the lattice packing diagram for **10** looking down the *b* and *c* axes, respectively. At 233 K, all BEDT-TTF monocations are equivalent, and the unit cell consists of two BEDT-TTF cations and two hydrogen dichloride anions, all located on *2/m* sites. The terminal ethylene groups and the hydrogen dichloride anions are disordered. The salt is isostructural with the previously described salts ε-(BEDT-TTF)PF_6,[56] ε-(BEDT-TTF)ClO_4,[50] and ε-(BEDSe-TSeF)PF_6.[102] As for α'-$(BEDT\text{-}TTF)_2(HCl_2)$ **9**, the BEDT-TTF central C=C bond distance can be used to confirm the oxidation state of the BEDT-TTF cations in **10**. The central C=C bond distance is 1.388(4) Å, which is consistent with a donor oxidation state of +1 in tetrathiafulvalene based molecules. There is one short side-to-side contact between an outer-ring S atom in one stack with an outer-ring S atom of an adjacent stack, but no close contacts less than the van der Waals radii sum for sulfur exist between BEDT-TTF monocations within a stack. The absence of close contacts within a stack of BEDT-TTF donor molecules is probably due to the large Coulomb repulsions between +1 cations. The hydrogen dichloride anion is unstable as apparent from the highly air-sensitive nature of the needles. Upon contact with air the needles quickly form a brown crust on the exterior, while reduced pressure environments also initiate decomposition.

Magnetic Properties of ε-(BEDT-TTF)HCl_2 (10).

EPR data were obtained for a single crystal of salt **10.** Figure 3-13 illustrates the integrated EPR signal area and linewidth, $\Delta H_{p\text{-}p}$, for **10** that were measured between 4 K and 298 K with the static magnetic field approximately perpendicular to the crystallographic

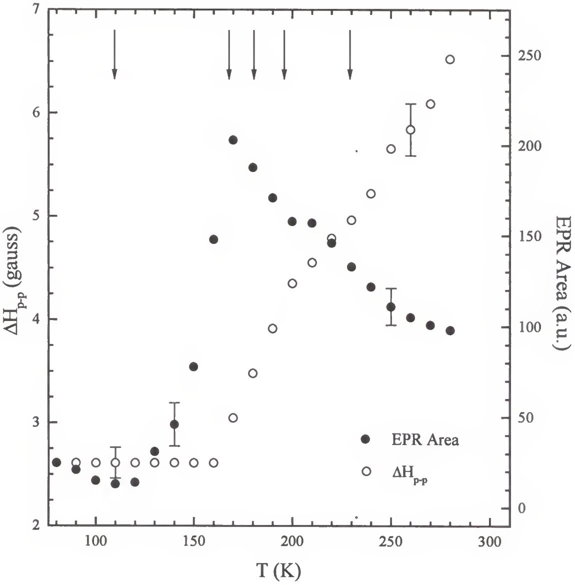

Figure 3-13. The EPR integrated area (filled circles) and the linewidth, $\Delta H_{p\text{-}p}$, (open circles) data for a single needle-like crystal of **10**. The anomaly seen near 200 K in both the integrated area and linewidth is associated with the anion ordering transition. The magnetic phase transition is seen near 170 K. At the lowest temperatures (down to 4 K, not shown) the data are dominated by a Curie-like impurity with constant linewidth. The arrows indicate temperatures at which crystallographic data were obtained.

c axis. The integrated area, which is proportional to the spin magnetic susceptibility, rises gradually with decreasing temperature from 298 K to 200 K, where a small kink appears. The integrated area continues to rise as the temperature is lowered to 170 K, below which point it drops sharply to a minimum at 120 K. The integrated area remains constant to about 90 K, where, at lower temperatures, an increase in the area gives evidence of a Curie-like impurity, presumably resulting from decomposition of the hydrogen dichloride anion. The EPR linewidth as a function of temperature shows a gradual decrease as the temperature is lowered from 298 K, followed by a sharper decrease at 200 K until a minimum at 160 K is reached. At temperatures below 160 K the linewidth remains constant down to 4 K. Examination of the EPR integrated area and linewidth data show evidence of two phase transitions, one near 200 K which has a minor effect on the magnetic structure and a magnetic phase transition between 160 and 170 K. The three regions present in the integrated area data correlate with the three regions in the linewidth data for **10**.

Crystal Structure of ε'-(BEDT-TTF)HCl_2 (11).

To investigate the nature of these transitions, a second crystal structure was solved at 173 K and the unit cell was monitored at 113 K, 185 K, and 200 K. The 173 K structure reveals a new phase for which the crystallographic data are included in Appendix Tables B-7 through B-9. Structure **11** belongs to the $P2_1/c$ space group in contrast to the high temperature phase, **10**, which crystallizes in *C2/m*. The cell dimensions are nearly equal for the two structures except for a doubling of the *c* axis in **11**. The structure still contains columns of HCl_2^- anions and slipped stacks of BEDT-TTF cations in a bond-over-ring arrangement (Figure 3-15).

The major change is ordering of the HCl_2^- ions and the terminal ethylene groups, which is illustrated in Figures 3-14 and 3-15. The HCl_2^- ions now alternate between two orientations giving rise to the doubling of the unit cell (Figure 3-15). The HCl_2^- anion is bent with an Cl-H-Cl angle of 164°. There are several short Cl···S and Cl···H contacts

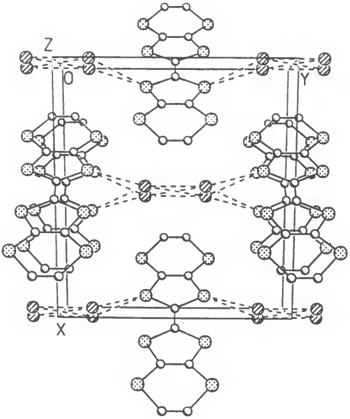

Figure 3-14. The crystal structure of **10** determined at 233 K. The terminal BEDT-TTF ethylene groups are disordered about the mirror plane and HCl_2^- anions are disordered about an inversion center. One short intermolecular S···S contact exists between outer ring sulfur atoms shown by the dashed lines.

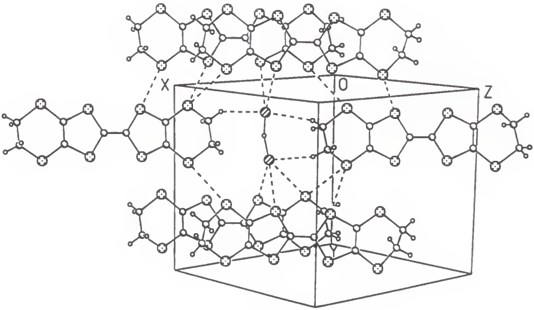

Figure 3-15. The crystal structure of ε'-(BEDT-TTF)HCl$_2$, **11**, determined at 173 K. Salt **3** crystallizes in the monoclinic $P2_1/c$ space group. The terminal ethylene groups of the BEDT-TTF cations and the HCl$_2^-$ anions are ordered. Several close intra- and intermolecular S···S contacts exist between outer ring and inner ring sulfur atoms on adjacent BEDT-TTF cations, and each HCl$_2^-$ anion sits in a hydrophobic pocket. The HCl$_2^-$ ion is bent.

between hydrogen dichloride anions and BEDT-TTF cations. The BEDT-TTF ion network is nearly the same as in **10**, although a slight displacement of the donor ions leads to additional intermolecular close contacts. In structure **10**, one type of $S \cdots S$ interaction exists that involves outer ring sulfur atoms on adjacent BEDT-TTF cations (Figure 3-14). In structure **11**, two types of interactions exist, one between outer ring sulfurs and another between inner and outer ring sulfurs on adjacent BEDT-TTF cations. Because of the similarity between the two phases, we refer to the low temperature phase as ε'-BEDT-TTF(HCl_2).

A unit cell determination shows the ε-phase exists at 200 K while the ε'-phase is present at 185 K. These results indicate the inflections seen in the EPR area and linewidth data near 200 K are related to the anion ordering structural phase transition. The anion ordering has only a minor effect on the magnetic interactions. On the other hand, the magnetic phase transition seen near 170 K in the EPR does not involve a structural change. A unit cell determination at 113 K reveals the ε'-phase, **11**, indicating that the same phase is present at 113, 173, and 185 K. The nature of the 170 magnetic phase transition remains unclear. Magnetic ordering or a solid-state disproportionation reaction are possibilities that could lead to the loss of paramagnetism seen below 170 K. Unfortunately, the extreme air sensitivity of the salt has thus far precluded more detailed investigations of the physical properties.

Description of the HCl_2^- Anion.

Salts of the hydrogen dichloride ion are unusual but precedented.[91-94] The relatively few HCl_2^- salts known are listed in Table 3-2. Hydrogen dichloride salts all tend to lose HCl rather readily, and some are very unstable towards moisture and oxygen. Salts **9** and **10** described in this work are both extremely air and moisture sensitive. Compound **9** is a shiny brown solid while **10** forms a shiny black solid, and each material maintains its integrity if kept in an inert environment. A brown crust forms if the crystals are exposed to air.

Table 3-2. Bond lengths and angles for the HCl_2^- anion in ionic solids.

Compound	H-Cl(1) (Å)	H-Cl(2) (Å)	Cl-H-Cl Angle
[K·18-Crown-6] HCl_2 [a]	1.56	1.56	180°
[Mg·18-Crown-6] $(HCl_2)_2$ [a]	1.30 1.47	2.03 1.65	161° 168°
[H_3O·18-Crown-6] HCl_2 [b]			
[$PCl_2CH_3C_6H_5OCH_3$] HCl_2 [c]	1.45	1.78	168°
CsCl·1/3H_3O HCl_2 [d]	1.57	1.57	180°
α'-(BEDT-TTF)$_2$$HCl_2$ [e]	1.57	1.57	180°
ε'-(BEDT-TTF)HCl_2 [e]	1.62	1.51	164°

a) Reference 94.
b) Reference 93.
c) Reference 92.
d) Reference 91.
e) This work.

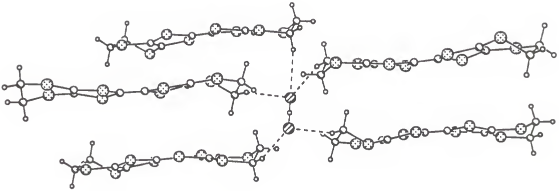

Figure 3-16. Side view of the 2:1 salt **9** showing the hydrophobic pocket holding the hydrogen dichloride anion. The HCl_2^- anion is linear with equal Cl-H bond distances of 1.57 Å and a Cl-H-Cl bond angle of 180°. There are numerous intermolecular contacts between the chlorine atoms of the anions and the ethylene hydrogen atoms and the sulfur atoms of the BEDT-TTF cations.

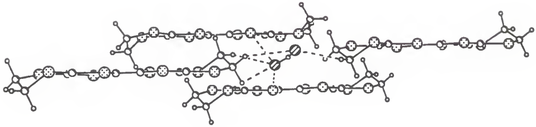

Figure 3-17. Side view of the 1:1 salt **11** looking down the short axis of the BEDT-TTF molecules, also showing the hydrophobic pocket holding each HCl_2^- anion. The HCl_2^- anion has a Cl-H-Cl angle of 164° with Cl(1)-H and Cl(2)-H distances of 1.51 Å and 1.62 Å, respectively.

The previously isolated hydrogen dichloride salts contain molecular cations that form hydrophobic pockets for the anion. The one exception, $(CsCl\cdot 1/3H_3O)HCl_2$,[91] has hydronium cations as well as cesium cations stabilizing the HCl_2^- anion. The HCl_2^- environment in **9** and **11** can be seen in Figures 3-2 and 3-3 and 3-15, respectively, and additional perspectives are shown in Figures 3-16 and 3-17 where close contacts between the anion and donor cations are indicated. It is the BEDT-TTF terminal ethylene hydrogen atoms, as well as the BEDT-TTF sulfur atoms (low electronegativity and high polarizability), which provide the hydrophobic setting needed to stabilize the anion.

Table 3-2 also summarizes the H-Cl bond lengths and Cl-H-Cl bond angles of the known HCl_2^- examples. The nature of the cation influences the geometry of the anion. It has been hypothesized that strong interaction between the HCl_2^- chlorine atoms and the positive counterions results in asymmetry in the HCl_2^- anion.[93,94] In these cases, the H-Cl(1) and H-Cl(2) bond distances are not equal and the Cl-H-Cl bond angle is less than 180°.[93,94] In compound **9** the hydrogen dichloride anions are symmetric and linear (H-Cl(1), H-Cl(2): 1.57 Å; Cl-H-Cl: 180°), whereas in salt **11** the distances are not equal and the anion is nonlinear (H-Cl(1):1.62 Å; H-Cl(2):1.51 Å; Cl-H-Cl: 164°). These differences in the hydrogen dichloride anion bond distances and bond angles can be attributed to the different charges on the BEDT-TTF cations. The more highly charged +1 cation in salt **11** has a greater interaction with the anion than the +1/2 cation in salt **9**. In **9**, the anion-cation contacts are all through the terminal ethylene groups while in **11** there are several close Cl-S contacts in addition to the $Cl-CH_2$ contacts.

3-4 Summary

To summarize, three new salts of the π-donor *bis*(ethylenedithio)tetrathiafulvalene (BEDT-TTF) α'-$(BEDT\text{-}TTF)_2HCl_2$, ε-BEDT-TTF(HCl_2), and ε'-BEDT-TTF(HCl_2) have been characterized. The α'- and ε-phase materials were grown from the same electrocrystallization cell. The ε' salt is a low-temperature phase of ε-BEDT-TTF(HCl_2)

that results from an anion ordering transition. These three cation-radical salts are the first examples of BEDT-TTF salts isolated with the hydrogen dichloride (HCl_2^-) anion.

The mode of BEDT-TTF packing in these systems helps to stabilize the rather unstable HCl_2^-. If the appropriate hydrophobic environment around the anion can be formed, ionic salts, and in our case molecular solids, can precipitate. Each hydrogen dichloride anion is surrounded by numerous BEDT-TTF cations providing the hydrophobic environment needed for stabilization. Depending on the stoichiometry of the salt, the hydrogen dichloride anion will either be symmetric and linear or asymmetric and nonlinear. The HCl_2^- anion is linear in salt **9**, while it is bent in both salts **10** and **11**. Despite the hydrophobic environment around the hydrogen dichloride anions in these salts, all of the materials are extremely sensitive to air and evacuated conditions, and must be collected and stored under an inert atmosphere to keep their integrity.

The transport and magnetic susceptibility measurements are consistent with a description of nearly localized $(BEDT\text{-}TTF)_2^+$ radicals showing **9** is a localized Mott-Hubbard system, similar to the other α'-$(BEDT\text{-}TTF)_2X$ salts. EPR integrated area and linewidth data for **10** show evidence of the structural transition observed in the X-ray data near 200 K, while it undergoes a paramagnetic to non-magnetic transition below 170 K.

CHAPTER 4
A NEW ORGANIC METAL BASED ON THE ORGANIC DONOR BEDO-TTF AND THE N, N', N"-TRICYANOGUANIDINATE DIANION, $(BEDO\text{-}TTF)_4[C_4N_6]\cdot H_2O$

4-1 Introduction

Since the discovery of superconductivity in tetramethyltetraselenafulvalene perchlorate, $(TMTSF)_2ClO_4$,[36] there has been interest in developing further examples of organic molecular conductors and superconductors. Cation-radical salts based on the donor *bis*(ethylenedithio)tetrathiafulavalene (BEDT-TTF) have been the most fruitful class of materials, from which over 50 superconductors are currently known.[4] Among the BEDT-TTF cation-radical salts, κ-$(BEDT\text{-}TTF)_2Cu[N(CN)_2]Cl$, has the highest ambient pressure superconducting transition temperature with $T_c = 12.8$ K.[43]

Many other organic donor molecules have been developed for the purpose of preparing molecular conductors.[4] One of the more interesting is *bis*(ethylenedioxy) tetrathiafulvalene, (BEDO-TTF) (**12**), shown in Figure 4-1, first prepared by Suzuki *et al.* in 1989.[64] Substitution of sulfur by oxygen in the outer ring of BEDO-TTF lowers the oxidation potential and increases electron density on the TTF core while keeping the size and shape of the molecule the same.[65] There are now many BEDO-TTF based cation-radical salts including two superconductors.[66,103-108] Interestingly, despite the similar size and shape of the donors, BEDO-TTF cation-radical salts form with different crystal packing motifs than those seen with BEDT-TTF.

Several of the known conducting BEDO-TTF salts possess organic acceptors or organic anions. Horiuchi recently reported crystal structures of several new BEDO-TTF

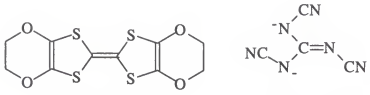

BEDO-TTF (**12**) $C_4N_6^{-2}$ (**13**)

Figure 4-1. Chemical structures of the organic donor BEDO-TTF, **12**, and the N,N',N"-tricyanoguanidinate dianion, **13**.

cation-radical salts including four with cyano-rich organic anions.[66] While the monoanion cyanoform ($C_4N_3^-$) forms a 5:2 salt, the monoanion 1,1,2,3,3-pentacyanopropenide ($C_8N_5^-$) forms a 2:1 salt, and both systems are conducting. BEDO-TTF forms 4:1 salts with dianions, hexacyanotrimethylenemethandiide ($C_{10}N_6^{-2}$, HCTMM^{-2}) and *tris*(dicyanomethylene)cyclopropandiide ($C_{12}N_6^{-2}$, HCP^{-2}). Both of these 4:1 salts are metallic as well.

The dianion N,N',N"-tricyanoguanidinate **13** was recently described by Subrayan *et al.*[109] as part of studies into molecules containing only carbon and nitrogen. The dianion **13** has alternating C-N connectivity with an open chain structure rather than the cyclic aromatic triazine structure common among high nitrogen compounds. Subrayan *et al.* describe a facile preparation of **13** which can be isolated as the sodium or potassium salt.[109] Considering the novel dianion to be potentially useful as a counterion for preparing cation-radical salts, we have used **13** in electrocrystallization cells with the donor BEDO-TTF. The title compound, $(BEDO\text{-}TTF)_4[C_4N_6]\cdot H_2O$ (**14**), has been isolated and is a new example of a BEDO-TTF molecular conductor. Compound **14** incorporates the N,N',N"-tricyanoguanidinate dianion, and adopts the "I_3" packing motif[66] found in other BEDO-TTF cation-radical salts. The BEDO-TTF donor molecule network consists of two-dimensional arrays separated by infinite sheets of N,N',N"-tricyanoguanidinate dianions which form dimers through hydrogen bonding with water molecules.

(BEDO-TTF)$_4$[C_4N_6]·H_2O is metallic from room temperature down to approximately 8 K. Below 8 K the salt undergoes a metal-to-insulator transition due to conduction electron localization. The electromagnetic response of **14** was investigated using a tunnel diode resonating circuit which monitored the change in the resonant frequency as a function of temperature. The results show an increase in the resonant frequency below approximately 8 K which is consistent with an increase in the skin depth of **14** due to a metal-to-insulator transition. The EPR and magnetic susceptibility data for **14** between room temperature and 50 K are typical of Pauli temperature independent paramagnetism seen in metallic species at high temperatures, while below 50 K the data are consistent with the gradual localization of the conduction electrons. Results of the synthesis, crystal structure, magnetic and transport properties and how they compare to other BEDO-TTF salts are the subjects of this chapter.

4-2 Experimental Section

Materials. BEDO-TTF was synthesized by the method of Suzuki.[65] Disodium N,N',N"-tricyanoguanidinate ($Na_2C_4N_6$·H_2O) was received from Professor Paul Rasmussen,[109] and was used without further purification.
1, 4, 7 ,10 , 13-pentaoxacyclopentadecane or 15-crown-5 ($C_{10}H_{20}O_5$, 98%) was purchased from Aldrich Chemical Co. (Milwaukee, WI). Methylene chloride (CH_2Cl_2, 99.9%) and ethanol (C_2H_5OH, absolute) were purchased from Fisher Scientific (Orlando, FL). Methylene chloride was dried over P_2O_5 and distilled before use, while ethanol and 15-crown-5 were used without further purification.

(BEDO-TTF)$_4$[C_4N_6]·H_2O (14). BEDO-TTF (7.0 mg) was placed in the working arm of a two-electrode H-cell and dissolved in 30 mL of 9.75 mM disodium N, N', N"-tricyanoguanidinate in 15% CH_3CH_2OH/methylene chloride containing 20 drops of 15-crown-5. A constant current density of 0.70 $\mu A/cm^2$ was maintained at room temperature between the platinum working electrode and counter electrode that were separated by two glass frits. After a few days elongated plates of **3** could be seen on the electrode surface and at the bottom of the H-cell. Large (typically 2.5 x 1.0 x 0.5 mm^3) black plates of **3** were collected after 21 days.

Crystallographic data collection and structure determination. Data for **14** were collected at 173 K on a Siemens SMART PLATFORM equipped with a CCD area detector and a graphite monochromator utilizing MoK_α radiation ($\lambda = 0.71073$ Å). Cell parameters were refined using up to 8151 reflections. A hemisphere of data (1381 frames) was collected using the ω-scan method (0.3° frame width). The first 50 frames were remeasured at the end of data collection to monitor instrument and crystal stability (maximum correction on I was < 1 %). ψ-scan absorption corrections were applied based on the entire data set.

The structure was solved by Direct Methods in *SHELXTL5*,[74] and refined using full-matrix least squares. The asymmetric unit consists of four BEDO-TTF molecules, one N,N',N"-tricyanoguanidinate ion, and a disordered water molecule (site occupation factors are 0.49(4) and 0.51(4) for O1 and O1', respectively). The H atoms of the partial water molecules are not disordered. They were obtained from a difference Fourier map, and their coordinates were refined while their isotropic thermal parameters were calculated at 1.5 of that of the O atoms. One end of one of the BEDO-TTF molecules is disordered with one CH_2-CH_2 unit having a refined occupation factor of 0.59(2) and the other 0.41(2). All non-H atoms were treated anisotropically, whereas the hydrogen atoms were calculated in ideal positions and were riding on their respective carbon atoms. A total of 774 parameters were refined in the final cycle of refinement using 5824 reflections with $I > 2\sigma(I)$ to yield R_1 4.61% and wR_2 of 10.12%, respectively. Refinement was done using F^2.

EPR measurements. Electron Paramagnetic Resonance (EPR) spectra of **14** were recorded between 4 and 298 K using a Bruker (Billerica, MA) ER-200D spectrometer modified with a digital signal channel and a digital field controller equipped with an Oxford Instruments (Witney, England) ITC 503 temperature controller and ESR 900 cryostat supplied with an AuFe/Ch thermocouple. A single crystal of **14** (1.5 x 1.0 x 0.5 mm^3)

was selected and mounted on a cut edge of a quartz rod; rotation was achieved using a home-built goniometer. The sample was first mounted vertically in the microwave cavity. The 0° and 90° orientations correspond to the parallel and perpendicular alignments, respectively, of the crystal *ab* plane with respect to the static magnetic field. The sample was also oriented horizontally in the microwave cavity, with the microwave electric field parallel to the crystal *ab* plane and the static magnetic field perpendicular to the crystallographic *c* axis. The temperature-dependent EPR data were obtained at 9.27 GHz with 100 kHz modulation. Data were collected using a U.S. EPR (Clarksville, MD) SPEX300 data acquisition program.

SQUID magnetometry measurements. The temperature dependence of the magnetic susceptibility between 300 K and 5 K was obtained from magnetization measurements made using a Quantum Design MPMS SQUID magnetometer on a 4.5 mg sample of randomly oriented single crystals of **14**. A #5 gel capsule and plastic straw were used as sample holder during the measurements. The background signals arising from the gel capsule and straw were measured independently and subtracted from the raw data.

Transport measurements. Temperature dependent (4 K - 298 K) resistivity measurements were made using a four-probe technique. Four gold contacts (~ 3000 Å thick) in a linear arrangement were deposited on a single plate-like crystal ($2.5 \times 0.9 \times 0.2$ mm^3) of **14** by thermal evaporation, and narrow gauge (0.0127 mm diameter) gold wires were affixed to the contacts using fast-drying silver paint. The sample was fastened onto a chip-holder which attaches to our home-built low temperature dipstick. A typical run was done by first cooling the sample to the lowest temperature and collecting data while warming. Temperature stability obtained in this set-up has been determined to be ± 0.5 K or better over the temperature range measured. Lower temperatures were achieved by using a home-built dilution refrigerator.[110]

Tunnel diode oscillator (TDO) measurements. The electromagnetic response of a single crystal of **14** was investigated by means of a simple inductor-capacitor (LC) tank circuit whose response was driven by a tunnel diode.[111,112] The sample was placed inside the inductance coil and the entire circuit was fastened onto a chip-holder which attaches to our home-built low temperature dipstick.[110] A typical run was done by first cooling the sample to the lowest temperature and collecting data while warming. A wire sample of a known superconductor was measured independently to calibrate $\Delta f/f$. The empty coil was run to get the background signal which was temperature independent, and this background signal was subsequently subtracted from the raw data for **14**.

4-3 Results and Discussion

Synthesis and Structure of (BEDO-TTF)$_4$[C_4N_6]·H_2O (14)

The title compound was precipitated from a constant-current electrocrystallization cell using a low concentration solution of $Na_2C_4N_6 \cdot H_2O$ and 15-crown-5 in a 15% CH_3CH_2OH/methylene chloride solvent mixture. (BEDO-TTF)$_4$[C_4N_6]·H_2O forms as elongated plates which are shiny and black. The X-ray structure was determined at 173 K, and crystallographic data are presented in Appendix Tables C-1 through C-3. Figure 4-2 shows a packing diagram of **3** perpendicular to the long axis of the BEDO-TTF molecules. The unit cell consists of four equivalent BEDO-TTF$^{+1/2}$ cations, one N,N',N"-tricyanoguanidinate dianion, and one water solvent molecule. BEDO-TTF molecules align side-by-side to form a two-dimensional array within the *ab* plane as shown in Figures 4-3 and 4-4. As is typical for BEDO-TTF cation-radical salts, the sheets of BEDO-TTF cations are separated by sheets of the counterion. The central C=C bond length is 1.372 Å which is considerably longer than 1.342 Å, characteristic of the neutral BEDO-TTF molecule.[113] The central C=C bond can be correlated to the charge on the molecule just as in the donor *bis*(ethylenedithio)tetrathiafulvalene (BEDT-TTF). The highest occupied molecular orbital (HOMO) of the BEDO-TTF molecule is centered on the C=C bond, so oxidation of the molecule results in a lengthening of the C=C bond. The

C=C distance 1.372 Å present in **14** is consistent with those found in other cation-radical salts containing BEDO-TTF$^{+1/2}$ cations.[113]

The N,N',N"-tricyanoguanidinate dianions form sheets parallel to the *ab* plane that separate the donor layers. The anion sheets accommodate one water solvent molecule per dianion, and the water molecules are disordered. The tricyanoguanidinate dianions form dimers through hydrogen bonding with the water molecule as shown in Figure 4-5. Each water molecule makes two hydrogen bonds, one to a terminal nitrogen on one dianion and one to a central nitrogen atom on the other dianion. The dimers pack side-by-side in the *ab* plane forming an infinite two-dimensional sheet. Subrayan *et al.* point out that **13** is planar with a propeller-like shape.[109] In **14** the central CN_3 unit is planar with all three N-C-N angles adding up to 360°; however, the outer portion of each leg of the propeller is slightly out of the plane. This deviation causes each dianion to be puckered, and within a dimer unit one dianion is puckered upward while the other downward. This effect occurs in order to accommodate the hydrogen bonds through the two water molecules. In addition there are **14** numerous donor-anion interactions present via·ethylene hydrogen atoms on the BEDO-TTF cations and the nitrile groups on the anions which contribute to the puckering of the dianions.

Of the two previously described cation-radical salts with cyano-based dianions, the title compound is isostructural with (BEDO-TTF)$_4$(HCTMM)$\cdot$2CH$_2$ClCHCl$_2$.[66] The mode of cation packing in (BEDO-TTF)$_4$[C$_4$N$_6$]$\cdot$H$_2$O is commonly seen in BEDO-TTF cation-radical salts and has been designated the "I$_3$" motif by Horiuchi *et al.* after the prototype (BEDO-TTF)$_{2.4}$I$_3$.[66,103] Band structure calculations by Kahlich *et al.*[114] on (BEDO-TTF)$_2$ReO$_4\cdot$H$_2$O, another salt with the "I$_3$" motif, have shown that this packing motif gives rise to a two-dimensional Fermi surface. The other cyano-based dianion salt (BEDO-TTF)$_4$[HCP]$\cdot$2C$_6$H$_5$CN is also metallic, but forms with a different packing motif designated "HCP" by Horiuchi.[66] Two characteristic features of the BEDO-TTF cations can explain the two-dimensional nature of the donor layer. First, the small size of the

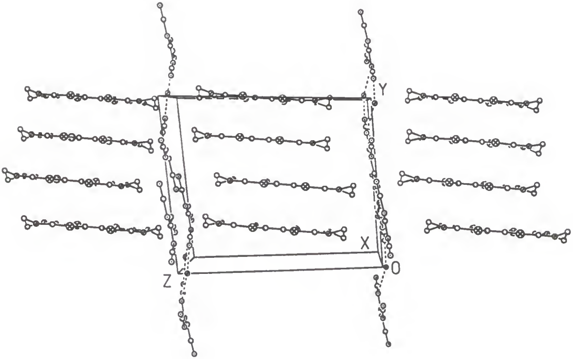

Figure 4-2. The packing diagram for **14** including both anions and cations. There are stacks of BEDO-TTF cations separated by layers of the N, N', N''-tricyanoguanidinate dianion $(C_4N_6)^{2-}$.

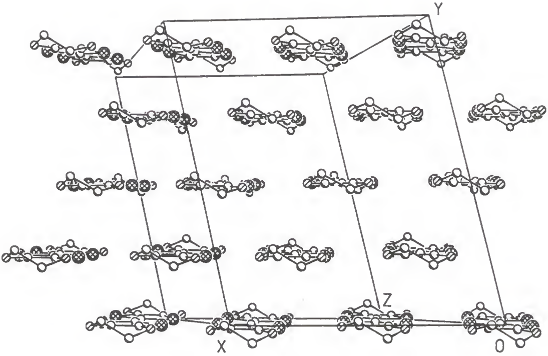

Figure 4-3. A projection of the BEDO-TTF cation layer looking down the long axis of the BEDO-TTF molecule. BEDO-TTF molecules pack in a slipped-stack, bond-over-ring arrangement. Good orbital overlap exists among donor molecules within one column as well as between adjacent columns.

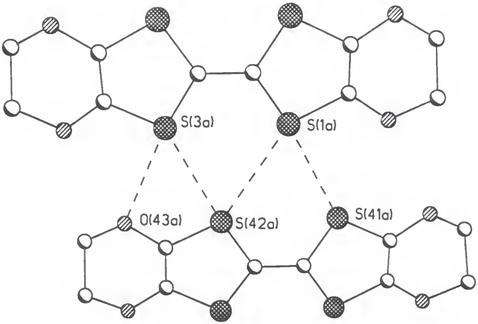

Figure 4-4. A side-by-side arrangement of two BEDO-TTF donor molecules from **14** highlighting the close S···O, and S···S contacts found in the salt.

Table 4-1. Table of important S···O, and S···S contacts found in **14**.

Contact	Distance (Å)
S(3a) - O(43a)	3.218
S(3a) - S(42a)	3.315
S(1a) - S(42a)	3.486
S(1a) - S(41a)	3.362

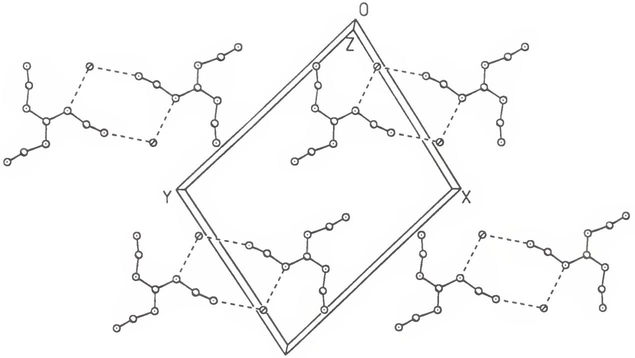

Figure 4-5. The N, N', N"-tricyanoguanidinate dianion layer. The $(C_4N_6)^{2-}$ anion is planar with a triskelion shape. Two dianions hydrogen bond with two water solvent molecules forming an infinite sheet of dianion dimer pairs.

oxygen atoms allows for close contacts between inner sulfur (S_{in}) atoms on adjacent BEDO-TTF molecules, which increases intermolecular orbital overlap. Second, the considerably large electronegativity of the oxygen atoms initiates the formation of many C-H···O interactions among the donor molecules. These weak "hydrogen bonds"[104] not only increase the orbital overlap between adjacent BEDO-TTF cations driving the material to form a two-dimensional array, but the C-H···O interactions also fix the BEDO-TTF cations in one uniform packing arrangement. One idea that may explain the prevalence of the "I_3" morphology in the BEDO-TTF family of salts is the rigidity of the terminal ethylene groups on the donor molecules.[66] Unlike the organic π-donor (BEDT-TTF), the inflexibility allows for only one conformation of the ethylene groups which allows little variation in packing of the BEDO-TTF molecules. Also, as stated above, the high electronegativity of the oxygen atoms initiates the formation of many C-H···O interactions among the donor molecules which fix the BEDO-TTF cations in one uniform packing arrangement, the "I_3" motif.

Transport Properties of (BEDO-TTF)$_4$[C_4N_6]·H_2O **(14)**.

The organic donor BEDO-TTF has a strong tendency to form organic donor-acceptor complexes and cation-radical salts which exhibit metallic conductivity down to low temperatures (< 20 K).[66,67,115] This tendency to form metals is ascribed to the strong intermolecular interactions normally seen in BEDO-TTF donor layers that gives rise to wide conduction bands. Although BEDO-TTF salts are frequently metallic conductors, the large bandwidths present in BEDO-TTF materials have led to fewer examples of superconductivity.[104,106] Wide bands result in a small density of states (DOS) at the Fermi level, while narrow bands have a larger DOS at the Fermi level. Recall that the transition to the superconducting phase occurs via electron pairs called Cooper pairs. The number of electrons available for pairing at the Fermi level is crucial for the phase transition to the superconducting state. Though it may sound counter-intuitive, poor metals (narrow bands)

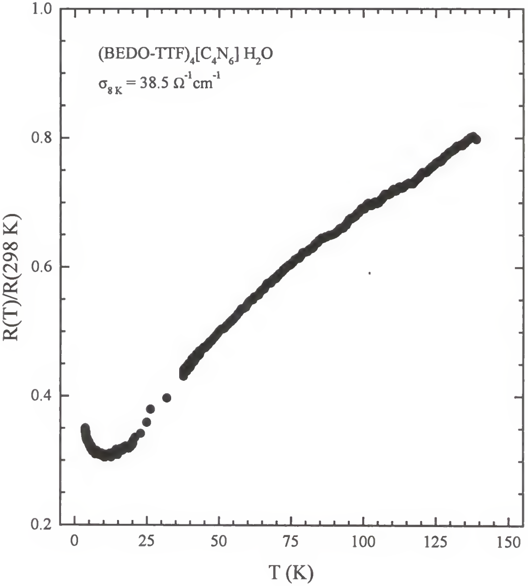

Figure 4-6. Temperature dependence of the resistivity normalized to the room temperature value for a single crystal of **14**.

are more suited to undergo a superconducting transition than robust metals (wide bands) because of the larger density of states at the Fermi level.

Conductivity data for **14** are shown in Figure 4-6. (BEDO-TTF)$_4$[C_4N_6]·H_2O is metallic at room temperature with $\sigma_{298K} = 11.5$ S cm^{-1}. As the temperature is decreased, the complex remains metallic down to 8 K ($\sigma_{8K} = 38.5$ S cm^{-1}) where a strong upturn in resistivity occurs indicating the occurrence of a metal-to-insulator transition. Resistivity data taken down to 100 millikelvin show the insulating behavior persists with no evidence of a superconducting transition. Low temperature metal-to-insulator transitions have been seen in numerous other BEDO-TTF cation-radical salts.[66] In the case of **14**, the metal-to-insulator transition appears to be due to localization of the conduction electrons. However, the type of metal-to-insulator transition is not known. Recall the types of localization described in Chapter 3, Mott-Hubbard, Anderson, weak, and strong.[1] The majority of metal-to-insulator transitions observed in organic metals of BEDT-TTF and BEDO-TTF are the Mott-Hubbard type seen in crystalline materials, where the electrons are localized to reduce the electron-electron Coulomb repulsion, resulting in an antiferromagnetically coupled insulating ground state. Anderson type localization, observed normally in non-crystalline materials due to defects and impurities, cannot be ruled out. Even though single crystals are used in the transport analysis, microcracks and impurities could lead to an Anderson type localization.

The resistivity versus temperature data plotted in Figure 4-6 reveal an approximately linear decrease in resistivity as the temperature is lowered. To investigate the resistance behavior of **14** more thoroughly, the data were plotted as ln R versus ln T shown in Figure 4-7. Such a plot will highlight deviations from linearity that do not appear in R vs. T plots. The data were probed for anomalies between 70 K and 50 K. The EPR integrated area and magnetic susceptibility, *vide infra*, increase between 70 K and 50 K indicative of the onset of conduction electron localization. The ln R vs. ln T plot shown in Figure 4-7 reveals a linear decrease in resistance in the 70 - 50 K temperature range. A change in the slope of the line in the plot would help define the onset temperature for electron localization in **14**. The R vs. T plot unambiguously points out the metal-to-insulator transition at 8.5 (± 1) K, however the temperature of the onset of electron localization is not observable from the resistance data.

Tunnel Diode Oscillator (TDO) Results for $(BEDO\text{-}TTF)_4[C_4N_6]\cdot H_2O$ (**14**).

The tunnel diode oscillator (TDO) experiment is a method used traditionally by solid-state chemists to screen single-crystal samples for superconducting transitions,[111,112] but we have utilized the method for characterization of the metal-to-insulator transition observed in **14**. The TDO experiment is extremely useful due to the quick results obtained. The method employs an *LC* circuit with an inductance coil connected in series with a tunnel diode. The sample is placed in the inductor and a small potential is applied across the diode generating a small oscillating current. The electromagnetic response produced inside the coil resonates at a frequency, f_o. Changes in the arrangement of the magnetic flux through the inductor result in changes in the resonant frequency. The magnetic flux will vary when phenomena such as superconducting transitions or metal-to-insulator transitions occur. More specifically, changes in the penetration depth, λ, due to a superconducting transition or changes in the skin depth, δ, due to a metal-to-insulator transition will cause a change in the inductance which in turn results in a shift in the resonance frequency. It can be shown that the change in frequency of the oscillator is given by

$$\frac{\Delta f}{f_o} = \frac{\pi r_s \Delta\delta}{A} \tag{4-1}$$

where $\Delta f = f(T_{\min}) - f(T)$, $f_o = f(T_{\min})$, r_s is the radius of the sample, A is the cross-sectional area between the coil and the sample, and δ is the skin depth of the metal. The geometry factors are independent of temperature, therefore, the equation says that $\Delta f / f$ is proportional to $\Delta\delta(T)$.[112]

A single crystal of **14** was placed in the TDO coil and the frequency was monitored as a function of temperature, with the results plotted in Figure 4-8 as $\Delta f / f_o$ versus T. Below 5 K, $\Delta f / f_o$ is relatively constant, withstanding the noise, while above 5 K the resonant frequency decreases to approximately 8.5 (± 1) K above which temperature the resonant frequency remains constant. Below the metal-to-insulator transition at 8.5 K the skin depth of **14** is essentially the thickness of the sample. This is a consequence of the insulating properties of **14** at these temperatures. Insulators allow electromagnetic radiation to penetrate unobstructed through them. However, at the onset of the insulator to metal transition above 5 K the resonant frequency decreases as the skin depth decreases. As the metallic nature of **14** increases the reflectivity also increases, narrowing the skin depth, and impeding the passage of electromagnetic radiation through the sample. The change in the skin depth of the metal causes a change in inductance which in turn results in a shift in the resonant frequency. Above 8.5 (± 1) K, the skin depth of **14** does not change significantly so the resonant frequency is relatively constant. The TDO experiment by itself is not conclusive evidence for a superconducting transition or a metal-to-insulator transition. The TDO must be done in conjunction with the transport measurement to obtain valid conclusions. Our resistivity data plotted in Figure 4-6 show an increase in resistivity in the same temperature regime (8 K) as the shift in f_o. Therefore, the TDO response is signaling an increase in skin depth accompanying the increased resistivity of the sample as the temperature is lowered through the metal-to-insulator transition. The information obtained from the TDO experiment on **14** is additional evidence supporting our conclusion that a metal-to-insulator transition occurs near 8 K.

EPR Results for (BEDO-TTF)$_4$[C$_4$N$_6$]·H$_2$O (14).

Electron paramagnetic resonance (EPR) data were obtained with a single crystal of **3** from 4 to 298 K. EPR spectra at 280 K, 50 K, and 4 K are shown in Figure 4-9. The EPR lineshape is Lorenztian at all temperatures, becoming Dysonian[116] below 100 K. The characteristic feature of the Dysonian lineshape is the asymmetry of the resonance due to

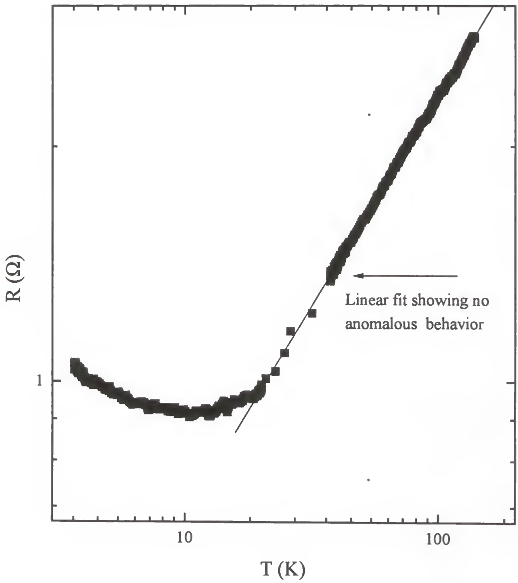

Figure 4-7. A log R versus log T plot for **14** showing no anomalous behavior in the high temperature range that would indicate conduction electron localization. The high temperature data are linear.

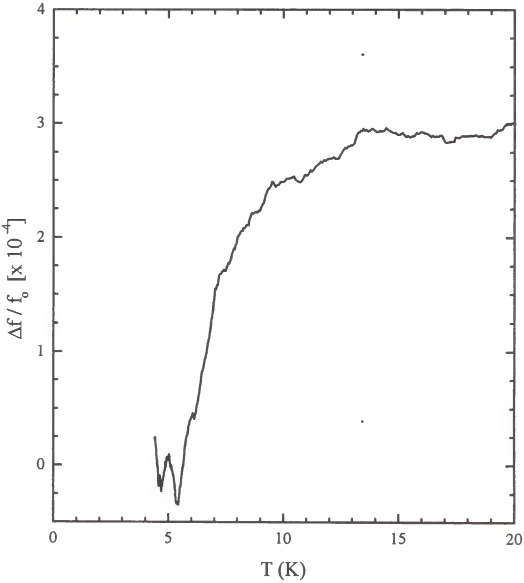

Figure 4-8. The relative change in frequency, $\Delta f/f = [f(T_{\min}) - f(T)/f(T_{\min})]$, as a function of temperature for **14** at approximately 2 MHz. The transition temperature is 8.5 (± 1) K in good agreement with the resistivity data.

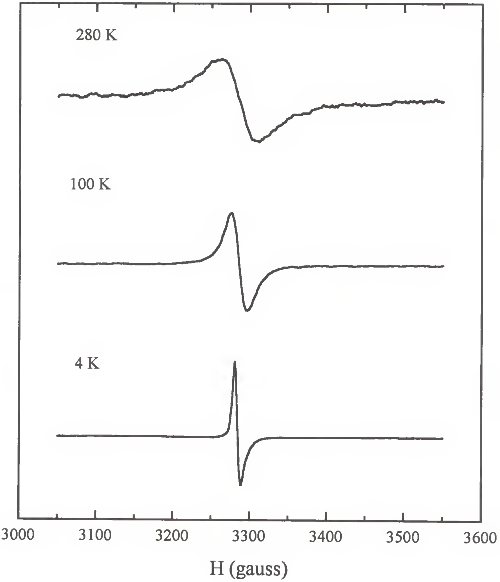

Figure 4-9. Representative EPR spectra of **14** at 298 K, 50 K, and 4 K. All spectra are Lorentzian with increasing Dysonian (asymmetric) character as the temperature is decreased.

skin depth effects.[117] Edmonds *et al* .[117] define the skin depth as the attenuation distance observed when an electromagnetic wave at microwave frequency enters a metallic specimen. The skin depth, δ,[117] is given by

$$\delta = \left(\frac{c^2 \varepsilon_o \rho}{\pi \nu} \right)^{1/2} , \tag{4-2}$$

where c is the speed of light, ε_o the vacuum permittivity, ρ the electrical resistivity of the metallic specimen, and ν the frequency of the microwave radiation. In the EPR experiment only those electrons residing within the skin depth are sampled, implying that if the actual sample size exceeds the skin depth the signal observed is due to only a portion of the entire specimen. The above equation shows that the skin depth is inversely proportional to the electrical resistivity. The electrical resistivity for a metallic specimen decreases as the temperature is decreased which consequently decreases the skin depth.

Another way of looking at this phenomenon is to recall that metals are reflective and this reflectivity increases as the conductivity increases. The higher the reflectivity, the narrower the skin depth will become. The decrease in skin depth reduces the number of electrons exposed to the microwave field which in turns reduces the power *absorbed* by the sample. The first derivative signal obtained from an EPR experiment, if symmetric, is due solely to the absorptive part of the Lorentzian function, but if the resonance is asymmetric (i.e. Dysonian) the observed signal becomes a mixture of both absorptive and dispersive components of the Lorentzian function. Symmetric EPR signals are common in non-metallic materials, whereas metallic species normally have asymmetric signals. Corrections to remove the dispersive component must be made in order to obtain the *absorptive* only resonance. The *absorption* only spectrum[118] can be obtained using

$$
\begin{aligned}
&P = A\frac{d}{dy}\left(\chi'\right) + B\frac{d}{dy}\left(\chi''\right)\\
&\text{where } \chi' = -\left(\frac{y}{1+y^2}\right) \quad \chi'' = \left(\frac{1}{1+y^2}\right)\\
&\text{and } y = T_2\gamma\left(H_o - H\right)
\end{aligned}
\tag{4-3}
$$

where P is the power absorption, χ' is the dispersive term and χ'' is the absorptive term, A and B are the fractions of dispersion and absorption, T_2 is the spin lifetime, γ is the gyromagnetic ratio, H_o is the microwave cavity resonant magnetic field, and H is the measured field. Once the effect of reduced skin depth and the removal of the dispersive portion of the signal are accounted, the resulting integrated area of the EPR signal as a function of temperature for the metallic species should behave Pauli-like (i.e. independent of temperature).

Figure 4-10 plots the temperature dependence of the EPR linewidth ($\Delta H_{p\text{-}p}$) calculated from the absorption component from 4 to 298 K, with the static magnetic field perpendicular to the *ab* plane of the crystal (i.e. the crystal face), determined from the absorption portion of the spectra.[118] (BEDO-TTF)$_4$[C$_4$N$_6$]·H$_2$O exhibits a linear decrease in linewidth from 52.2 G at 298 K to 7.8 G at 4 K. The higher dimensionality of the two-dimensional organic conductors based on BEDT-TTF and BEDO-TTF versus the one-dimensional conductors based on TTF and TMTSF results in broader linewidths for the two-dimensional materials when compared to the one-dimensional materials.[4] The increased dimensionality resulting from close interstack contacts in the two-dimensional systems serves to broaden the linewidths. In the present case, the title compound exhibits an extremely broad room temperature linewidth presumably due to the highly two-dimensional nature of the BEDO-TTF cation layer. It is noteworthy that the EPR linewidth of organic conductors is narrow in comparison to highly dimensional inorganic magnetic materials. The narrowness of the EPR linewidths in organic conductors in comparison to

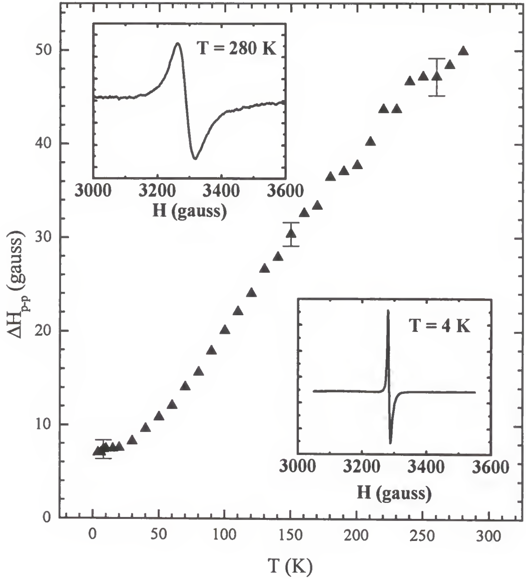

Figure 4-10. Plot of the EPR linewidth ($\Delta H_{p\text{-}p}$) as a function of temperature for **14**. The linewidth decreases relatively linearly with decrease in temperature which is characteristic of metallic species.

inorganic materials is attributed to the low-dimensionality present in the organic materials reducing the spin-orbit coupling.

The decrease in linewidth as the temperature is lowered in **14** is a common feature of organic metals due to reduced conduction-electron scattering.[119-123] Conduction electron scattering is greatest when the spin-lattice vibrations are greatest, which normally occurs at high temperatures due to the thermal vibrations of the lattice. As the temperature is lowered thermal lattice vibrations decrease reducing spin-lattice interactions resulting in longer spin-relaxation times, T_2, which result in narrower linewidths.

The integrated area of the EPR signal for a single crystal of **14** was measured from 4 to 298 K with the static magnetic field approximately perpendicular to the crystallographic *ab* plane (i.e. the crystal face). The temperature dependence of the integrated area is plotted in Figure 4-11. All EPR spectra have been fit to a linear combination of Lorentzian absorption and dispersion assuming a flat-plate geometry using the methods outlined by Chapman *et al* . for magnetic resonance in metallic species.[118] The integrated area at each temperature was obtained from the absorption portion of the measured signal and subsequently corrected for the reduced microwave penetration depth of the sample. This phenomenon is a consequence of the reduced skin depth due to the increasing conductivity of the sample as the temperature is lowered. The integrated area plotted in Figure 4-11 is approximately temperature independent down to ~60 K where a strong upturn occurs. The relatively constant integrated area between room temperature and 60 K is consistent with Pauli paramagnetism observed in metallic species. The integrated area data below 8 K can be fit to a Curie law, however the upturn between 60 K and 8 K is not Curie-like. In this temperature regime the increase in the integrated area may be a signature of localization of the conduction electrons. Localization of electrons implies that each electron behaves singularly; that is, each spin does not see its neighboring spins, therefore the spins behave as individual paramagnetic centers. It remains unclear if the Curie-like behavior below 8 K is associated with the electron localization phenomenon or is a consequence of

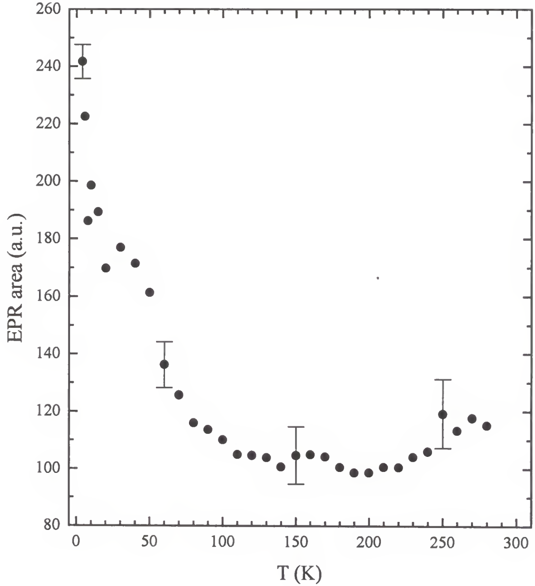

Figure 4-11. Plot of the integrated area of the EPR signal as a function of temperature for compound **14**.

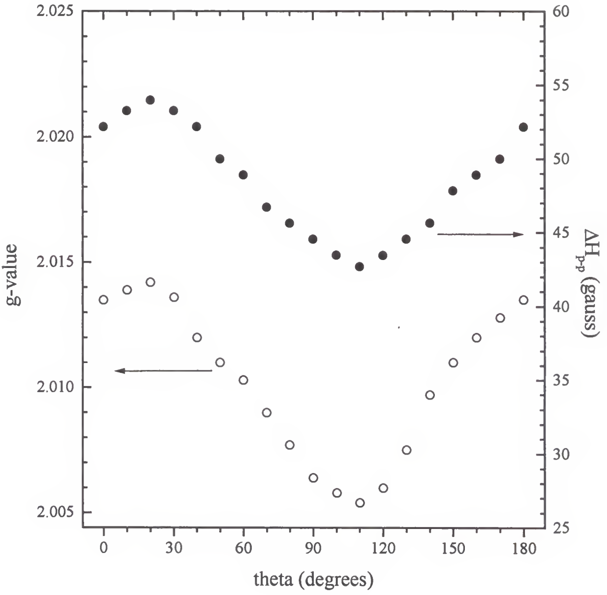

Figure 4-12. Angular dependence of the g-value and linewidth, ΔH_{p-p}, for **14** at 298 K from the EPR experiment with the static magnetic field perpendicular to the *ab* plane.

paramagnetic impurities beginning to dominate the signal at low temperatures. We believe the answer is a combination of both effects. Impurities in the crystal will make a Curie-like contribution to the integrated area, while both impurities and defects in the crystal provide the environment needed for Anderson-type localization to occur. In either case, we expect the EPR integrated area to increase as we have observed.

The g-value for **14** is nearly independent of temperature, increasing slightly from 2.011(3) at room temperature to 2.014(3) at 4 K. The angular dependence of the g-value and linewidth were studied at room temperature on a single crystal with the conducting *ab* plane (i.e. the crystal face) both perpendicular and parallel to the static magnetic field. The rotational dependence of both the linewidth, $\Delta H_{p\text{-}p}$, and g-value at 298 K are plotted in Figure 4-12 for the crystal oriented perpendicular to the static magnetic field. In this plot 0° corresponds to the crystal face (*ab* plane) perpendicular to the static magnetic field while 90° corresponds to the crystal face parallel to the static magnetic field. Anisotropy in the g-value arises from coupling of the spin angular momentum with the orbital angular momentum. For both the linewidth and g-value, one maximum and one minimum are seen near 20° and 110°, respectively, which are slightly shifted from the crystallographic axes. A consequence of the low crystal symmetry (i.e. space group $P\bar{1}$) is that the principal molecular axes of the BEDO-TTF molecules do not correspond with any of the crystallographic axes. Based on the crystal structure, the long axis of the BEDO-TTF cation forms angles of 90°, 81.1°, and 20.5° with the *a*, *b*, and *c* axes, respectively. The g-value maximum of 2.014 (1) at 20° corresponds to the static magnetic field approximately parallel to the long molecular axis (i.e. central C=C double bond) while the minimum g-value of 2.005(1) at 110° corresponds to the static magnetic field approximately parallel to the BEDO-TTF short molecular axis of the BEDO-TTF molecule.[124] The crystal was also mounted horizontally in the cavity with the crystal face (*ab* plane) parallel to the static magnetic field and angular dependent g-values were measured and are plotted in Figure 4-13. All spectra recorded with the crystal mounted horizontally, that is, with the static magnetic field parallel to the crystal face, were Dysonian in nature. This is a result of the highly conducting *ab* plane lying perpendicular to the oscillating microwave magnetic field which causes more reflection of the microwave radiation than absorption. In this plot one maximum g-value of 2.0026(1) and one minimum g-value of 1.9985(3) exist at 30° and 120°, respectively. The maximum g-value in Figure 4-13 corresponds to the static magnetic field parallel to the BEDO-TTF short molecular axis, and the minimum g-value corresponds to the static magnetic field perpendicular to the BEDO-TTF molecular plane. The principal g-values and the axes of the g-tensor were determined by performing a least squares fitting of the data in both orientations (i.e. perpendicular and parallel to the crystal face) to

$$g^2 = \sum_{i,j=1}^{n} g_{ij}^2 I_i I_j , \qquad (4\text{-}4)$$

where I_i and I_j are the direction cosines of the principal axes (x, y, and z).[125] The g-values calculated are shown by solid lines in Figure 4-13 and 4-14 for the crystal face (i.e. the *ab* plane) parallel and perpendicular to the static magnetic field, respectively. The principal g-values are $g_{(xx)} = 2.004(1)$, $g_{(yy)} = 1.9985(3)$, $g_{(zz)} = 2.014(1)$, which correspond to the static field parallel to the BEDO-TTF short molecular axis, perpendicular to the molecular plane, and parallel to the long molecular axis, respectively. This result suggests that the g-values of this BEDO-TTF based salt are determined by the g tensor of the BEDO-TTF radical cation.

Magnetic Susceptibility Results for $(BEDO\text{-}TTF)_4[C_4N_6]\cdot H_2O$ (**14**).

Static susceptibility, χ(T), measurements performed using a SQUID magnetometer were recorded from 5 K to 300 K. The data for a 4.5 mg sample of **14** are plotted in Figure 4-15 with the EPR integrated area data shown in the inset. Qualitatively, the results of the magnetic susceptibility are consistent with the EPR integrated area data, showing

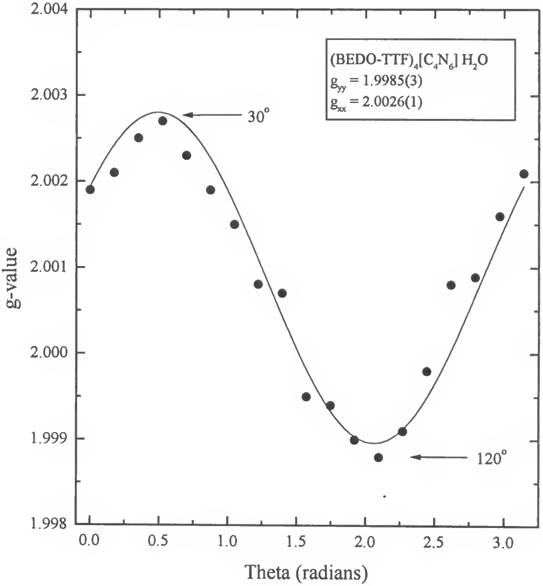

Figure 4-13. The angular dependence of the g-value for a single crystal of **14** with the *ab* plane (i.e. crystal face) parallel to the static magnetic field and perpendicular to the microwave magnetic field. The solid line shows the best fit of the data to Equation 4-4.

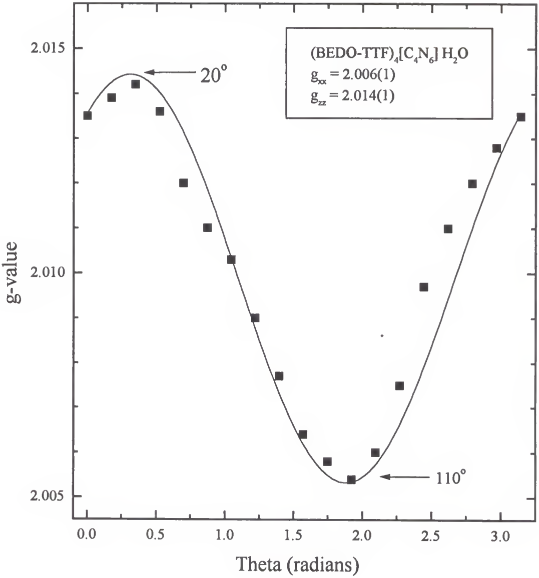

Figure 4-14. The angular dependence of the g-value for a single crystal of **14** with the *ab* plane (i.e. crystal face) perpendicular to the static magnetic field and parallel to the microwave magnetic field. The solid line shows the best fit of the data to Equation 4-4.

nearly Pauli paramagnetism[1] at high temperatures with a room temperature susceptibility of 5.0 (± 1) x 10^{-4} emu/mol. The temperature independent paramagnetism observed in **14** is consistent with metallic behavior.

At temperatures below approximately 60-70 K, the susceptibility increases steadily down to 5 K. The increase in susceptibility is indicative of electrons in localized states behaving as individual paramagnetic centers. The actual metal-to-insulator transition temperature is difficult to discern from the $\chi(T)$ because the mass of sample used was extremely small. The low mass sample had approximately the same signal intensity as the gel cap and straw which the sample was held, making extraction of features from the data difficult. The same signatures present in the EPR data are also found in the susceptibility data, but no real quantification of the onset of the metal-to-insulator transition can be determined. Future magnetometry work could be done on larger mass sample which should help to highlight features of the metal-to-insulator transition at temperatures below 70 K.

Nature of the Metal-to-Insulator Transition in (BEDO-TTF)$_4$[C_4N_6]·H_2O (14).

In at least one other BEDO-TTF salt, (BEDO-TTF)$_2$ReO$_4$·H_2O, a low T metal-to-insulator transition has been attributed to a spin density wave (SDW) ground state.[114] The preliminary characterization of **14** suggests that a SDW state is not reasonable for the metal-to-insulator transition seen here, but rather due to possibly Mott-Hubbard type or Anderson type localization of the conduction electrons below 60 K. Despite EPR evidence for conduction electron localization in **14** at temperatures below 60 K, the transport data show that **14** remains metallic down to 8 K where electron localization effects dominate both the magnetic and electrical properties observed.

The SDW state is not a valid phenomenon for the metal-to-insulator transition in **14** for several reasons. First, the magnetic susceptibility data at T < 8 K do not indicate an antiferromagnetic state which would be expected due to the spin-spin interactions associated with the SDW state. Second, the EPR integrated area data, linewidth data, and

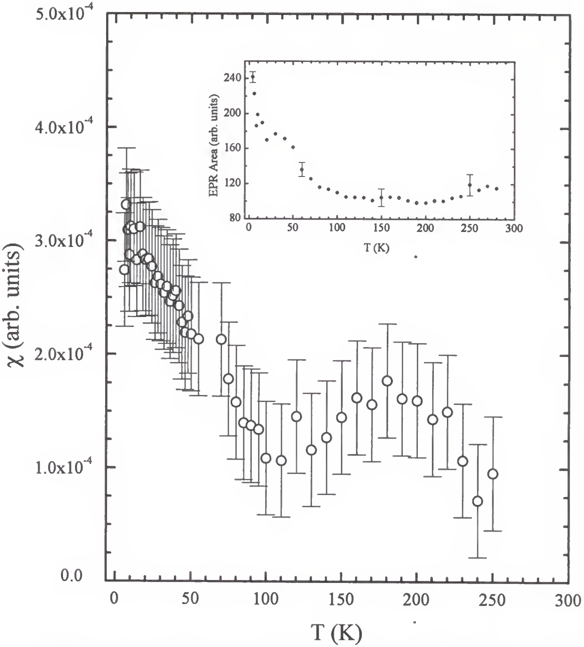

Figure 4-15. The magnetic susceptibility as a function of temperature for a 4.5 mg sample of randomly oriented crystals of **14**. χ(T) is approximately temperature independent between 298 K and 70 K indicative of Pauli independent paramagnetism seen in metals, while the increase in susceptibility below 70 K is consistent with gradual localization of the conduction electrons.

g-value data as a function of temperature are inconsistent with an SDW state. Previous work on (BEDT-TTF)$_2$KHg(SCN)$_4$ and (BEDT-TTF)$_2$RbHg(SCN)$_4$ reported by Kinoshita *et al.*[121,123] shows evidence for an SDW state in these materials based on correlations between EPR and conductivity data. The two BEDT-TTF salts have a metal-to-insulator transition around 8 - 10 K evident in the conductivity data. Detailed EPR studies on the two salts show anomalous behavior at temperatures below 20 K. In both salts marked changes in the EPR integrated area and g-value occur below 20 K. In (BEDT-TTF)$_2$KHg(SCN)$_4$ a decrease in both the EPR integrated area and g-value occur as the temperature is decreased below 20 K, while there is a slight increase in the EPR linewidth.[121] These signatures along with the metal-to-insulator transition in the transport data confirm the existence of an SDW state in (BEDT-TTF)$_2$KHg(SCN)$_4$. (BEDT-TTF)$_2$RbHg(SCN)$_4$ exhibits similar transport and EPR behavior with the EPR integrated area decreasing below 20 K, EPR linewidth increasing slightly, and the g-value increasing below 20 K.[123] The difference in the g-value behavior (i.e. the potassium salt decreasing and the rubidium increasing) below 20 K is due to different crystal alignments in the EPR cavity. Also the existence of an SDW state in (BEDT-TTF)$_2$KHg(SCN)$_4$ was further confirmed by high-field magnetoresistance data collected by Oshima *et al.*[122]

In **14** the EPR linewidth, area, and g-value data exhibit none of the characteristic features observed in the EPR data for (BEDT-TTF)$_2$KHg(SCN)$_4$ and (BEDT-TTF)$_2$RbHg(SCN)$_4$. The integrated area of the EPR signal has a Curie-like increase at low temperatures rather than a spin pairing decrease, while the peak-to-peak linewidth decreases linearly down to the lowest temperatures with no deviation. Also, no significant change in the g-value occurs at low temperatures, therefore, an SDW transition in **14** is not supported by the EPR data.

One other possibility which has been considered is a structural disorder in either the cationic or anionic sublattice. It has been suggested[114] that this type of transition is highly unlikely because ordered phases commonly exist at low temperatures. The transport and

EPR data confirm that (BEDO-TTF)$_4$[C$_4$N$_6$]·H$_2$O is metallic down to low temperatures, followed by a metal-to-insulator transition which is a result of conduction electron localization in the lattice.

Based on our EPR and magnetic susceptibility results, an SDW magnetic phase transition is not the likely cause of the 8 K metal-to-insulator transition. We believe that insulating state present in **14** is due to localization of the conduction electrons. There are many reports of Mott-Hubbard metal-to-insulator transitions in BEDT-TTF based salts. Recall that this type of transition results in antiferromagnetic array of spins in the ground state. Our EPR and magnetic susceptibility data do not support a transition to an antiferromagnetic state. However, the previously mentioned Anderson type localization is a plausible explanation for the metal-to-insulator transition observed in **14**. The Anderson type localization results from impurities and defects in the crystal lattice and has no magnetic phase transition associated with it. The electron scattering due to defects and impurities costs more energy than if the electrons localize themselves. In salt **14** we believe that Anderson type localization occurs which results in localized spins with paramagnetic behavior. This type of behavior is supported by the increasing EPR integrated area and the increasing magnetic susceptibility at temperatures in the vicinity of the 8 K metal-to-insulator transition.

4-4 Summary

A new metallic BEDO-TTF cation-radical salt with a cyano-rich anion, N,N',N"-tricyanoguanidinate, (BEDO-TTF)$_4$[C$_4$N$_6$]·H$_2$O, has been synthesized and characterized, and represents a new material which may be added to the growing list of BEDO-TTF based organic metals. This cation-radical salt incorporating the N,N',N"-tricyanoguanidinate dianion adopts the "I$_3$" packing motif found in other BEDO-TTF cation-radical salts. The BEDO-TTF donor molecule network consists of two-dimensional arrays separated by infinite sheets of N,N',N"-tricyanoguanidinate dianions which form dimers through hydrogen bonding with water molecules. Numerous S···S, S···O, and C-H···O interactions are present between BEDO-TTF cations within one stack as well as between adjacent stacks of cations. Inner fulvalene ring S···S close contacts which exist readily in BEDO-TTF salts unlike in BEDT-TTF salts enhance the π overlap between donor molecules stabilizing the metallic state to low temperatures. The 4:1 stoichiometry found in **14** gives each BEDO-TTF cation a charge of +1/2. This 4:1 cation-to-anion ratio has been seen in the other BEDO-TTF salts with cyano-based dianions.

The title compound is metallic with a room temperature conductivity of 11.5 S cm^{-1} and has $\sigma_{\max}$ of 38.5 S cm^{-1} at 8 K. Below 8.5 (± 1) K **14** undergoes a metal-to-insulator transition due to conduction electron localization. The nature of the metal-to-insulator transition (i.e. Mott-Hubbard or Anderson) cannot be determined from the resistance data. The tunnel diode oscillator (TDO) experiment shows an increase in the resonant frequency of the circuit at approximately 8.5 (± 1) K indicative of an increase in the skin depth of **14** due to the metal-to-insulator transition. The resistivity was probed down to millikelvin temperatures, but no indication of a superconducting transition was observed. The magnetic susceptibility between 298 K and 70 K and the EPR integrated between 298 K and 60 K are characteristic of temperature independent Pauli paramagnetism observed in metallic species at high temperatures, while below ~60 K the behavior is consistent with the gradual localization of the conduction electrons. In addition, the EPR data show no evidence of a low temperature magnetic phase transition to an SDW state as observed in some cation-radical salts of BEDT-TTF and BEDO-TTF.

CHAPTER 5

A NEW SALT OF THE ORGANIC DONOR BEDT-TTF INCORPORATING A HEXACYANOMETALLATE ANION, β"-$(BEDT\text{-}TTF)_4[Fe(CN)_6]\cdot 2CH_2Cl_2$

5-1 Introduction

Molecular conducting, superconducting and magnetic materials of low dimensionality have been of great interest in recent years, especially interest in materials which exhibit cooperative magnetic and conducting or superconducting properties.[126] Day and co-workers[44] in 1995 synthesized the first organic molecular superconductor which incorporated an inorganic magnetic counterion in the lattice, namely, $(BEDT\text{-}TTF)_4[(H_2O)Fe(C_2O_4)_3]\cdot C_6H_5CN$ with a superconducting transition temperature of 8.5 K, while more recently Kobayashi *et al.*[127] observed superconductivity ($T_c = 4.6$ K) in $(BEDT\text{-}TTF)_2(FeCl_4)_{0.5}(GaCl_4)_{0.5}$. Interesting physical properties could exist in the organic cation-radical layer of the lattice resulting from the interactions of the donor layers with the inorganic magnetic anion network.

In the quest to synthesize novel organic conductors based on BEDT-TTF and BEDO-TTF, we attempted to grow materials incorporating inorganic hexacyanometallate anions in the lattice. There are a few reasons for incorporating such anions into the lattice. Remembering that the conducting nature of these organic cation-radical salts stems from the overlap of the extended π-orbital network in the organic layers, we wished to improve the orbital interactions between donor cations in the layers. One way to achieve this is to incorporate highly charged anions into the lattice. The high negative electronic charges must be compensated by large degree of positive charge in the cation layer. The need for high positive charge density could in fact increase the interactions between donor cations, thereby increasing π-orbital overlap within the donor layers. Second, the cyano-based ligands are known for their ability to form "polymeric" anion networks via N···M or N···H-O-H bridges. We have seen this in the previous chapter where the salt (BEDO-TTF)$_4$[C$_4$N$_6$]·H$_2$O incorporates the tricyanoguanidinate dianion, containing three terminal cyano groups. The anion layer is made of an infinite ribbon-like sheet of tricyanoguanidinate anions which form dimers via hydrogen bonding with water molecules. Third, the incorporation of a highly charged anion could allow for non-integer high-oxidation states (i.e. between +1 and +2) of the organic donor cation not seen before. For example, instead of a large number of low-oxidation state donor cations merging together in the donor layer, the possibility of fewer high-oxidation state donors cations in the layer is conceivable. This kind of behavior would result in materials with degrees of band filling different than those presently known.

Recently, several new materials, κ-(BEDT-TTF)$_4$(H$_5$C$_2$)$_4$N[M(CN)$_6$]·3H$_2$O and β-(BEDT-TTF)$_5$[M(CN)$_6$]·10H$_2$O (where M = Co(III), Cr(III), and Fe(III))have been synthesized and characterized.[128,129] In the hexacyanocobaltate salt the metal is diamagnetic while in the ferricyanide salt the metal is paramagnetic making this salt the first example of a BEDT-TTF material incorporating an octahedral magnetic counterion. In the κ-phase materials[128] the counterion network consists of hexacyanometallate anions, tetraalkylammonium cations, and water solvent molecules giving an overall charge of -2 in the anion layer. Each BEDT-TTF donor cation has a +1/2 charge and the cations form dimers which pack orthogonal to one another, hence the κ-type packing designation. In each of the κ-phase materials the donor:anion ratio is 4:1 with each BEDT-TTF having a +1/2 charge, which is quite normal for BEDT-TTF cation-radical salts. In this case a large number of donor cations is needed to for charge compensation. The β-phase materials[126] also incorporate hexacyanometallate trianions with alternating layers of BEDT-TTF cations and M(CN)$_6^{-3}$ anions. These materials are interesting due to the nature of the anion included.

Using electrocrystallization techniques we have isolated a new BEDT-TTF cation-radical salt, β"-(BEDT-TTF)$_4$[Fe(CN)$_6$]·2CH$_2$Cl$_2$ **(15)**, which incorporates the ferricyanide (i.e. Fe(CN)$_6^{-3}$) anion and methylene chloride solvent molecules in the anion network. Our material is the first BEDT-TTF cation-radical salt to incorporate a trivalent hexacyanometallate anion without other alkali metal or tetraalkylammonium cations compensating charge. Also, **15** is the first BEDT-TTF salt, containing BEDT-TTF donor cations with +0.75 oxidation states to adopt the β" packing motif.[130-132] Unlike the salts described above, our salt does not contain any cations in the anion layer which lower the overall negative charge. Like the other two hexacyanometallate salts described above, **15** has a 4:1 donor:anion ratio, but our salt contains three charges delocalized over 4 BEDT-TTF molecules. We achieve both the inclusion of a high-valent anion (-3) as well as non-integer oxidation state (+0.75) donor cations in our material. The transport data show **15** to be a robust semiconductor at room temperature with a conductivity of 0.35 Ω^{-1}cm^{-1}. The plot of ln R versus 1/T does not generate a single linear relationship. The X-band electron paramagnetic resonance (EPR) data reveal that the EPR resonance signal linewidth remains constant until 150 K where the linewidth begins to broaden rapidly likely due to anisotropic exchange or dipolar coupling, while the EPR integrated area exhibit a broad maximum at about 240 K followed by decrease to a minimum at 150 K below which the area increases rapidly. Below 70 K, both the linewidth and integrated area data for **15** are dominated by the signal due to the Fe(III) ions in the lattice. High-Field EPR measurements were performed at the National High Magnetic Field Laboratory in Tallahassee, FL in order to resolve the two signals observed at temperatures below 70 K in the X-band measurements. The signal from the BEDT-TTF cation-radical and the Fe(III) signal were resolved. The magnetic susceptibility data are also dominated by the Fe(III) signal, and attempts have been made to subtract this contribution from the data in order to observe the magnetic behavior of the BEDT-TTF spins.

5-2 Experimental Section

Materials. BEDT-TTF was synthesized by the method of Larsen and Lenoir.[89] Potassium ferrocyanide trihydrate ($K_4Fe(CN)_6{\cdot}3H_2O$) was purchased from Aldrich Chemical Co. (Milwaukee, WI) and was used without further purification. 1,4,7,10,13,16-hexaoxacyclooctadecane or 18-crown-6 ($C_{12}H_{24}O_6$, 98%) was purchased from Aldrich Chemical Co. (Milwaukee, WI). Methylene chloride (CH_2Cl_2, 99.9%) and ethanol (C_2H_5OH, absolute) were purchased from Fisher Scientific (Orlando, FL). Methylene chloride was dried over P_2O_5 and distilled before use, while ethanol and 18-crown-6 were used without further purification.

β-(BEDT-TTF)$_4$[Fe(CN)$_6$]$\cdot$2CH$_2$Cl$_2$ (15). BEDT-TTF (8.2 mg) was placed in the working arm of a two-electrode H-cell and dissolved in 35 mL of 3.52 mM potassium ferrocyanide in 15% CH_3CH_2OH/methylene chloride containing 150 mg of 18-crown-6. A constant current density of 0.25 $\mu A/cm^2$ was maintained at room temperature between the platinum working electrode and counter electrode that were separated by two glass frits. After a few days long needles of **15** could be seen on the electrode surface and at the bottom of the H-cell. Large black needles of **15** were collected after 25 days.

Crystallographic data collection and structure determination. Data were collected at 173 K on a Siemens SMART PLATFORM equipped with a CCD area detector and a graphite monochromator utilizing MoK_α radiation ($\lambda = 0.71073$ Å). Cell parameters were refined using up to 5684 reflections. A hemisphere of data (1381 frames) was collected using the ω-scan method (0.3° frame width). The first 50 frames were remeasured at the end of data collection to monitor instrument and crystal stability (maximum correction on I was < 1 %). Empirical absorption corrections were applied based on the entire data set.

The structure was solved by Direct Methods in *SHELXTL5*,[74] and refined using full-matrix least squares. The lattice contains BEDT-TTF$^{+3/4}$ and $Fe(CN)_6^{-3}$ in a 4:1 ratio and one CH_2Cl_2 molecule for every 2 BEDT-TTF cations. There are two BEDT-TTF cations, one CH_2Cl_2, and a half of an $Fe(CN)_6^{-3}$ anion in the asymmetric unit. The

$Fe(CN)_6^{-3}$ ions are located on a center of symmetry. The non-H atoms were treated anisotropically, whereas the hydrogen atoms were calculated in ideal positions and were riding on their respective carbon atoms. 414 parameters were refined in the final cycle of refinement using 4554 reflections with $I > 2\sigma(I)$ to yield R_1 4.19% and wR_2 of 8.84%, respectively. Refinement was done using F^2.

EPR measurements. EPR spectra of **15** were recorded between 4 and 298 K using a Bruker (Billerica, MA) ER-200D spectrometer modified with a digital signal channel and a digital field controller equipped with an Oxford Instruments (Witney, England) ITC 503 temperature controller and ESR 900 cryostat equipped with an AuFe/Ch thermocouple. A single crystal of **15** was mounted on the cut edge of a quartz rod and placed vertically in the microwave cavity with the *ab* plane perpendicular to the static magnetic field and parallel to the microwave field. The sample was also oriented horizontally on the edge of the quartz rod so that the *ab* plane of the crystal was parallel to the static magnetic field and perpendicular to the microwave field. Data were collected at 9.27 GHz with 100 kHz modulation using a U.S. EPR (Clarksville, MD) SPEX300 data acquisition program.

High-field EPR measurements. High-field EPR measurements were performed on powdered samples of **15** and spectra were acquired using the high-field EMR facility at the National High Magnetic Field Laboratory (NHMFL) in Tallahassee, Florida. The EPR spectrometer used two different types of millimeter and submillimeter wave radiation sources. Two Gunn oscillators were used (AB Millimetre, Paris) to access higher frequencies (95 - 380 GHz), one tunable over the range of 92 - 98 GHz and the other over the range of 108 - 112 GHz. In addition to operating at the fundamental frequencies, these Gunn sources were equipped with sets of Schottky-diode harmonic generators and filters which enabled operation at frequencies near 190, 285, and 380 GHz for the lower frequency oscillator, as well as 220 and 330 GHz for the higher frequency Gunn source. The frequency was measured by an EIP 578B counter which was also used as a frequency lock source for the Gunn oscillators. The Zeeman field was produced by an Oxford

Instruments Teslatron superconducting magnet capable of field sweeps from 0 - 17 T. The resonance absorption was measured at a fixed frequency by monitoring the transmitted power as a function of the applied magnetic field that is swept through the resonance with either an increasing or decreasing field. The field was modulated in the usual fashion with a frequency of 4 - 10 kHz, and phase detection was employed. A liquid helium cooled hot-electron InSb bolometer from QMC (London, England) was used as the power detector. EPR spectra were taken over the range of 5 - 80 K, each with the use of an Oxford Instruments CF-1200 continuous flow liquid helium cryostat.

SQUID magnetometry measurements. The temperature dependence of the magnetic susceptibility between 2 and 298 K was obtained from magnetization measurements made using a Quantum Design MPMS SQUID magnetometer on a 10.0 mg sample of randomly oriented single crystals of **15**. A #5 gel capsule and plastic straw were used as sample holder during the measurements. The background signals arising from the gel capsule and straw were measured independently and subtracted from the raw data.

Transport measurements. Temperature dependent (100 - 298 K) resistivity measurements were made using a four-probe technique. Four gold contacts (~3000 Å thick) in a linear arrangement were deposited on a single needle-like crystal ($2.5 \times 0.4 \times 0.3$ mm^3) of **15** by thermal evaporation, and narrow gauge (0.0127 mm diameter) gold wires were affixed to the contacts using fast-drying silver paint. The sample was fastened onto a chip-holder which attaches to our home-built low temperature dipstick. A typical run was done by first cooling the sample to the lowest temperature and collecting data while warming. Temperature stability obtained in this set-up has been determined to be ± 0.5 K or better over the temperature range measured.

5-3 Results and Discussion

Synthesis and Structure of β"-(BEDT-TTF)$_4$[Fe(CN)$_6$]·2CH$_2$Cl$_2$ (15).

Needle-like single crystals of **15** were obtained from electrochemical oxidation of BEDT-TTF in the presence of potassium ferrocyanide trihydrate, $K_4Fe(CN)_6 \cdot 3H_2O$, in a 6:1 mixture of methylene chloride:ethanol in an H-cell at a Pt working electrode at a fixed current density of 0.25 μA/cm^2. In order to increase the solubility of the ionic salt, $K_4Fe(CN)_6 \cdot 3H_2O$, in organic solvents, 18-crown-6 was added. After several days shiny, black needle-like crystals of **15** could be seen on the Pt electrode, and the crystals were harvested 25 days later. The crystals are stable in the open air for approximately 5 days after which time they begin to decompose, most likely due to loss of methylene chloride solvent molecules from the lattice.

β"-(BEDT-TTF)$_4$[Fe(CN)$_6$]·2CH$_2$Cl$_2$ crystallizes in the triclinic system $P\bar{1}$. The X-ray crystal structure was solved at 173 K and the crystallographic data are presented in Appendix Tables D-1 through D-5. Like many BEDT-TTF cation-radical salts, the X-ray structure of **15** consists of sheets of BEDT-TTF monocations separated by sheets of ferricyanide trianions. The anion and cation sheets are oriented parallel to the *ab* plane shown in Figure 5-1. There are two crystallographically independent BEDT-TTF monocations (A and B) in the donor layer evidenced by their differing central C=C bond distances which are 1.384(5) Å and 1.372(5) Å. As stated in previous chapters, donor ion bond lengths are often used to assign oxidation states in charge-transfer salts of BEDT-TTF. The bond lengths in our salt represent a new case. Plotted in Figure 5-2 are the oxidation states of known BEDT-TTF cations versus their central C=C bond distances. The plot suggests that our C=C bond distances lie between those associated with BEDT-TTF$^{+2/3}$ and BEDT-TTF^{+1} cations. We believe our salt contains BEDT-TTF cations with effective charges of +0.75 which coincide with the 4:1 stoichiometry present

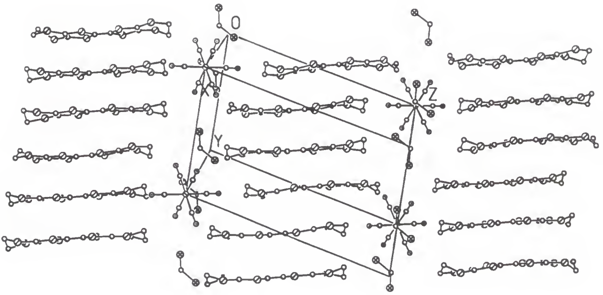

Figure 5-1. The packing diagram for **15** including both anions and cations. The BEDT-TTF molecules form 2D sheets which are separated by the layers of ferrocyanide anions and methylene chloride solvent molecules.

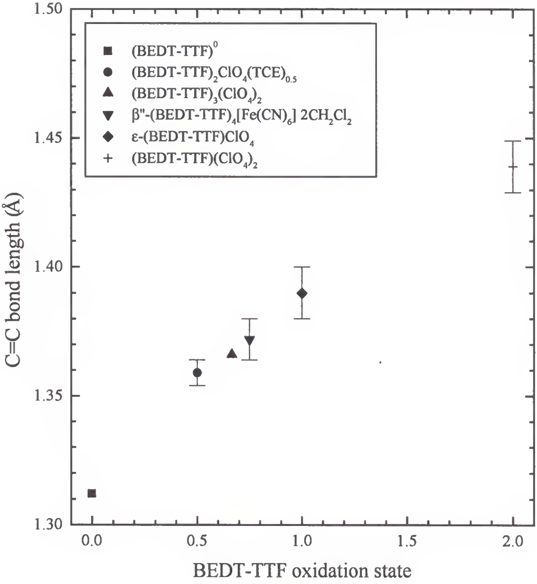

Figure 5-2. The BEDT-TTF central C=C bond distance (Å) versus BEDT-TTF cation oxidation state. The plot shows that our BEDT-TTF C=C bond distances of 1.372(5) and 1.384(5) lie between those of BEDT-TTF$^{+2/3}$ cations and BEDT-TTF^{+1} cations. We believe that our salt **15** contains BEDT-TTF$^{+3/4}$ cations formed with three charges or "holes" delocalized over 4 BEDT-TTF molecules. Data taken from references 45, 49, 50, 133, 134, and 135.

in **15**. In order to accommodate such a charge on the BEDT-TTF cations, three positive charges (holes) must delocalize over four molecules.

This type of charge delocalization is supported crystallographically. The two independent BEDT-TTF cations form columns and sheets of tetramers within the lattice structure. Figure 5-3 shows the BEDT-TTF tetramers along a column and within sheet of donor molecules. Recall that two types of BEDT-TTF molecules exist in **15**. Each tetramer consists of an ABBA arrangement of molecules where A and B represent the two independent BEDT-TTF molecules. Within each tetramer three charges are delocalized over four molecules resulting in a net charge of +0.75 on each BEDT-TTF molecule. Repeating units made up of 2, 3, 4, and 5 BEDT-TTF molecules are precedented in the literature.[44,126,128,132] The tetramerization of the BEDT-TTF molecules is important to the interpretation of the magnetic data (*vide infra*).

Slightly shifted from the *b* axis BEDT-TTF molecules stack face-to-face to form columns. Each BEDT-TTF$^{+3/4}$ cation has six nearest neighbors; two above and two below the molecular plane, as well as two neighbors on either side in the same plane shown in Figure 5-4 looking down the long axis of the BEDT-TTF molecules. The overlap is poor between molecules within a column, but there are several side-by-side intermolecular contacts between outer ring and inner ring sulfur atoms on adjacent molecules along the *a* axis, as well as S···S contacts with molecules along the *b* axis in adjacent columns forming a two-dimensional sheet of donors. The arrangement of BEDT-TTF donor molecules in **15** is consistent with the β"-phase[130-132] observed in BEDT-TTF cation-radical salts. The signature of the β"-phase[132] is an angle, θ, made between a BEDT-TTF stack and a BEDT-TTF sheet (seen in Figure 5-4) approximately equal to 60°, and in compound **15**, $\theta = 58.7°$. All of the previously synthesized β"-phase BEDT-TTF salts contain BEDT-TTF cations with a +1/2 oxidation state and are metallic,[130-132] making **15** the first β"-phase BEDT-TTF salt to contain +3/4 donor cations and behave electrically as a semiconductor.

The BEDT-TTF donor molecules are close-packed in order to compensate the large negative charges of the ferricyanide ($Fe(CN)_6^{-3}$) anions. The $Fe(CN)_6^{-3}$ anions and the methylene chloride molecules form columns which separate the BEDT-TTF donor sheets as illustrated in Figure 5-5. The two axially positioned cyano groups of the ferricyanide anions have two close contacts with methylene hydrogen atoms from two different CH_2Cl_2 molecules. Also, the terminal nitrogen atoms of the cyano groups as well as the chlorine atoms of the methylene chloride solvent molecules form close contacts with the hydrogen atoms of the terminal ethylene groups and the outer ring sulfur atoms of the BEDT-TTF molecules.

The structure of **15** is similar to the β-$(BEDT\text{-}TTF)_5[M(CN)_6]\cdot 10H_2O$ (M = Co(III), Cr(III), and Fe(III))[126] salts and differs significantly from κ-$(BEDT\text{-}TTF)_4(H_5C_2)_4N\ [Co(CN)_6]\cdot 3H_2O$ and κ-$(BEDT\text{-}TTF)_4(H_5C_2)_4N\ [Fe(CN)_6]\cdot 3H_2O$.[128,129] The β-phase salts have a 5:1 cation:anion stoichiometry with ten water molecules residing in the anion layer, giving each BEDT-TTF cation an effective charge of +0.6. The κ-phase salts consists of sheets of $(BEDT\text{-}TTF^{+1/2})_2$ dimers that pack orthogonal to one another. The κ-phase materials contain hexacyanometallate trianions, tetraethylammonium (TEA) cations, and water molecules in the counterion sheets. Rather than a forming with 6:1 stoichiometry (i.e. six $BEDT\text{-}TTF^{+1/2}$ cations to one trianion) or a 3:1 (i.e. 3 BEDT-TTF monocations to one trianion), the materials incorporate TEA cations to give an overall negative charge of -2. This allows for $BEDT\text{-}TTF^{+1/2}$ cations to form dimers. Our β''-phase salt **15** forms with a 4:1 donor:anion stoichiometry and does not incorporate other cations to compensate charge. This results in an effective charge of +0.75 per BEDT-TTF molecule.

Transport Properties of $(BEDT\text{-}TTF)_4[Fe(CN)_6]\cdot 2CH_2Cl_2$ **(15)**.

The organic donor BEDT-TTF forms cation-radical salts exhibiting a variety of conducting properties from superconductors with transition temperatures as high as $T_c = 12.8$ K to weak semiconductors with conductivities on the order of $10^{-6}\ \Omega^{-1}cm^{-1}$.[4]

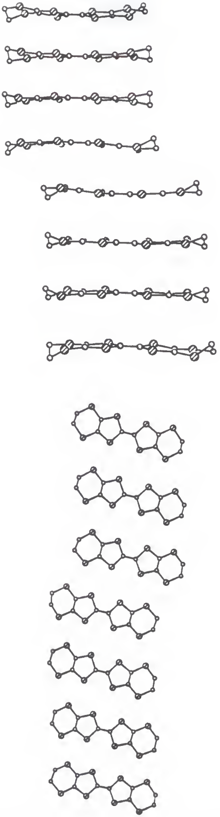

Figure 5-3. A view of the BEDT-TTF molecules showing the tetramerization of the molecules both along a stack and within a sheet. The two independent BEDT-TTF molecules, A and B, form "ABBA" tetramers. Each tetramer unit is shifted from the previous one in a column or in a sheet.

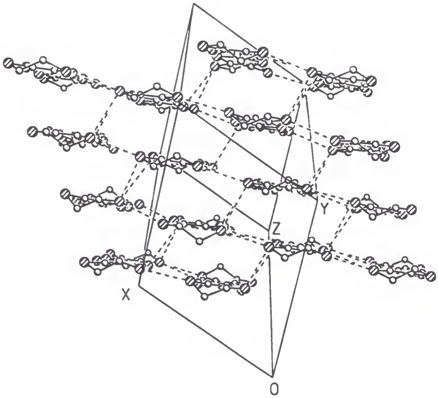

Figure 5-4. The BEDT-TTF cation layer present in **15**. The BEDT-TTF molecules within a stack are slightly displaced relative to one another such that the stacking axis forms an angle of 58.7° with the plane of the BEDT-TTF molecules. Each BEDT-TTF molecule has six nearest neighbors.

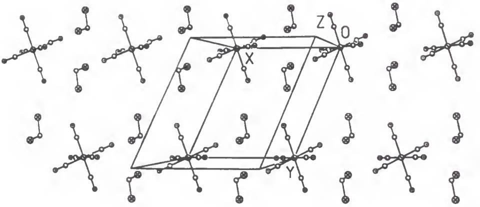

Figure 5-5. The ferricyanide trianion layer in **15** including methylene chloride (CH_2Cl_2) solvent molecules. Each ferricyanide trianion has two CH_2Cl_2 molecules associated with it forming an infinite sheet of ferricyanide trianions.

The requirement for highly conducting materials is partially empty conduction band which is a consequence of partial oxidation of the donor molecules. In salt **15** the BEDT-TTF tetramers have three charges delocalized over four molecules resulting in a non-integer of +0.75 per donor molecule. A valence band consisting of non-integer oxidation state BEDT-TTF cations provides the partially filled band needed for metallic conduction.

Resistance data collected for **15** using a four-probe technique are shown in Figure 5-6. The data show that **15** is a narrow band gap semiconductor with a room temperature resistance of 71 Ω, and a conductivity $\sigma_{298\,\mathrm{K}} = 0.35\ \Omega^{-1}\mathrm{cm}^{-1}$. The typical temperature dependent resistance of a semiconductor[1] can be expressed as

$$R = R_o e^{-E_g/2k_BT} \tag{5-1}$$

where R_o is a temperature independent resistance term, E_g is the energy of the semiconductor gap, k_B is Boltzmann's constant, and T is the temperature. Figure 5-7 plots the resistance data for **15** as the log R versus 1/T. The plot shows that the resistance does not obey a singular linear relationship. The slope of the line gives the activation energy E_g. Our data show three different regions of linear behavior, each with differing activation energies determined by fitting the data to equation 5-1. Figure 5-7 points out the three regions: region 1, 156 K to 214 K; region 2, 127 K to 156 K; region 3, 100 K to 127 K. The activation energy is not constant in any of the three regions, ranging from 0.17 eV at 214 K to 0.14 eV at 100 K. The mechanism of activated conduction is not clear though. Presumably the partially filled valence band is split forming filled bands due to localization of electrons on the tetramers. A room temperature X-ray structure might reveal the presence of equivalent BEDT-TTF molecules, which undergo a lattice distortion as the temperature is lowered resulting in two independent BEDT-TTF molecules which pack as tetramers (present in the 173 K structure). This form of lattice distortion would perhaps result in band splitting producing a semiconducting state.

EPR Properties of $(BEDT\text{-}TTF)_4[Fe(CN)_6]\cdot 2CH_2Cl_2$ (15).

The temperature dependent X-band EPR data were obtained with a single needle-like crystal of **15** oriented with the crystal face (*ac* plane) parallel to the microwave field and perpendicular to the static magnetic field. Representative EPR spectra at 280 K, 150 K, 90 K, 60 K, 30 K, and 4 K are illustrated in Figure 5-8. Above $T = 60$ K the EPR resonance is purely Lorentzian, while below 60 K an Fe(III) signal is present and increases in intensity down to 4 K. Figure 5-9 plots the peak-to-peak linewidth, $\Delta H_{p\text{-}p}$, as a function of temperature for **15** from 298 K to 70 K. The linewidth at room temperature is 58.7 G and $\Delta H_{p\text{-}p}$ remains constant down to 170 K. Below 170 K the linewidth increases monotonically to 130 G at 95 K while the increase is rapid below 95 K. Starting at 60 K an Fe(III) peak downfield from the BEDT-TTF signal begins to grow in making it difficult to determine the linewidth and calculate the integrated area of the BEDT-TTF resonance line.

The EPR linewidth data for **15** are temperature independent from room temperature down to 160 K indicating that the magnetic interactions are not influenced by magnetic exchange or magnetic dipole-dipole interactions.[7] The BEDT-TTF $S = 1/2$ spins are behaving as individual paramagnetic centers at high temperatures. However, below 160 K the linewidth increases as the temperature is continually lowered. The two types of interactions mentioned above (magnetic exchange or magnetic dipole-dipole interactions) have opposite effects on the EPR linewidth. Magnetic exchange interactions result in linewidth narrowing, while magnetic dipole-dipole interactions result in linewidth broadening. In compound **15** the linewidth broadens as the temperature is lowered indicative of dipole-dipole interactions. Any type of interaction of the magnetic ion and its surroundings may broaden the line if it results in energy being transferred from the ion following excitation. With many magnetic neighbors in the lattice a magnetic dipole may set up local magnetic fields with its neighbors adding additional fields randomly which serves to vary the magnetic field from site to site causing linewidth broadening.[7] These

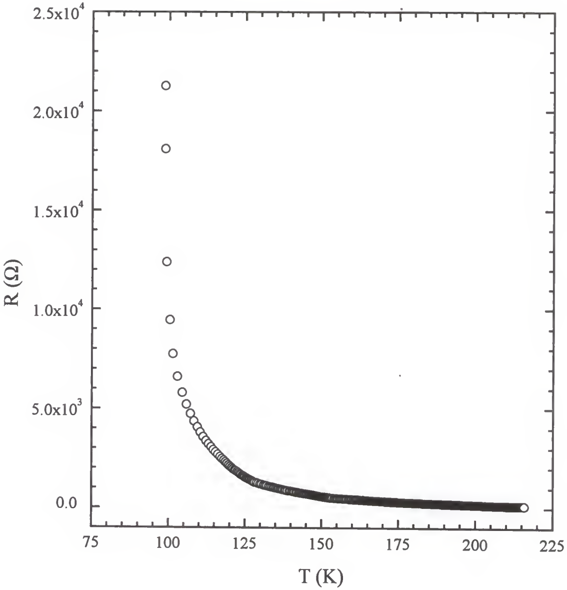

Figure 5-6. The temperature dependence of the resistance for **15** measured using a four-probe technique. The results show that as the temperature is lowered the resistance of **15** increases, indicative of semiconducting behavior.

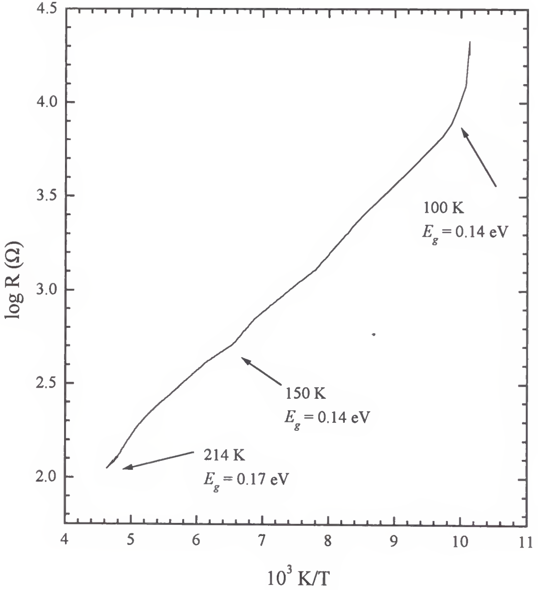

Figure 5-7. A plot of log R vs. (1/T) for **15** showing that the data do not obey a single linear relationship, but have three separate linear regions. The activation energy determined from the slope of the line in each region is not constant, but varies from 0.17 eV at 214 K to 0.14 eV at 100 K. The exact mechanism of activated conduction is not clear.

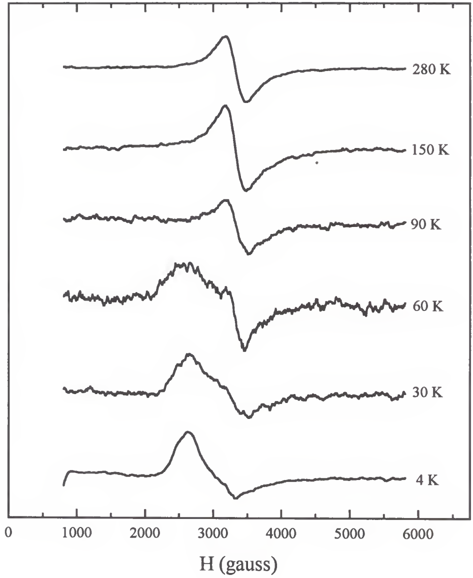

Figure 5-8. Representative X-band EPR spectra at 280 K, 150 K, 90 K, 60 K, 30 K, and 4 K for **15** with the crystal face oriented perpendicular to the static magnetic field. The BEDT-TTF resonance is purely Lorenztian at all temperatures, but at temperatures below ~ 70 K the BEDT-TTF signal is masked by the Fe(III) resonance which begins to grow in due to increased spin relaxation times.

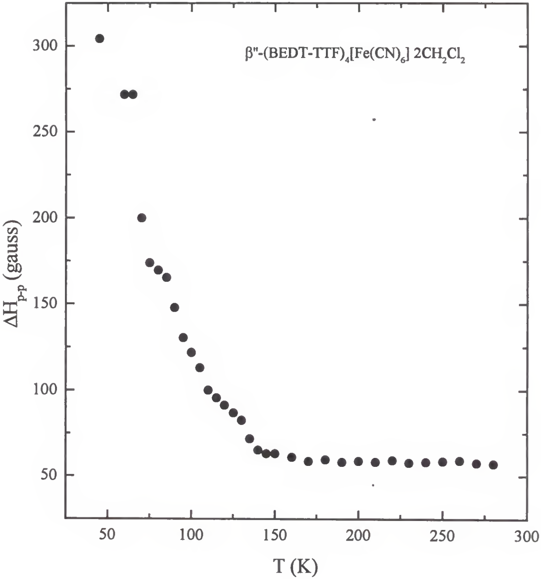

Figure 5-9. The linewidth, $\Delta H_{p\text{-}p}$, as a function of temperature for **15** from 298 K to 70 K. The linewidth remains constant down to approximately 170 K where it begins to increase rapidly down to 70 K. Below 70 K accurate determination of the linewidth of the BEDT-TTF resonance is not possible due to the Fe(III) signal.

effects appear to dominate the linewidth data below 160 K down to the lowest temperatures.

Plotted in Figure 5-10 are the integrated area data for **15** between 70 K and 298 K. The integrated area gradually increases as the temperature is lowered from room temperature and passes through a broad maximum at 240 K. Below 240 K the area followed decreases to a minimum at 145 K, below which the area increases rapidly. Again data below 70 K could not accurately be obtained due to the impurity signal. The EPR integrated area for **15** appears to highlight two transitions, one at 240 K and another at 150 K. The broad maximum at 240 K is normally associated with antiferromagnetic correlation (exchange) in the lattice, where nearest neighbor spins, S_i and S_j, align themselves antiparallel to one another. It can be speculated that the broad maximum observed in compound **15** at 240 K is a result of strong antiferromagnetic correlations, where nearest neighbor BEDT-TTF cations have their spins aligned antiparallel to one another. The marked decrease in the integrated area below 240 K is possibly due to spin pairing within the tetramer units, while the increase in the integrated area below 150 K is associated with a Curie-like contribution from the Fe(III) ions present in the anion sublattice.

Recall that below 70 K the signal due to the Fe(III) ions in the anion layer grows in as the temperature is lowered to 4 K. In order to investigate the nature of the signal high-field EPR experiments at the National High Magnetic Field Laboratory in Tallahassee, FL were undertaken to determine if the EPR signal due to the BEDT-TTF organic radical-cation still exists at low temperatures. The X-band EPR data show the apparent disappearance of the resonance from **15**, but more likely it is masked by the Fe(III) ion signal. The high-field EPR experiment allows for resolution of signals that have very similar g-values. The high-field EPR spectra of a powder sample of **15** taken between 80 K and 5 K are shown in Figure 5-11. The spectra show that at 80 K a single resonance line exists centered at g = 2.004(1), which corresponds to the intermediate g-value of **15**

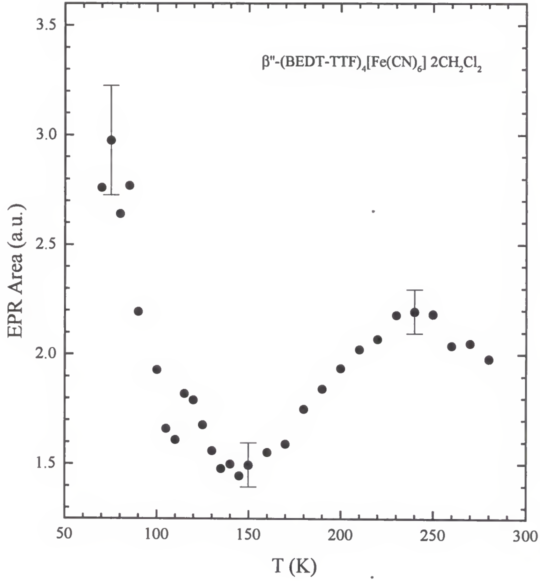

Figure 5-10. The EPR integrated area as a function of temperature for **15** from 298 K to 70 K. The integrated area goes through a broad maximum at 240 K followed by a decrease to a minimum at ~ 145 K. The area then increases rapidly down to the lowest temperatures most likely due to a Curie-like contribution from the Fe(III) ions in the anion layer. Below 70 K determination of the integrated area of the BEDT-TTF resonance was not possible due to the Fe(III) ion resonance.

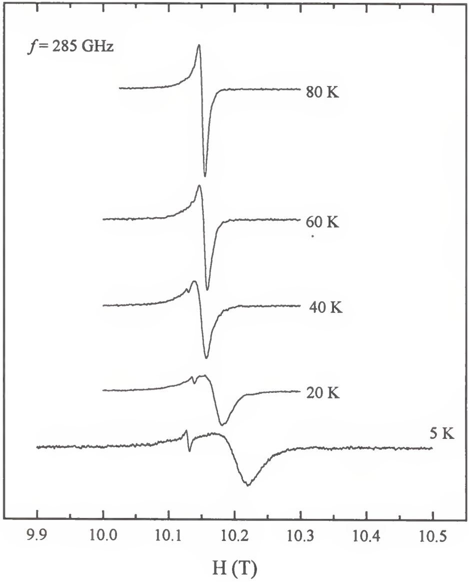

Figure 5-11. The high-field EPR spectra for **15** indicating that the Fe(III) signal grows in at around 60 K just as in the X-band EPR data. The high-field EPR experiment proves that the BEDT-TTF resonance is present at 5 K, and is masked in the X-band experiment.

determined through angular dependent X-band EPR experiments. This g-value is an average of all three principal g-values for compound **15** due to the powder-like nature of the specimen. The high-field EPR spectra show that the resonance due to the organic BEDT-TTF cations is still present at 5 K despite being masked by the Fe(III) signal in the X-band EPR experiment.

Magnetic Susceptibility Results on (BEDT-TTF)$_4$[Fe(CN)$_6$]$\cdot$2CH$_2$Cl$_2$ (15).

The results of the temperature dependent magnetic susceptibility on a polycrystalline sample of **15** are shown in Figure 5-12. The susceptibility behavior observed in **15** shows Curie paramagnetism. The data show no resemblance to the X-band EPR integrated area data taken on a single crystal of **15**. The data appear to be dominated by the Fe(III) ions from the anion sublattice. The low temperature susceptibility (2 - 20 K) data fit nicely to the Curie law, namely

$$\chi = \mathrm{C} / \mathrm{T} \tag{5-2}$$

with a Curie constant of C = 0.217 (± 1) emu-K/mol. The Curie fit can be used to determine the contribution of the Fe(III) ions in the sample by determining the number of Fe(III) spins using

$$\mathrm{C} = \frac{N\mu_B^2 g^2 S(S+1)}{3k_B} \tag{5-3}$$

where μ_B is the Bohr magneton, g is the g-value of the material, S is the effective spin of the material, and k_B is Boltzmann's constant. In Equation 5-3 N is the number of Fe(III) spins in the material. The number of spins/mol of Fe(III) in **15**, ($N_{Fe(III)}$), divided by Avogadro's number of spins in one mole, (N_A), will give the percentage of Fe(III) spins in the sample. The value of $N_{Fe(III)}$ was 3.49 x 10^{23} spins/mol, and this value divided by

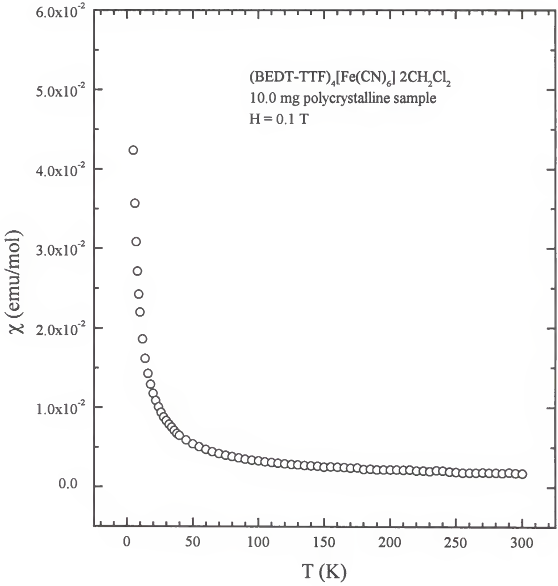

Figure 5-12. The magnetic susceptibility as a function of temperature for a 10.0 mg polycrystalline sample of **15**. The data exhibit Curie behavior at all temperatures indicating that the data are dominated by the signal due to the Fe(III) ions in the anion layer which effectively mask the BEDT-TTF radical-cation signal.

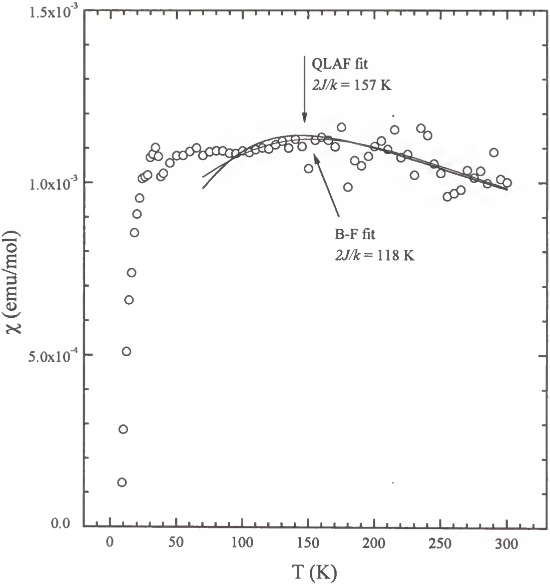

Figure 5-13. Bonner-Fisher (B-F) and Quadratic-layer-antiferromagnet (QLAF) fits to the magnetic susceptibility data for **15**. A Curie law fit to the low temperature data was subtracted leaving the signal due to the BEDT-TTF radical-cations.

Avogadro's number gave an Fe(III) spin percentage of 58%. This percentage implies that over half of the magnetic response is due to the Fe(III) magnetic centers in the crystal. If the contribution to the magnetic susceptibility from the Fe(III) ions is subtracted, the remaining signal belongs to the BEDT-TTF radical-cations. The subtraction of the Curie contribution of the Fe(III) ions, from the magnetic susceptibility data results in the curve plotted in Figure 5-13. The data shown in Figure 5-13 are due to the BEDT-TTF radical-cations and can be fit to both the one-dimensional Bonner-Fisher (B-F)[9] and two-dimensional Quadratic Layer-Antiferromagnet (QLAF)[101] models. The values for the magnetic exchange, *J/k*, are 118 (± 5) K and 157 (± 5) K for the B-F and QLAF models, respectively, and the fits are also shown in Figure 5-13. The broad maximums are centered at 118 K and 157 K for the B-F and QLAF models, respectively. The fits are quite similar making it difficult to discern whether the magnetic behavior of **15** is one-dimensional or two-dimensional, although, based on the two-dimensional nature of the BEDT-TTF cation lattice, the QLAF model is more appropriate. After the subtraction of the Fe(III) ion contribution, the data look similar to the EPR integrated area data with a broad maximum at high temperatures. The data suggest that there are antiferromagnetic correlations at high temperatures, and there possibly could be a singlet-to-triplet transition indicated by the sharp decrease in the susceptibility data.

The spin pairing could be mediated through the tetramers in the BEDT-TTF two-dimensional layers (i.e. within a BEDT-TTF sheet and not along a BEDT-TTF column). Recall that in **15** three spins are delocalized over four molecules, so two of the three spins could pair. This type of spin pairing mechanism could account for the 60% decrease in the EPR integrated area of **15** between 240 K and 150 K. The increase in the integrated area at lower temperatures is likely due to Fe(III) ion effects.

5-4 Summary

We have isolated a new BEDT-TTF cation-radical salt, β''-(BEDT-TTF)$_4$[Fe(CN)$_6$]·2CH$_2$Cl$_2$ (**15**), which incorporates the ferricyanide (i.e. Fe(CN)$_6^{-3}$) anion, and our material is the first β''-BEDT-TTF cation-radical salt to incorporate a trivalent hexacyanometallate anion as well as the first to contain BEDT-TTF$^{+3/4}$ cations. Historically the β'' phase has been reserved for (BEDT-TTF)$_2$X salts where each BEDT-TTF molecule has a +1/2 oxidation state. The BEDT-TTF cation layer consists of two independent BEDT-TTF molecules (A and B) which form tetramers in an ABBA arrangement. The transport data for **15** show the compound to be a narrow band gap semiconductor, with a room temperature conductivity of 0.35 Ω^{-1}cm^{-1}. The EPR integrated area show **15** to have strong antiferromagnetic correlations at high temperatures followed by a significant decrease in the integrated area, while the low temperature data are dominated by Fe(III) ions from the anion layer. The total magnetic susceptibility for **15** is Curie-like from 4 - 300 K due to the Fe(III) ions in the anion sublattice. The contribution of the Fe(III) spins was subtracted from the total susceptibility leaving the contribution from the BEDT-TTF radical-cations. The corrected susceptibility data suggest antiferromagnetic correlations within the two-dimensional BEDT-TTF cation layers.

The results reported on compound **15** are preliminary. It appears that the use of K$_4$(Fe(CN)$_6$)·H$_2$O as the starting electrolyte does not result in a material with Fe(II) ions, but rather the material formed contains the impurity Fe(III) ions present in the electrolyte. Future work should be performed in order to fully characterize the form of iron present in this system. In addition, magnetometry should be run again on other samples in order to obtain more definitive results on the magnetic properties of the BEDT-TTF cation network. A room temperature X-ray crystal structure would show if the BEDT-TTF cations are crystallographically different than at 173 K, the temperature of the X-ray structure presented in this chapter. It would be interesting to perform experiments which would monitor for charge-transfer between BEDT-TTF molecules and Fe(III) ions.

APPENDIX
TABLES OF CRYSTALLOGRAPHIC DATA

Appendix Table A-1: Crystallographic data and structure refinement for $MnCl_3(C_{12}H_{12}N_2){\cdot}CH_3CN$ (**6**).

Empirical formula	$C_{14}\,H_{15}\,Cl_3\,Mn\,N_3$
Formula weight	386.58 g/mol
Temperature	173(2) K
Wavelength	0.71073 Å
Crystal system	Monoclinic
Space group	P2(1)/n
Unit cell dimensions	a = 7.41180(10) Å, a = 90° b = 16.7280(3) Å, b = 90.7480(10)° c = 13.51680(10) Å, g = 90°
Volume, Z	1675.73(4) $Å^3$, 4
Density (calculated)	1.532 Mg/m^3
Absorption coefficient	1.261 mm^{-1}
F(000)	784
Crystal size	0.25 x 0.19 x 0.19 mm^3
Theta range for data collection	1.94 to 27.50°
Limiting indices	-9<=h<=8, -13<=k<=22, -18<=l<=18
Reflections collected	11406
Independent reflections	3840 [R(int) = 0.0415]
Absorption correction	Semi-empirical from psi-scans
Max. and min. transmission	0.9138 and 0.8170
Refinement method	Full-matrix least-squares on F^2
Data / restraints / parameters	3822 / 0 / 218
Goodness-of-fit on F^2	1.079
Final R indices [$I>2\sigma(I)$]	R1 = 0.0288, wR2 = 0.0702
R indices (all data)	R1 = 0.0334, wR2 = 0.0749
Extinction coefficient	0.0035(6)
Largest diff. peak and hole	0.403 and -0.248 e. $Å^{-3}$

Appendix Table A-2: Atomic coordinates (x 10^4) and equivalent isotropic displacement parameters (Å^2 x 10^3) for **6**. $U_{(eq)}$ is defined as one third of the trace of the orthogonalized U_{ij} tensor.

Atom	x	y	z	$U_{(eq)}$
Mn	1886(1)	820(1)	2026(1)	22(1)
Cl(1)	-693(1)	1527(1)	2166(1)	27(1)
Cl(2)	1787(1)	404(1)	3583(1)	36(1)
Cl(3)	4378(1)	1641(1)	2200(1)	33(1)
N(1)	2650(2)	-311(1)	1509(1)	22(1)
C(2)	3041(2)	-958(1)	2070(1)	27(1)
C(3)	3472(2)	-1693(1)	1666(1)	29(1)
C(4)	3536(2)	-1787(1)	646(1)	26(1)
C(4')	3928(3)	-2583(1)	175(2)	36(1)
C(5)	3178(2)	-1108(1)	61(1)	23(1)
C(6)	2729(2)	-389(1)	508(1)	20(1)
C(7)	2285(2)	350(1)	-49(1)	20(1)
C(8)	2301(2)	417(1)	-1073(1)	23(1)
C(9)	1852(2)	1145(1)	-1528(1)	25(1)
C(9')	1846(3)	1239(1)	-2636(1)	35(1)
C(10)	1419(2)	1785(1)	-913(1)	27(1)
C(11)	1420(2)	1687(1)	104(1)	27(1)
N(12)	1827(2)	980(1)	534(1)	22(1)
N(13)	5552(3)	1449(1)	5583(2)	51(1)
C(14)	6123(3)	1061(1)	4963(2)	36(1)
C(15)	6834(3)	561(1)	4179(2)	42(1)

Appendix Table A-3: Bond lengths [Å] and angles [°] for **6**.

Mn-N(12)	2.0351(14)	C(8)-C(9)	1.401(2)
Mn-N(1)	2.0969(14)	C(8)-H(8)	1.01(2)
Mn-Cl(1)	2.2590(5)	C(9)-C(9')	1.506(2)
Mn-Cl(2)	2.2189(5)	C(9')-H(9'A)	0.96
Mn-Cl(3)	2.3116(5)	C(9')-H(9'B)	0.96
N(1)-C(2)	1.349(2)	C(9')-H(9'C)	0.96
N(1)-C(6)	1.362(2)	C(9')-H(9'D)	1.10
C(2)-C(3)	1.385(2)	C(9')-H(9'E)	1.02
C(2)-H(2)	0.89(2)	C(9')-H(9'F)	1.04
C(3)-C(4)	1.389(3)	C(10)-C(11)	1.384(2)
C(3)-H(3)	0.91(2)	C(10)-H(10)	0.91(2)
C(4)-C(5)	1.406(2)	C(11)-N(12)	1.350(2)
C(4)-C(4')	1.506(2)	C(11)-H(11)	0.97(2)
C(4')-H(4'A)	0.96	N(13)-C(14)	1.145(3)
C(4')-H(4'B)	0.96	C(14)-C(15)	1.454(3)
C(4')-H(4'C)	0.96	C(15)-H(15A)	0.96
C(4')-H(4'D)	0.98	C(15)-H(15B)	0.96
C(4')-H(4'E)	0.93	C(15)-H(15E)	0.96
C(5)-C(6)	1.389(2)	C(15)-H(15F)	0.94
C(6)-C(7)	1.481(2)	C(7)-C(8)	1.389(2)
C(7)-N(12)	1.362(2)		

N(12)-Mn-N(1)	77.96(5)	C(8)-C(7)-C(6)	124.68(14)
N(12)-Mn-Cl(2)	168.86(4)	C(7)-C(8)-C(9)	120.2(2)
N(1)-Mn-Cl(2)	92.61(4)	C(7)-C(8)-H(8)	120.1(12)
N(12)-Mn-Cl(1)	90.36(4)	C(9)-C(8)-H(8)	119.8(12)
N(1)-Mn-Cl(1)	137.16(4)	C(10)-C(9)-C(8)	117.4(2)
Cl(2)-Mn-Cl(1)	92.65(2)	C(10)-C(9)-C(9')	121.0(2)
N(12)-Mn-Cl(3)	91.66(4)	C(8)-C(9)-C(9')	121.6(2)
N(1)-Mn-Cl(3)	110.56(4)	C(9)-C(9')-H(9'A)	109.47(10)
Cl(2)-Mn-Cl(3)	97.27(2)	C(9)-C(9')-H(9'B)	109.47(10)
Cl(1)-Mn-Cl(3)	110.85(2)	H(9'A)-C(9')-H(9'B)	109.5
C(2)-N(1)-C(6)	118.02(14)	C(9)-C(9')-H(9'C)	109.47(10)
C(2)-N(1)-Mn	126.36(11)	H(9'A)-C(9')-H(9'C)	109.5
C(6)-N(1)-Mn	115.62(10)	H(9'B)-C(9')-H(9'C)	109.5
N(1)-C(2)-C(3)	122.7(2)	C(9)-C(9')-H(9'F)	112.14(10)
N(1)-C(2)-H(2)	117.4(13)	C(9)-C(9')-H(9'D)	117.81(10)
C(3)-C(2)-H(2)	119.9(13)	H(9'F)-C(9')-H(9'D)	100.7
C(2)-C(3)-C(4)	120.1(2)	C(9)-C(9')-H(9'E)	106.79(10)
C(2)-C(3)-H(3)	117.5(14)	H(9'F)-C(9')-H(9'E)	109.7
C(4)-C(3)-H(3)	122(2)	H(9'D)-C(9')-H(9'E)	109.6
C(3)-C(4)-C(5)	117.3(2)	C(11)-C(10)-C(9)	120.2(2)
C(3)-C(4)-C(4')	121.9(2)	C(11)-C(10)-H(10)	119.8(13)
C(5)-C(4)-C(4')	120.8(2)	C(9)-C(10)-H(10)	120.0(13)
C(4)-C(4')-H(4'A)	109.47(10)	N(12)-C(11)-C(10)	121.9(2)
C(4)-C(4')-H(4'B)	109.47(10)	N(12)-C(11)-H(11)	115.1(13)
H(4'A)-C(4')-H(4'B)	109.5	C(10)-C(11)-H(11)	122.9(13)
C(4)-C(4')-H(4'C)	109.47(10)	C(11)-N(12)-C(7)	119.07(14)
H(4'A)-C(4')-H(4'C)	109.5	C(11)-N(12)-Mn	122.97(11)
H(4'B)-C(4')-H(4'C)	109.5	C(7)-N(12)-Mn	117.92(11)
C(4)-C(4')-H(4'D)	109.84(10)	N(13)-C(14)-C(15)	179.4(2)

Appendix Table A-3 continued.

C(4)-C(4')-H(4'E)	117.34(10)	C(14)-C(15)-H(15A)	111.44(12)
H(4'D)-C(4')-H(4'E)	110.8	C(14)-C(15)-H(15B)	111.58(12)
C(4)-C(4')-H(4'F)	113.37(10)	H(15A)-C(15)-H(15B)	109.4
H(4'D)-C(4')-H(4'F)	96.6	C(14)-C(15)-H(15C)	101.13(12)
H(4'E)-C(4')-H(4'F)	106.9	H(15A)-C(15)-H(15C)	111.6
C(6)-C(5)-C(4)	119.9(2)	H(15B)-C(15)-H(15C)	111.6
C(6)-C(5)-H(5)	120.6(13)	C(14)-C(15)-H(15D)	105.75(12)
C(4)-C(5)-H(5)	119.4(13)	C(14)-C(15)-H(15E)	115.39(12)
N(1)-C(6)-C(5)	121.89(14)	H(15D)-C(15)-H(15E)	105.8
N(1)-C(6)-C(7)	114.38(14)	C(14)-C(15)-H(15F)	115.82(11)
C(5)-C(6)-C(7)	123.73(14)	H(15D)-C(15)-H(15F)	105.8
N(12)-C(7)-C(8)	121.22(14)	H(15E)-C(15)-H(15F)	107.3
N(12)-C(7)-C(6)	114.10(14)		

Appendix Table B-1: Crystallographic data and structure refinement for α'-(BEDT-TTF)$_2$(HCl$_2$) **(9)**.

Empirical formula	$C_{10}H_8S_8$. 1/2 HCl$_2$
Formula weight	841.20 g/mol
Temperature	173(2) K
Wavelength	0.71073 Å
Crystal system	Monoclinic
Space group	P2/c
Unit cell dimensions	a = 7.7479(1) Å, α = 90° b = 6.6307(1) Å, β = 96.889(1)° c = 30.2362(5) Å, γ = 90°
Volume, Z	1542.14(4) Å^3, 4
Density (calculated)	1.812 Mg/m^3
Absorption coefficient	1.311 mm^{-1}
F(000)	854
Crystal size	0.19 x 0.15 x 0.13 mm^3
Theta range for data collection	1.36 to 25.00°
Limiting indices	-10<=h<=9, -9<=k<=8, -41<=l<=39
Reflections collected	10627
Independent reflections	2705 [R(int) = 0.0701]
Absorption correction	Semi-empirical from psi-scans
Max. and min. transmission	0.891 and 0.787
Refinement method	Full-matrix least-squares on F^2
Data / restraints / parameters	2699 / 65 / 209
Goodness-of-fit on F^2	1.014
Final R indices [I>2σ(I)]	R1 = 0.0456, wR2 = 0.1114
R indices (all data)	R1 = 0.0578, wR2 = 0.1376
Extinction coefficient	0.0007(4)
Largest diff. peak and hole	0.798 and -0.521 e.Å^{-3}

Appendix Table B-2: Atomic coordinates (x 10^4) and equivalent isotropic displacement parameters (Å^2 x 10^3) for **9**. $U_{(eq)}$ is defined as one third of the trace of the orthogonalized Uij tensor.

Atom	x	y	z	$U_{(eq)}$
Cl(1)	1081(1)	-3107(2)	9882(1)	36(1)
S(3)	1951(1)	-1497(1)	7120(1)	26(1)
S(4)	3743(1)	-2833(1)	8099(1)	27(1)
S(9)	4370(1)	1410(1)	8335(1)	24(1)
S(10)	2353(1)	2762(1)	7377(1)	24(1)
S(11)	-158(1)	-729(1)	6257(1)	25(1)
S(12)	4817(2)	-4428(2)	8999(1)	37(1)
S(17)	124(1)	4284(2)	6578(1)	33(1)
S(18)	5644(1)	643(1)	9283(1)	29(1)
C(1)	2671(5)	248(5)	7533(1)	22(1)
C(2)	3468(5)	-317(5)	7941(1)	22(1)
C(5)	873(4)	278(5)	6755(1)	19(1)
C(6)	4513(5)	-2304(5)	8657(1)	21(1)
C(7)	1028(5)	2235(5)	6881(1)	22(1)
C(8)	4807(4)	-357(5)	8768(1)	18(1)
C(13)	-664(6)	1478(6)	5901(1)	30(1)
C(14)	5539(8)	-3356(8)	9540(1)	32(2)
C(14')	6569(12)	-3404(18)	9383(4)	21(4)
C(15)	375(6)	3352(6)	6028(1)	32(1)
C(16)	6713(7)	-1558(7)	9541(2)	30(2)
C(16')	5877(26)	-1633(15)	9614(5)	28(4)

Appendix Table B-3: Bond lengths [Å] and angles [°] for **9**.

Cl(1)-H(1)	1.574(1)	S(18)-C(16')	1.808(3)
S(3)-C(1)	1.743(4)	C(1)-C(2)	1.364(5)
S(3)-C(5)	1.756(3)	C(5)-C(7)	1.354(5)
S(4)-C(2)	1.742(4)	C(6)-C(8)	1.347(5)
S(4)-C(6)	1.753(4)	C(13)-C(15)	1.505(6)
S(9)-C(2)	1.737(4)	C(13)-H(13A)	0.93(4)
S(9)-C(8)	1.759(3)	C(13)-H(13B)	1.07(5)
S(10)-C(1)	1.742(4)	C(14)-C(16)	1.499(7)
S(10)-C(7)	1.747(4)	C(14)-H(14A)	0.97
S(11)-C(5)	1.749(3)	C(14)-H(14B)	0.97
S(11)-C(13)	1.832(4)	C(14')-C(16')	0.97
S(12)-C(14)	1.808(3)	C(15)-H(15A)	1.02(4)
S(17)-C(7)	1.740(4)	C(15)-H(15B)	0.94(4)
S(17)-C(15)	1.806(4)	C(16)-H(16A)	0.97
S(18)-C(8)	1.746(3)	C(16)-H(16B)	0.97
S(18)-C(16)	1.808(3)	C(16')-H(16C)	0.97
C(16')-H(16D)	0.97		

Cl(1)-H(1)-Cl(1)#1	180.0	S(11)-C(13)-H(13A)	104(2)
C(1)-S(3)-C(5)	95.4(2)	C(15)-C(13)-H(13B)	105(3)
C(2)-S(4)-C(6)	95.1(2)	S(11)-C(13)-H(13B)	109(3)
C(2)-S(9)-C(8)	95.5(2)	H(13A)-C(13)-H(13B)	114(3)
C(1)-S(10)-C(7)	95.2(2)	C(16)-C(14)-S(12)	115.9(4)
C(5)-S(11)-C(13)	104.1(2)	C(16)-C(14)-H(14A)	108.3(4)
C(6)-S(12)-C(14')	96.6(5)	S(12)-C(14)-H(14A)	108.3(2)
C(6)-S(12)-C(14)	103.0(2)	C(16)-C(14)-H(14B)	108.3(2)
C(7)-S(17)-C(15)	97.9(2)	S(12)-C(14)-H(14B)	108.3(2)
C(8)-S(18)-C(16)	100.4(2)	H(14A)-C(14)-H(14B)	107.4
C(8)-S(18)-C(16')	100.3(6)	C(16')-C(14')-S(12)	108.1(10)
C(2)-C(1)-S(10)	122.8(3)	C(16')-C(14')-H(14C)	110.1(6)
C(2)-C(1)-S(3)	122.5(3)	S(12)-C(14')-H(14C)	110.1(4)
S(10)-C(1)-S(3)	114.7(2)	C(16')-C(14')-H(14D)	110.1(8)
C(1)-C(2)-S(9)	122.7(3)	S(12)-C(14')-H(14D)	110.1(5)
C(1)-C(2)-S(4)	122.6(3)	H(14C)-C(14')-H(14D)	108.4
S(9)-C(2)-S(4)	114.7(2)	C(13)-C(15)-S(17)	113.8(3)
C(7)-C(5)-S(11)	128.7(3)	C(13)-C(15)-H(15A)	112(2)
C(7)-C(5)-S(3)	116.4(3)	S(17)-C(15)-H(15A)	111(2)
S(11)-C(5)-S(3)	114.8(2)	C(13)-C(15)-H(15B)	105(2)
C(8)-C(6)-S(12)	128.1(3)	S(17)-C(15)-H(15B)	100(2)
C(8)-C(6)-S(4)	117.4(3)	H(15A)-C(15)-H(15B)	114(3)
S(12)-C(6)-S(4)	114.5(2)	C(14)-C(16)-S(18)	113.2(4)
C(5)-C(7)-S(17)	125.6(3)	C(14)-C(16)-H(16A)	08.9(4)
C(5)-C(7)-S(10)	117.3(3)	S(18)-C(16)-H(16A)	108.9(2)
S(17)-C(7)-S(10)	117.0(2)	C(14)-C(16)-H(16B)	108.9(3)
C(6)-C(8)-S(18)	128.4(3)	S(18)-C(16)-H(16B)	108.9(2)
C(6)-C(8)-S(9)	116.2(3)	H(16A)-C(16)-H(16B)	107.7
S(18)-C(8)-S(9)	115.4(2)	C(14')-C(16')-S(18)	114.4(8)
C(15)-C(13)-S(11)	116.0(3)	C(14')-C(16')-H(16C)	108.7(7)
C(15)-C(13)-H(13A)	109(2)	S(18)-C(16')-H(16C)	108.7(6)

Appendix Table B-3 continued.

C(14')-C(16')-H(16D)	108.7(8)
S(18)-C(16')-H(16D)	108.7(6)
H(16C)-C(16')-H(16D)	107.6

Symmetry transformations used to generate equivalent atoms:
#1 -x, -1-y, 2-z

Appendix Table B-4: Crystallographic data and structure refinement for ε-(BEDT-TTF)HCl_2 (**10**).

Empirical formula	$C_{10} H_9 Cl_2 S_8$
Formula weight	456.55
Temperature	233(2) K
Wavelength	0.71073 Å
Crystal system	Monoclinic
Space group	C2/m
Unit cell dimensions	a = 12.9687(8) Å α = 90° b = 11.6077(8) Å β = 104.688(1)° c = 5.6949(4) Å γ = 90°
Volume, Z	829.28(10) $Å^3$, 2
Density (calculated)	1.828 Mg/m^3
Absorption coefficient	1.383 mm^{-1}
F(000)	462
Crystal size	0.17 x 0.09 x 0.08 mm^3
Theta range for data collection	2.39 to 27.48°
Limiting indices	$-15 \leq h \leq 16, -14 \leq k \leq 15, -5 \leq l \leq 7$
Reflections collected	5350
Independent reflections	998 [R(int) = 0.0230]
Absorption correction	None
Refinement method	Full-matrix least-squares on F^2
Data / restraints / parameters	997 / 0 / 63
Goodness-of-fit on F^2	1.049
Final R indices [$I>2\sigma(I)$]	R1 = 0.0290, wR2 = 0.0778 [866]
R indices (all data)	R1 = 0.0352, wR2 = 0.0850
Extinction coefficient	0.0045(12)
Largest diff. peak and hole	0.441 and -0.400 e.$Å^{-3}$

Appendix Table B-5: Atomic coordinates (x 10^4) and equivalent isotropic displacement parameters ($Å^2$ x 10^3) for **10**. $U_{(eq)}$ is defined as one third of the trace of the orthogonalized U_{ij} tensor.

Atom	x	y	z	$U_{(eq)}$
S1	812(1)	3743(1)	2653(1)	30(1)
S2	2203(1)	3500(1)	7602(1)	39(1)
C1	348(2)	5000	1149(4)	25(1)
C2	1551(1)	4414(2)	5275(3)	27(1)
C3	3061(4)	4490(4)	9783(8)	45(1)
C3'	3348(3)	4389(4)	8781(9)	42(1)
Cl	4806(2)	3691(1)	5146(7)	54(1)

Appendix Table B-6: Bond lengths [Å] and angles [˚] for **10**.

S1-C1	1.7214(12)
S1-C2	1.741(2)
S2-C2	1.740(2)
S2-C3'	1.793(5)
S2-C3	1.844(5)
C1-C1#1	1.388(4)
C1-S1#2	1.7214(12)
C2-C2#2	1.360(4)
C3-C3'#2	1.506(6)
C3-H3A	0.96
C3-H3B	0.96
C3'-C3#2	1.506(6)
C3'-H3'A	0.96
C3'-H3'B	0.96
Cl-H	1.5454(10)

C1-S1-C2	95.42(9)
C2-S2-C3'	97.5(2)
C2-S2-C3	103.1(2)
C1#1-C1-S1	122.05(6)
C1#1-C1-S1#2	122.05(6)
S1-C1-S1#2	115.89(13)
C2#2-C2-S2	127.56(6)
C2#2-C2-S1	116.59(6)
S2-C2-S1	115.84(11)
C3'#2-C3-S2	116.6(3)
C3'#2-C3-H3A	109.0(3)
C3'#2-C3-H3b	107.2(2)
S2-C3-H3A	108.8(2)
S2-C3-H3B	107.4(2)
H3A-C3-H3B	107.4
C3#2-C3'-S2	112.2(3)
C3#2-C3'-H3'a	108.3(2)
C3#2-C3'-H3'b	109.6(6)
S2-C3'-H3'A	109.5(2)
S2-C3'-H3'B	109.2(2)
H3'A-C3'-H3'B	108.0
Cl#3-H-Cl	180.0(1)
Cl#2-H-Cl	158.8(1)

Symmetry transformations used to generate equivalent atoms:
#1 -x,-y+1,-z #2 x,-y+1,z #3 -x+1,-y+1,-z+1

Appendix Table B-7: Anisotropic displacement parameters ($Å^2 \times 10^3$) for **10**. The anisotropic displacement factor exponent takes the Form: $-2 \pi^2 [h^2 a^{*2} U_{11} + ... + 2 h k a^* b^* U_{12}]$.

Atom	U_{11}	U_{22}	U_{33}	U_{23}	U_{13}	U_{12}
S1	34(1)	21(1)	28(1)	1(1)	-6(1)	3(1)
S2	43(1)	40(1)	26(1)	9(1)	-6(1)	4(1)
C1	24(1)	19(1)	27(1)	0	-5(1)	0
C2	25(1)	33(1)	21(1)	2(1)	0(1)	3(1)
C3	35(2)	55(3)	33(2)	3(2)	-10(2)	-2(2)
C3'	29(2)	60(3)	35(2)	1(2)	1(2)	10(2)
Cl	78(2)	31(1)	49(1)	2(1)	9(1)	-11(1)

Appendix Table B-8: Hydrogen coordinates (x 10^4) and isotropic displacement parameters ($Å^2$ x 10^3) for **10.**

Atom	x	y	z	$U_{(eq)}$
H3A	3703(4)	4092(4)	10579(8)	54
H3B	2692(4)	4675(4)	10998(8)	54
H3'A	3690(3)	4559(4)	7511(9)	51
H3'B	3847(3)	3976(4)	10033(9)	51
H	5000	5000	5000	89(21)

Appendix Table B-9: Crystallographic data and structure refinement for ε'-(BEDT-TTF)HCl_2 (**11**).

Empirical formula	$C_{10} H_9 Cl_2 S_8$
Formula weight	456.55 g/mol
Temperature	173(2) K
Wavelength	0.71073 Å
Crystal system	Monoclinic
Space group	P2(1)/*c*
Unit cell dimensions	a = 12.7112(1) Å, α = 90° b = 11.5778(2) Å, β = 101.194(1)° c = 11.3583(1) Å, γ = 90K
Volume, Z	1639.77(3) $Å^3$, 4
Density (calculated)	1.849 Mg/m^3
Absorption coefficient	1.398 mm^{-1}
F(000)	924
Crystal size	0.43 x 0.22 x 0.15 mm^3
Theta range for data collection	2.82 to 25.00°
Limiting indices	-16<=h<=15, -14<=k<=8, -7<=l<=14
Reflections collected	10017
Independent reflections	2819 [R(int) = 0.0200]
Absorption correction	Semi-empirical from psi-scans
Max. and min. transmission	0.438 and 0.436
Refinement method	Full-matrix least-squares on F^2
Data / restraints / parameters	2818 / 0 / 217
Goodness-of-fit on F^2	1.155
Final R indices [$I>2\sigma(I)$]	R1 = 0.0378, wR2 = 0.0999
R indices (all data)	R1 = 0.0460, wR2 = 0.1070
Largest diff. peak and hole	0.787 and -0.362 $e.Å^{-3}$

Appendix Table B-10: Atomic coordinates (x 10^4) and equivalent isotropic displacement parameters (Å^2 x 10^3) for **11**. $U_{(eq)}$ is Defined as One third of the trace of the orthogonalized U_{ij} tensor.

Atom	x	y	z	$U_{(eq)}$
Cl(1)	7242(1)	3800(1)	3587(1)	38(1)
Cl(2)	7792(1)	1199(1)	3955(1)	41(1)
S(3)	6696(1)	6242(1)	2142(1)	20(1)
S(4)	8348(1)	6307(1)	331(1)	22(1)
S(9)	6668(1)	8764(1)	2196(1)	23(1)
S(10)	8276(1)	8827(1)	321(1)	21(1)
S(11)	5266(1)	5959(1)	3906(1)	27(1)
S(12)	9703(1)	6088(1)	-1473(1)	26(1)
S(17)	5303(1)	8971(1)	3992(1)	27(1)
S(18)	9671(1)	9091(1)	-1477(1)	26(1)
C(1)	7141(2)	7522(2)	1653(3)	17(1)
C(2)	7842(2)	7551(2)	853(3)	19(1)
C(5)	5947(2)	6883(2)	3096(2)	20(1)
C(6)	9054(2)	7003(2)	-629(2)	19(1)
C(7)	5930(2)	8055(2)	3124(2)	20(1)
C(8)	9021(2)	8178(2)	-629(2)	19(1)
C(13)	4126(2)	6896(3)	3952(3)	33(1)
C(14)	10568(3)	7057(3)	-2126(3)	35(1)
C(15)	4427(3)	7995(3)	4626(3)	38(1)
C(16)	10833(2)	8197(3)	-1495(3)	33(1)

Appendix Table B-11: Bond lengths [Å] and angles [°] for **11**.

Cl(1)-H(1)	1.62(4)	S(18)-C(8)	1.743(3)
Cl(2)-H(1)	1.51(4)	S(18)-C(16)	1.807(3)
S(3)-C(1)	1.716(2)	C(1)-C(2)	1.390(4)
S(3)-C(5)	1.741(3)	C(5)-C(7)	1.358(4)
S(4)-C(2)	1.729(3)	C(6)-C(8)	1.362(4)
S(4)-C(6)	1.739(3)	C(13)-C(15)	1.496(5)
S(9)-C(1)	1.719(2)	C(13)-H(13A)	0.95(4)
S(9)-C(7)	1.746(3)	C(13)-H(13B)	1.12(4)
S(10)-C(2)	1.727(3)	C(14)-C(16)	1.508(5)
S(10)-C(8)	1.738(3)	C(14)-H(14A)	0.97(4)
S(11)-C(5)	1.746(3)	C(14)-H(14B)	1.12(4)
S(11)-C(13)	1.818(3)	C(15)-H(15A)	1.09(4)
S(12)-C(6)	1.740(3)	C(15)-H(15B)	0.94(4)
S(12)-C(14)	1.826(3)	C(16)-H(16A)	1.05(3)
S(17)-C(7)	1.743(3)	C(16)-H(16B)	1.00(4)
S(17)-C(15)	1.830(3)		

Cl(1)-H(1)-Cl(2)	164(4)	S(10)-C(8)-S(18)	117.1(2)
C(1)-S(3)-C(5)	95.05(13)	C(15)-C(13)-S(11)	113.3(2)
C(2)-S(4)-C(6)	95.83(13)	C(15)-C(13)-H(13A)	104(2)
C(1)-S(9)-C(7)	95.14(13)	S(11)-C(13)-H(13A)	109(2)
C(2)-S(10)-C(8)	95.59(13)	C(15)-C(13)-H(13B)	105(2)
C(5)-S(11)-C(13)	97.43(14)	S(11)-C(13)-H(13B)	116(2)
C(6)-S(12)-C(14)	103.70(14)	H(13A)-C(13)-H(13B)	110(3)
C(7)-S(17)-C(15)	103.1(2)	C(16)-C(14)-S(12)	116.2(2)
C(8)-S(18)-C(16)	97.81(14)	C(16)-C(14)-H(14A)	114(2)
C(2)-C(1)-S(3)	121.7(2)	S(12)-C(14)-H(14A)	100(2)
C(2)-C(1)-S(9)	121.8(2)	C(16)-C(14)-H(14B)	108(2)
S(3)-C(1)-S(9)	116.5(2)	S(12)-C(14)-H(14B)	109(2)
C(1)-C(2)-S(10)	122.6(2)	H(14A)-C(14)-H(14B)	110(3)
C(1)-C(2)-S(4)	122.2(2)	C(13)-C(15)-S(17)	116.0(2)
S(10)-C(2)-S(4)	115.3(2)	C(13)-C(15)-H(15A)	109(2)
C(7)-C(5)-S(3)	117.0(2)	S(17)-C(15)-H(15A)	112(2)
C(7)-C(5)-S(11)	126.0(2)	C(13)-C(15)-H(15B)	105(2)
S(3)-C(5)-S(11)	117.0(2)	S(17)-C(15)-H(15B)	106(2)
C(8)-C(6)-S(4)	16.3(2)	H(15A)-C(15)-H(15B)	110(3)
C(8)-C(6)-S(12)	128.8(2)	C(14)-C(16)-S(18)	113.5(2)
S(4)-C(6)-S(12)	114.9(2)	C(14)-C(16)-H(16A)	110(2)
C(5)-C(7)-S(17)	129.3(2)	S(18)-C(16)-H(16A)	107(2)
C(5)-C(7)-S(9)	116.3(2)	C(14)-C(16)-H(16B)	109(2)
S(17)-C(7)-S(9)	114.4(2)	S(18)-C(16)-H(16B)	100(2)
C(6)-C(8)-S(10)	117.0(2)	H(16A)-C(16)-H(16B)	117(3)
C(6)-C(8)-S(18)	126.0(2)		

Appendix Table C-1: Crystallographic data and structure refinement for $(BEDO\text{-}TTF)_4[C_4N_6]\cdot H_2O$ (**14**).

Empirical formula	$C_{44} H_{34} N_6 O_{17} S_{16}$
Formula weight	1431.73
Temperature	173(2) K
Wavelength	0.71073 Å
Crystal system	Triclinic
Space group	P-1
Unit cell dimensions	a = 11.9628(2) Å α = 81.268(1)° b = 14.1016(2) Å β = 70.206(1)° c = 17.0830(3) Å γ = 77.038(1)°
Volume, Z	2633.39(7) A^3, 2
Density (calculated)	1.806 Mg/m^3
Absorption coefficient	0.737 mm^{-1}
F(000)	1464
Crystal size	0.34 x 0.30 x 0.04 mm
Theta range for data collection	1.27 to 25.00°
Limiting indices	$-15 \le h \le 14$, $-18 \le k \le 7$, $-22 \le l \le 22$
Reflections collected	16658
Independent reflections	8946 [R(int) = 0.0396]
Absorption correction	Empirical
Min. & Max. Transmission	0.703, 0.977
Refinement method	Full-matrix least-squares on F^2
Data / restraints / parameters	8913 / 0 / 774
Goodness-of-fit on F^2	1.019
Final R indices [$I>2\sigma(I)$]	R1 = 0.0461, wR2 = 0.1012 [5824]
R indices (all data)	R1 = 0.0802, wR2 = 0.1486
Extinction coefficient	0.0021(2)
Largest diff. peak and hole	0.718 and -0.414 $e.A^{-3}$

Appendix Table C-2: Atomic coordinates (x 10^4) and equivalent isotropic displacement parameters (A^2 x 10^3) for **14**. $U_{(eq)}$ is defined as one third of the trace of the orthogonalized U_{ij} tensor.

Atom	x	y	z	$U_{(eq)}$
C1	2493(3)	9991(2)	5021(2)	17(1)
C2	2059(3)	10069(2)	5867(2)	17(1)
S3	1540(1)	9888(1)	4472(1)	19(1)
S4	550(1)	10059(1)	6434(1)	20(1)
C5	2674(3)	9873(3)	3513(2)	20(1)
C6	729(3)	10177(3)	7380(2)	21(1)
C7	3798(3)	9903(3)	3494(2)	20(1)
C8	1844(3)	10216(3)	7378(2)	20(1)
S9	4002(1)	9999(1)	4446(1)	19(1)
S10	3004(1)	10162(1)	6427(1)	20(1)
O11	2364(2)	9800(2)	2830(1)	25(1)
O12	-263(2)	10208(2)	8065(2)	29(1)
C13	3435(3)	9504(3)	2136(2)	28(1)
C14	101(4)	10036(3)	8816(2)	33(1)
C15	4410(4)	10073(3)	2048(2)	29(1)
C16	1049(4)	10615(3)	8734(2)	34(1)
O17	4777(2)	9888(2)	2804(1)	25(1)
O18	2143(2)	10307(2)	8057(1)	27(1)
C21	4843(3)	7541(2)	5275(2)	17(1)
C22	4428(3)	7609(3)	6119(2)	20(1)
S23	3888(1)	7438(1)	4725(1)	19(1)
S24	2924(1)	7611(1)	6722(1)	21(1)
C25	5037(3)	7370(3)	3770(2)	20(1)
C26	3158(3)	7722(3)	7655(2)	21(1)
C27	6154(3)	7409(3)	3754(2)	20(1)
C28	4295(3)	7744(3)	7620(2)	21(1)
S29	6351(1)	7539(1)	4699(1)	20(1)
S30	5408(1)	7698(1)	6652(1)	20(1)
O31	4732(2)	7282(2)	3088(1)	25(1)
O32	2199(2)	7752(2)	8355(2)	28(1)
C33	5803(3)	7032(3)	2385(2)	25(1)
C34	2539(20)	7531(15)	9060(12)	37(4)
C34'	2555(13)	7991(11)	9068(7)	31(3)
C35	6766(3)	7600(3)	2317(2)	27(1)
C36	3507(11)	8100(14)	8986(6)	26(4)
C36'	3797(8)	7453(10)	9061(4)	30(3)
O37	7140(2)	7383(2)	3065(1)	26(1)
O38	4646(2)	7783(2)	8289(1)	28(1)
C41	7937(3)	4913(3)	4162(2)	19(1)
C42	7513(3)	4995(2)	5005(2)	18(1)
S43	6966(1)	4801(1)	3628(1)	20(1)
S44	5992(1)	5031(1)	5569(1)	19(1)
C45	8103(3)	4720(3)	2662(2)	20(1)
C46	6169(3)	5142(3)	6521(2)	21(1)
C47	9227(3)	4756(3)	2636(2)	20(1)
C48	7297(3)	5145(3)	6518(2)	22(1)

Appendix Table C-2 continued.

Atom	x	y	z	$U_{(eq)}$
S49	9440(1)	4900(1)	3570(1)	21(1)
S50	8458(1)	5064(1)	5570(1)	20(1)
O51	7763(2)	4612(2)	2003(1)	26(1)
O52	5177(2)	5192(2)	7199(1)	25(1)
C53	8836(3)	4342(3)	1296(2)	28(1)
C54	5518(4)	4945(3)	7956(2)	31(1)
C55	9785(3)	4935(3)	1203(2)	27(1)
C56	6517(3)	5482(3)	7909(2)	28(1)
O57	10193(2)	4734(2)	1938(1)	24(1)
O58	7594(2)	5208(2)	7210(1)	27(1)
C61	10119(3)	2439(2)	4800(2)	18(1)
C62	9686(3)	2512(3)	5642(2)	18(1)
S63	9182(1)	2351(1)	4228(1)	19(1)
S64	8174(1)	2524(1)	6220(1)	20(1)
C65	10343(3)	2314(3)	3275(2)	20(1)
C66	8375(3)	2665(3)	7161(2)	21(1)
C67	11455(3)	2340(3)	3281(2)	19(1)
C68	9495(3)	2707(3)	7143(2)	20(1)
S69	11636(1)	2441(1)	4234(1)	19(1)
S70	10646(1)	2628(1)	6188(1)	20(1)
O71	10056(2)	2236(2)	2585(1)	25(1)
O72	7385(2)	2719(2)	7845(1)	27(1)
C73	11154(3)	1937(3)	1904(2)	28(1)
C74	7728(4)	2606(3)	8601(2)	32(1)
C76	8694(3)	3188(3)	8489(2)	29(1)
O77	12456(2)	2314(2)	2598(1)	25(1)
O78	9793(2)	2835(2)	7816(1)	26(1)
C80	7023(3)	6994(3)	203(2)	24(1)
N81	8174(3)	6599(3)	145(2)	37(1)
C82	8903(4)	7202(3)	135(2)	29(1)
N83	9671(3)	7574(3)	113(2)	37(1)
N84	6233(3)	6478(3)	178(2)	39(1)
C85	6717(4)	5515(3)	37(2)	36(1)
N86	6951(4)	4709(3)	-84(2)	41(1)
N87	6653(3)	7976(3)	289(2)	35(1)
C88	5499(4)	8328(3)	293(2)	35(1)
N89	4579(3)	8766(3)	302(2)	47(1)
O1	7497(9)	9830(6)	-210(10)	33(3)
O1'	7315(8)	9903(6)	110(11)	36(3)

Appendix Table C-3: Bond lengths [Å] and angles [°] for **14**.

C1-C2	1.372(5)
C1-S9	1.740(3)
C1-S3	1.745(3)
C2-S4	1.737(3)
C2-S10	1.745(3)
S3-C5	1.737(4)
S4-C6	1.737(3)
C5-C7	1.345(5)
C5-O11	1.363(4)
C6-C8	1.346(5)
C6-O12	1.353(4)
C7-O17	1.351(4)
C7-S9	1.751(3)
C8-O18	1.356(4)
C8-S10	1.742(4)
O11-C13	1.449(4)
O12-C14	1.460(4)
C13-C15	1.514(5)
C13-H13A	0.99
C13-H13B	0.99
C14-C16	1.499(5)
C14-H14A	0.99
C14-H14B	0.99
C15-O17	1.470(4)
C15-H15A	0.99
C15-H15B	0.99
C16-O18	1.453(4)
C16-H16A	0.99
C16-H16B	0.99
C21-C22	1.367(5)
C21-S29	1.737(3)
C21-S23	1.748(3)
C22-S24	1.744(4)
C22-S30	1.745(3)
S23-C25	1.740(4)
S24-C26	1.744(3)
C25-C27	1.341(5)
C25-O31	1.362(4)
C26-O32	1.347(4)
C26-C28	1.348(5)
C27-O37	1.353(4)
C27-S29	1.749(3)
C28-O38	1.355(4)
C28-S30	1.737(4)
O31-C33	1.447(4)
O32-C34	1.37(2)
O32-C34'	1.522(12)
C33-C35	1.510(5)
C33-H33A	0.99
C33-H33B	0.99
C34-C36	1.51(3)
C34-H34A	0.99
C34-H34B	0.99
C34'-C36'	1.51(2)
C34'-H34C	0.99

Appendix Table C-3 continued.

C34'-H34D	0.99
C35-O37	1.460(4)
C35-H35A	0.99
C35-H35B	0.99
C36-O38	1.504(11)
C36-H36A	0.99
C36-H36B	0.99
C36'-O38	1.452(7)
C36'-H36C	0.99
C36'-H36D	0.99
C41-C42	1.368(5)
C41-S49	1.737(3)
C41-S43	1.746(3)
C42-S44	1.741(3)
C42-S50	1.741(3)
S43-C45	1.748(4)
S44-C46	1.745(3)
C45-C47	1.343(5)
C45-O51	1.358(4)
C46-C48	1.348(5)
C46-O52	1.346(4)
C47-O57	1.349(4)
C47-S49	1.745(3)
C48-O58	1.364(4)
C48-S50	1.741(4)
O51-C53	1.456(4)
O52-C54	1.454(4)
C53-C55	1.508(5)
C53-H53A	0.99
C53-H53B	0.99
C54-C56	1.527(5)
C54-H54A	0.99
C54-H54B	0.99
C55-O57	1.462(4)
C55-H55A	0.99
C55-H55B	0.99
C56-O58	1.453(4)
C56-H56A	0.99
C56-H56B	0.99
C61-C62	1.366(5)
C61-S69	1.744(3)
C61-S63	1.751(3)
C62-S64	1.740(3)
C62-S70	1.752(3)
S63-C65	1.744(4)
S64-C66	1.750(3)
C65-C67	1.342(5)
C65-O71	1.360(4)
C66-C68	1.345(5)
C66-O72	1.351(4)
C67-O77	1.358(4)
C67-S69	1.743(3)
C68-O78	1.359(4)
C68-S70	1.742(4)
O71-C73	1.457(4)

Appendix Table C-3 continued.

O72-C74	1.459(4)
C73-C75	1.505(5)
C73-H73A	0.99
C73-H73B	0.99
C74-C76	1.508(5)
C74-H74A	0.99
C74-H74B	0.99
C75-O77	1.457(4)
C75-H75A	0.99
C75-H75B	0.99
C76-O78	1.468(4)
C76-H76A	0.99
C76-H76B	0.99
C80-N84	1.330(5)
C80-N81	1.341(5)
C80-N87	1.370(5)
N81-C82	1.342(5)
C82-N83	1.143(5)
N84-C85	1.375(6)
C85-N86	1.141(6)
N87-C88	1.357(5)
C88-N89	1.131(5)
O1-H1A	0.93(5)
O1-H1B	0.90(5)
O1'-H1A	0.91(5)
O1'-H1B	0.97(5)

C2-C1-S9	122.2(3)
C2-C1-S3	120.9(3)
S9-C1-S3	116.9(2)
C1-C2-S4	121.7(3)
C1-C2-S10	121.4(3)
S4-C2-S10	116.9(2)
C5-S3-C1	93.7(2)
C6-S4-C2	94.0(2)
C7-C5-O11	124.4(3)
C7-C5-S3	118.4(3)
O11-C5-S3	117.2(3)
C8-C6-O12	125.0(3)
C8-C6-S4	117.7(3)
O12-C6-S4	117.3(3)
C5-C7-O17	125.7(3)
C5-C7-S9	117.1(3)
O17-C7-S9	117.2(3)
C6-C8-O18	125.5(3)
C6-C8-S10	117.9(3)
O18-C8-S10	116.7(3)
C1-S9-C7	93.9(2)
C8-S10-C2	93.6(2)
C5-O11-C13	110.5(3)
C6-O12-C14	109.7(3)
O11-C13-C15	111.1(3)
O11-C13-H13A	109.4(2)
C15-C13-H13A	109.4(2)
O11-C13-H13B	109.4(2)

Appendix Table C-3 continued.

C15-C13-H13B	109.4(2)
H13A-C13-H13B	108.0
O12-C14-C16	110.6(3)
O12-C14-H14A	109.5(2)
C16-C14-H14A	109.5(2)
O12-C14-H14B	109.5(2)
C16-C14-H14B	109.5(2)
H14A-C14-H14B	108.1
O17-C15-C13	110.3(3)
O17-C15-H15A	109.6(2)
C13-C15-H15A	109.6(2)
O17-C15-H15B	109.6(2)
C13-C15-H15B	109.6(2)
H15A-C15-H15B	108.1
O18-C16-C14	111.0(3)
O18-C16-H16A	109.4(2)
C14-C16-H16A	109.4(2)
O18-C16-H16B	109.4(2)
C14-C16-H16B	109.4(2)
H16A-C16-H16B	108.0
C7-O17-C15	110.5(3)
C8-O18-C16	109.3(3)
C22-C21-S29	121.7(3)
C22-C21-S23	121.7(3)
S29-C21-S23	116.7(2)
C21-C22-S24	123.2(3)
C21-C22-S30	120.5(3)
S24-C22-S30	116.3(2)
C25-S23-C21	93.8(2)
C26-S24-C22	94.3(2)
C27-C25-O31	124.6(3)
C27-C25-S23	118.1(3)
O31-C25-S23	117.3(2)
O32-C26-C28	125.1(3)
O32-C26-S24	117.6(3)
C28-C26-S24	117.2(3)
C25-C27-O37	125.6(3)
C25-C27-S29	117.4(3)
O37-C27-S29	116.9(2)
C26-C28-O38	124.9(3)
C26-C28-S30	118.0(3)
O38-C28-S30	117.0(3)
C21-S29-C27	94.0(2)
C28-S30-C22	94.2(2)
C25-O31-C33	110.7(3)
C26-O32-C34	112.1(9)
C26-O32-C34'	109.0(5)
O31-C33-C35	111.8(3)
O31-C33-H33A	109.3(2)
C35-C33-H33A	109.3(2)
O31-C33-H33B	109.3(2)
C35-C33-H33B	109.3(2)
H33A-C33-H33B	107.9
O32-C34-C36	109(2)
O32-C34-H34A	109.9(9)

Appendix Table C-3 continued.

C36-C34-H34A	109.9(12)
O32-C34-H34B	109.9(9)
C36-C34-H34B	109.9(9)
H34A-C34-H34B	108.3
C36'-C34'-O32	112.3(10)
C36'-C34'-H34C	109.1(8)
O32-C34'-H34C	109.1(5)
C36'-C34'-H34D	109.1(6)
O32-C34'-H34D	109.1(5)
H34C-C34'-H34D	107.9
O37-C35-C33	110.3(3)
O37-C35-H35A	109.6(2)
C33-C35-H35A	109.6(2)
O37-C35-H35B	109.6(2)
C33-C35-H35B	109.6(2)
H35A-C35-H35B	108.1
O38-C36-C34	111.6(13)
O38-C36-H36A	109.3(7)
C34-C36-H36A	109.3(12)
O38-C36-H36B	109.3(5)
C34-C36-H36B	109.3(9)
H36A-C36-H36B	108.0
O38-C36'-C34'	106.9(9)
O38-C36'-H36C	110.3(3)
C34'-C36'-H36C	110.3(6)
O38-C36'-H36D	110.3(5)
C34'-C36'-H36D	110.3(8)
H36C-C36'-H36D	108.6
C27-O37-C35	109.8(3)
C28-O38-C36'	111.6(4)
C28-O38-C36	106.2(5)
C42-C41-S49	123.0(3)
C42-C41-S43	120.6(3)
S49-C41-S43	116.4(2)
C41-C42-S44	121.3(3)
C41-C42-S50	122.2(3)
S44-C42-S50	116.5(2)
C41-S43-C45	94.0(2)
C42-S44-C46	94.3(2)
C47-C45-O51	125.9(3)
C47-C45-S43	117.7(3)
O51-C45-S43	116.4(2)
C48-C46-O52	125.5(3)
C48-C46-S44	117.1(3)
O52-C46-S44	117.3(3)
C45-C47-O57	125.0(3)
C45-C47-S49	117.5(3)
O57-C47-S49	117.5(3)
C46-C48-O58	124.5(3)
C46-C48-S50	118.1(3)
O58-C48-S50	117.5(3)
C41-S49-C47	94.4(2)
C48-S50-C42	94.0(2)
C45-O51-C53	109.4(3)
C46-O52-C54	110.3(3)

Appendix Table C-3 continued.

O51-C53-C55	111.3(3)
O51-C53-H53A	109.4(2)
C55-C53-H53A	109.4(2)
O51-C53-H53B	109.4(2)
C55-C53-H53B	109.4(2)
H53A-C53-H53B	108.0
O52-C54-C56	110.1(3)
O52-C54-H54A	109.6(2)
C56-C54-H54A	109.6(2)
O52-C54-H54B	109.6(2)
C56-C54-H54B	109.6(2)
H54A-C54-H54B	108.2
O57-C55-C53	110.2(3)
O57-C55-H55A	109.6(2)
C53-C55-H55A	109.6(2)
O57-C55-H55B	109.6(2)
C53-C55-H55B	109.6(2)
H55A-C55-H55B	108.1
O58-C56-C54	111.3(3)
O58-C56-H56A	109.4(2)
C54-C56-H56A	109.4(2)
O58-C56-H56B	109.4(2)
C54-C56-H56B	109.4(2)
H56A-C56-H56B	108.0
C47-O57-C55	109.6(3)
C48-O58-C56	110.9(3)
C62-C61-S69	121.6(3)
C62-C61-S63	122.0(3)
S69-C61-S63	116.3(2)
C61-C62-S64	122.5(3)
C61-C62-S70	120.6(3)
S64-C62-S70	116.9(2)
C65-S63-C61	94.0(2)
C62-S64-C66	93.8(2)
C67-C65-O71	125.0(3)
C67-C65-S63	117.7(3)
O71-C65-S63	117.3(2)
C68-C66-O72	125.6(3)
C68-C66-S64	117.6(3)
O72-C66-S64	116.8(2)
C65-C67-O77	125.2(3)
C65-C67-S69	117.9(3)
O77-C67-S69	116.8(2)
C66-C68-O78	124.7(3)
C66-C68-S70	118.0(3)
O78-C68-S70	117.2(2)
C67-S69-C61	94.0(2)
C68-S70-C62	93.7(2)
C65-O71-C73	109.9(3)
C66-O72-C74	110.5(3)
O71-C73-C75	110.8(3)
O71-C73-H73A	109.5(2)
C75-C73-H73A	109.5(2)
O71-C73-H73B	109.5(2)
C75-C73-H73B	109.5(2)

Appendix Table C-3 continued.

H73A-C73-H73B	108.1
O72-C74-C76	110.6(3)
O72-C74-H74A	109.5(2)
C76-C74-H74A	109.5(2)
O72-C74-H74B	109.5(2)
C76-C74-H74B	109.5(2)
H74A-C74-H74B	108.1
O77-C75-C73	110.6(3)
O77-C75-H75A	109.5(2)
C73-C75-H75A	109.5(2)
O77-C75-H75B	109.5(2)
C73-C75-H75B	109.5(2)
H75A-C75-H75B	108.1
O78-C76-C74	110.6(3)
O78-C76-H76A	109.5(2)
C74-C76-H76A	109.5(2)
O78-C76-H76B	109.5(2)
C74-C76-H76B	109.5(2)
H76A-C76-H76B	108.1
C67-O77-C75	109.9(3)
C68-O78-C76	109.8(3)
N84-C80-N81	123.0(4)
N84-C80-N87	119.0(4)
N81-C80-N87	117.9(4)
C82-N81-C80	117.7(4)
N83-C82-N81	168.3(5)
C80-N84-C85	114.2(4)
N86-C85-N84	169.7(5)
C88-N87-C80	114.3(4)
N89-C88-N87	168.7(5)
H1A-O1-H1B	113(4)
H1A-O1'-H1B	108(4)

Appendix Table C-4: Anisotropic displacement parameters (A^2 x 10^3) for **14**. The anisotropic displacement factor exponent takes the form: $-2 \pi^2 [h^2 a^{*2} U_{11} + ... + 2 h k a^* b^* U_{12}]$.

Atom	U11	U22	U33	U23	U13	U12
C1	16(2)	14(2)	23(2)	1(1)	-8(2)	-4(2)
C2	16(2)	17(2)	19(2)	-3(2)	-6(2)	-3(2)
S3	16(1)	24(1)	21(1)	-2(1)	-8(1)	-5(1)
S4	17(1)	25(1)	20(1)	-4(1)	-6(1)	-6(1)
C5	24(2)	19(2)	20(2)	0(2)	-11(2)	-4(2)
C6	20(2)	21(2)	21(2)	-6(2)	-2(2)	-4(2)
C7	25(2)	19(2)	18(2)	-3(2)	-7(2)	-6(2)
C8	23(2)	22(2)	18(2)	-3(2)	-9(2)	-6(2)
S9	15(1)	25(1)	19(1)	-2(1)	-6(1)	-6(1)
S10	18(1)	24(1)	20(1)	-2(1)	-7(1)	-6(1)
O11	29(2)	31(2)	21(1)	-4(1)	-12(1)	-8(1)
O12	23(2)	40(2)	22(1)	-5(1)	-4(1)	-7(1)
C13	33(2)	29(2)	21(2)	-4(2)	-9(2)	-2(2)
C14	31(2)	46(3)	16(2)	1(2)	-3(2)	-6(2)
C15	35(2)	34(2)	18(2)	-2(2)	-8(2)	-8(2)
C16	36(2)	42(3)	22(2)	-10(2)	-10(2)	2(2)
O17	20(1)	32(2)	21(1)	-4(1)	-3(1)	-6(1)
O18	28(2)	37(2)	20(1)	-6(1)	-9(1)	-11(1)
C21	15(2)	16(2)	20(2)	-2(2)	-6(2)	-3(2)
C22	18(2)	19(2)	24(2)	-1(2)	-11(2)	-2(2)
S23	16(1)	25(1)	18(1)	-4(1)	-7(1)	-5(1)
S24	15(1)	26(1)	21(1)	-3(1)	-4(1)	-6(1)
C25	23(2)	21(2)	17(2)	-2(2)	-8(2)	-4(2)
C26	20(2)	23(2)	18(2)	-3(2)	-1(2)	-7(2)
C27	18(2)	22(2)	17(2)	-5(2)	-3(2)	-3(2)
C28	22(2)	19(2)	20(2)	-3(2)	-4(2)	-4(2)
S29	15(1)	27(1)	19(1)	-3(1)	-5(1)	-6(1)
S30	17(1)	28(1)	17(1)	-2(1)	-6(1)	-7(1)
O31	23(1)	39(2)	18(1)	-8(1)	-7(1)	-9(1)
O32	23(2)	35(2)	21(1)	-5(1)	2(1)	-9(1)
C33	27(2)	28(2)	17(2)	-6(2)	-5(2)	-1(2)
C34	36(8)	51(11)	24(6)	-1(9)	-9(5)	-13(10)
C34'	35(5)	52(8)	10(3)	-2(6)	-1(3)	-24(7)
C35	29(2)	36(2)	16(2)	-5(2)	-2(2)	-11(2)
C36	33(7)	33(10)	14(5)	-9(5)	-6(4)	-6(6)
C36'	37(5)	35(7)	15(3)	2(3)	-5(3)	-12(5)
O37	18(1)	38(2)	20(1)	-7(1)	0(1)	-8(1)
O38	31(2)	42(2)	17(1)	-4(1)	-7(1)	-15(1)
C41	15(2)	19(2)	21(2)	-4(2)	-3(2)	-3(2)
C42	15(2)	14(2)	24(2)	-3(2)	-9(2)	0(2)
S43	15(1)	27(1)	20(1)	-5(1)	-5(1)	-4(1)
S44	13(1)	26(1)	20(1)	-5(1)	-4(1)	-5(1)
C45	16(2)	25(2)	19(2)	-2(2)	-5(2)	-3(2)
C46	20(2)	23(2)	18(2)	-3(2)	-4(2)	-3(2)
C47	20(2)	19(2)	19(2)	-3(2)	-2(2)	-3(2)
C48	26(2)	22(2)	21(2)	-4(2)	-11(2)	-2(2)
S49	16(1)	26(1)	21(1)	-5(1)	-5(1)	-5(1)
S50	15(1)	26(1)	22(1)	-4(1)	-8(1)	-4(1)
O51	21(1)	41(2)	18(1)	-8(1)	-6(1)	-6(1)
O52	21(1)	33(2)	20(1)	-4(1)	-2(1)	-7(1)
C53	27(2)	36(2)	17(2)	-10(2)	-5(2)	3(2)

Appendix Table C-4 continued.

Atom	U11	U22	U33	U23	U13	U12
C54	34(2)	36(2)	19(2)	3(2)	-5(2)	-8(2)
C55	23(2)	37(2)	17(2)	3(2)	-4(2)	-3(2)
C56	33(2)	32(2)	21(2)	-2(2)	-11(2)	-3(2)
O57	18(1)	30(2)	20(1)	-2(1)	-3(1)	-3(1)
O58	27(2)	38(2)	21(1)	-6(1)	-11(1)	-7(1)
C61	15(2)	15(2)	26(2)	-2(2)	-9(2)	-2(2)
C62	14(2)	16(2)	23(2)	-4(2)	-6(2)	-1(2)
S63	16(1)	25(1)	19(1)	-2(1)	-7(1)	-5(1)
S64	15(1)	26(1)	19(1)	-5(1)	-6(1)	-5(1)
C65	20(2)	20(2)	21(2)	-1(2)	-8(2)	-4(2)
C66	21(2)	24(2)	17(2)	-4(2)	-5(2)	-5(2)
C67	19(2)	20(2)	17(2)	-1(2)	-4(2)	-3(2)
C68	20(2)	22(2)	20(2)	-3(2)	-6(2)	-6(2)
S69	14(1)	24(1)	19(1)	-4(1)	-5(1)	-5(1)
S70	16(1)	26(1)	21(1)	-6(1)	-6(1)	-5(1)
O71	29(2)	33(2)	18(1)	-2(1)	-10(1)	-8(1)
O72	22(1)	41(2)	20(1)	-5(1)	-6(1)	-8(1)
C73	35(2)	31(2)	18(2)	0(2)	-11(2)	-3(2)
C74	33(2)	46(3)	18(2)	2(2)	-6(2)	-16(2)
C75	33(2)	29(2)	12(2)	4(2)	-5(2)	-4(2)
C76	28(2)	43(3)	18(2)	-7(2)	-7(2)	-7(2)
O77	24(2)	32(2)	18(1)	-1(1)	-5(1)	-5(1)
O78	23(2)	41(2)	17(1)	-7(1)	-5(1)	-9(1)
C80	25(2)	30(2)	14(2)	-2(2)	-5(2)	0(2)
N81	36(2)	40(2)	31(2)	-1(2)	-12(2)	1(2)
C82	31(2)	36(2)	19(2)	-4(2)	-9(2)	0(2)
N83	30(2)	46(2)	36(2)	-12(2)	-13(2)	-1(2)
N84	40(2)	48(2)	29(2)	-4(2)	-6(2)	-17(2)
C85	48(3)	38(3)	20(2)	1(2)	-5(2)	-16(2)
N86	53(3)	35(2)	36(2)	-4(2)	-14(2)	-7(2)
N87	39(2)	33(2)	30(2)	-7(2)	-9(2)	-5(2)
C88	34(3)	35(2)	30(2)	-9(2)	-9(2)	5(2)
N89	35(2)	44(2)	65(3)	-20(2)	-22(2)	9(2)

Appendix Table D-1: Crystallographic data and structure refinement for $(BEDT\text{-}TTF)_4[Fe(CN)_6]\cdot 2CH_2Cl_2$ **(15)**.

Empirical formula	$C_{24} H_{18} Cl_2 Fe_{0.50} N_3 S_{16}$	
Formula weight	960.20 g/mol	
Temperature	173(2) K	
Wavelength	0.71073 Å	
Crystal system	Triclinic	
Space group	P-1	
Unit cell dimensions	a = 9.5783(3) Å b = 10.9977(3) Å c = 18.6824(6) Å	α = 77.960(1)° β = 84.38° γ = 67.139(1)°
Volume, Z	1773.20(9) $Å^3$,	2
Density (calculated)	1.798 Mg/m^3	
Absorption coefficient	1.349 mm^{-1}	
F(000)	972	
Crystal size	0.27 x 0.09 x 0.08 mm^3	
Theta range for data collection	2.05 to 25.00°	
Limiting indices	$-13 \leq h \leq 13$, $-8 \leq k \leq 15$, $-20 \leq l \leq 24$	
Reflections collected	12140	
Independent reflections	6090 [R(int) = 0.0222]	
Absorption correction	None	
Refinement method	Full-matrix least-squares on F^2	
Data / restraints / parameters	6062 / 0 / 414	
Goodness-of-fit on F^2	1.012	
Final R indices [$I>2\sigma(I)$]	R1 = 0.0419, wR2 = 0.0884 [4554]	
R indices (all data)	R1 = 0.0634, wR2 = 0.1000	
Extinction coefficient	0.0001(2)	
Largest diff. peak and hole	0.454 and -0.510 e.$Å^{-3}$	

Appendix Table D-2: Atomic coordinates (x 10^4) and equivalent isotropic displacement parameters (A^2 x 10^3) for **15**. $U_{(eq)}$ is defined as one third of the trace of the orthogonalized U_{ij} tensor.

Atom	x	y	z	$U_{(eq)}$
C1	3697(4)	18500(4)	-4775(2)	32(1)
C2	3453(4)	18014(4)	-4048(2)	32(1)
S3	2226(1)	19545(1)	-5354(1)	40(1)
S4	1669(1)	18465(1)	-3640(1)	38(1)
C5	3386(4)	19826(4)	-6101(2)	31(1)
C6	2286(4)	17600(4)	-2756(2)	31(1)
C7	4899(4)	19151(4)	-6014(2)	34(1)
C8	3794(4)	16898(4)	-2684(2)	31(1)
S9	5489(1)	18087(1)	-5174(1)	42(1)
S10	4917(1)	16958(1)	-3474(1)	37(1)
S11	2407(1)	20951(1)	-6851(1)	45(1)
S12	845(1)	17823(1)	-2094(1)	37(1)
C13	3849(5)	20866(4)	-7567(2)	41(1)
C14	1861(4)	16741(4)	-1285(2)	38(1)
C15	5207(5)	19570(4)	-7489(2)	43(1)
C16	3393(4)	16754(4)	-1213(2)	39(1)
S17	6295(1)	19199(1)	-6677(1)	47(1)
S18	4759(1)	15966(1)	-1883(1)	40(1)
C21	-1077(4)	24227(4)	-5614(2)	32(1)
C22	-1328(4)	23751(4)	-4894(2)	32(1)
S23	-2513(1)	25252(1)	-6211(1)	38(1)
S24	-3126(1)	24191(1)	-4492(1)	37(1)
C25	-1341(4)	25285(4)	-6988(2)	30(1)
C26	-2518(4)	23247(4)	-3624(2)	29(1)
C27	158(4)	24608(4)	-6881(2)	32(1)
C28	-1007(4)	22550(4)	-3544(2)	30(1)
S29	741(1)	23781(1)	-5992(1)	39(1)
S30	138(1)	22682(1)	-4316(1)	40(1)
S31	-2265(1)	26186(1)	-7801(1)	39(1)
S32	-3959(1)	23378(1)	-2965(1)	39(1)
C33	-700(4)	26352(4)	-8385(2)	40(1)
C34	-2881(4)	22659(4)	-2135(2)	38(1)
C35	671(4)	25058(4)	-8373(2)	40(1)
C36	-1560(4)	21351(4)	-2174(2)	38(1)
S37	1654(1)	24439(1)	-7515(1)	44(1)
S38	-22(1)	21520(1)	-2766(1)	40(1)
Fe	0	10000	0	28(1)
N41	2187(4)	7063(4)	532(2)	47(1)
N42	1742(4)	11109(4)	839(2)	47(1)
N43	-2078(4)	9860(4)	1364(2)	43(1)
C41	1378(4)	8148(4)	346(2)	33(1)
C42	1129(4)	10697(4)	515(2)	34(1)
C43	-1309(4)	9904(4)	856(2)	31(1)
Cl1	4337(2)	11620(2)	-762(1)	74(1)
Cl2	3492(2)	13689(2)	125(1)	89(1)
C44	4569(5)	12004(5)	64(3)	58(1)

Appendix Table D-3: Bond lengths [Å] and angles [°] for **15**.

C1-C2	1.384(5)
C1-S9	1.730(4)
C1-S3	1.732(4)
C2-S10	1.724(4)
C2-S4	1.730(4)
S3-C5	1.750(4)
S4-C6	1.756(4)
C5-C7	1.356(5)
C5-S11	1.733(4)
C6-C8	1.352(5)
C6-S12	1.738(4)
C7-S17	1.739(4)
C7-S9	1.746(4)
C8-S18	1.743(4)
C8-S10	1.745(4)
S11-C13	1.816(4)
S12-C14	1.813(4)
C13-C15	1.501(6)
C13-H13A	0.97
C13-H13B	0.97
C14-C16	1.492(5)
C14-H14A	0.97
C14-H14B	0.97
C15-S17	1.811(4)
C15-H15A	0.97
C15-H15B	0.97
C16-S18	1.811(4)
C16-H16A	0.97
C16-H16B	0.97
C21-C22	1.372(5)
C21-S23	1.726(4)
C21-S29	1.735(4)
C22-S30	1.734(4)
C22-S24	1.737(4)
S23-C25	1.748(4)
S24-C26	1.750(3)
C25-C27	1.349(5)
C25-S31	1.739(4)
C26-C28	1.355(5)
C26-S32	1.740(4)
C27-S37	1.745(4)
C27-S29	1.748(4)
C28-S30	1.741(4)
C28-S38	1.743(4)
S31-C33	1.812(4)
S32-C34	1.807(4)
C33-C35	1.513(5)
C33-H33A	0.97
C33-H33B	0.97
C34-C36	1.512(5)
C34-H34A	0.97
C34-H34B	0.97
C35-S37	1.806(4)
C35-H35A	0.97
C35-H35B	0.97

Appendix Table D-3 continued.

C36-S38	1.799(4)
C36-H36A	0.97
C36-H36B	0.97
Fe-C43	1.945(4)
Fe-C43#1	1.945(4)
Fe-C41	1.959(4)
Fe-C41#1	1.959(4)
Fe-C42#1	1.960(4)
Fe-C42	1.960(4)
N41-C41	1.143(5)
N42-C42	1.143(5)
N43-C43	1.147(4)
Cl1-C44	1.738(5)
Cl2-C44	1.759(5)
C44-H44A	0.97
C44-H44B	0.97
C2-C1-S9	122.5(3)
C2-C1-S3	122.3(3)
S9-C1-S3	115.2(2)
C1-C2-S10	122.3(3)
C1-C2-S4	122.6(3)
S10-C2-S4	115.0(2)
C1-S3-C5	95.6(2)
C2-S4-C6	95.8(2)
C7-C5-S11	129.4(3)
C7-C5-S3	116.4(3)
S11-C5-S3	114.2(2)
C8-C6-S12	129.7(3)
C8-C6-S4	116.2(3)
S12-C6-S4	114.1(2)
C5-C7-S17	125.9(3)
C5-C7-S9	116.9(3)
S17-C7-S9	117.2(2)
C6-C8-S18	127.3(3)
C6-C8-S10	116.8(3)
S18-C8-S10	115.9(2)
C1-S9-C7	95.6(2)
C2-S10-C8	96.1(2)
C5-S11-C13	104.3(2)
C6-S12-C14	101.8(2)
C15-C13-S11	115.3(3)
C15-C13-H13A	108.4(2)
S11-C13-H13A	108.44(14)
C15-C13-H13B	108.4(2)
S11-C13-H13B	108.4(2)
H13A-C13-H13B	107.5
C16-C14-S12	115.0(3)
C16-C14-H14A	108.5(2)
S12-C14-H14A	108.53(12)
C16-C14-H14B	108.5(2)
S12-C14-H14B	108.53(14)
H14A-C14-H14B	107.5
C13-C15-S17	114.3(3)
C13-C15-H15A	108.7(2)

Appendix Table D-3 continued.

S17-C15-H15A	108.67(13)
C13-C15-H15B	108.7(2)
S17-C15-H15B	108.67(14)
H15A-C15-H15B	107.6
C14-C16-S18	113.1(3)
C14-C16-H16A	108.9(2)
S18-C16-H16A	108.95(13)
C14-C16-H16B	108.9(2)
S18-C16-H16B	108.95(14)
H16A-C16-H16B	107.8
C7-S17-C15	99.2(2)
C8-S18-C16	99.7(2)
C22-C21-S23	123.4(3)
C22-C21-S29	121.2(3)
S23-C21-S29	115.4(2)
C21-C22-S30	122.2(3)
C21-C22-S24	122.7(3)
S30-C22-S24	115.2(2)
C21-S23-C25	95.9(2)
C22-S24-C26	95.4(2)
C27-C25-S31	128.4(3)
C27-C25-S23	116.0(3)
S31-C25-S23	115.6(2)
C28-C26-S32	128.6(3)
C28-C26-S24	116.8(3)
S32-C26-S24	114.5(2)
C25-C27-S37	128.9(3)
C25-C27-S29	117.6(3)
S37-C27-S29	113.5(2)
C26-C28-S30	116.8(3)
C26-C28-S38	128.9(3)
S30-C28-S38	114.2(2)
C21-S29-C27	95.0(2)
C22-S30-C28	95.8(2)
C25-S31-C33	101.3(2)
C26-S32-C34	101.2(2)
C35-C33-S31	114.5(3)
C35-C33-H33A	108.6(2)
S31-C33-H33A	108.64(13)
C35-C33-H33B	108.6(2)
S31-C33-H33B	108.6(2)
H33A-C33-H33B	107.6
C36-C34-S32	113.7(3)
C36-C34-H34A	108.8(2)
S32-C34-H34A	108.82(14)
C36-C34-H34B	108.8(2)
S32-C34-H34B	108.82(12)
H34A-C34-H34B	107.7
C33-C35-S37	113.8(3)
C33-C35-H35A	108.8(2)
S37-C35-H35A	108.79(13)
C33-C35-H35B	108.8(2)
S37-C35-H35B	108.79(14)
H35A-C35-H35B	107.7
C34-C36-S38	114.5(3)

Appendix Table D-3 continued.

C34-C36-H36A	108.6(2)
S38-C36-H36A	108.64(14)
C34-C36-H36B	108.6(2)
S38-C36-H36B	108.64(13)
H36A-C36-H36B	107.6
C27-S37-C35	101.9(2)
C28-S38-C36	100.7(2)
C43-Fe-C43#1	180.0
C43-Fe-C41	90.54(14)
C43#1-Fe-C41	89.46(14)
C43-Fe-C41#1	89.46(14)
C43#1-Fe-C41#1	90.54(14)
C41-Fe-C41#1	180.0
C43-Fe-C42#1	89.5(2)
C43#1-Fe-C42#1	90.5(2)
C41-Fe-C42#1	88.7(2)
C41#1-Fe-C42#1	91.3(2)
C43-Fe-C42	90.5(2)
C43#1-Fe-C42	89.5(2)
C41-Fe-C42	91.3(2)
C41#1-Fe-C42	88.7(2)
C42#1-Fe-C42	180.000(1)
N41-C41-Fe	178.5(3)
N42-C42-Fe	177.0(3)
N43-C43-Fe	179.1(4)
Cl1-C44-Cl2	112.6(3)
Cl1-C44-H44A	109.1(2)
Cl2-C44-H44A	109.1(2)
Cl1-C44-H44B	109.1(2)
Cl2-C44-H44B	109.1(2)
H44A-C44-H44B	107.8

Symmetry transformations used to generate equivalent atoms:
#1 -x,-y+2,-z

Appendix Table D-4: Anisotropic displacement parameters ($A^2 \times 10^3$) for **15**. The anisotropic displacement factor exponent takes the form: $-2 \pi^2 [h^2 a^{*2} U_{11} + ... + 2 h k a^* b^* U_{12}]$.

Atom	U11	U22	U33	U23	U13	U12
C1	28(2)	37(2)	26(2)	-4(2)	1(2)	-8(2)
C2	27(2)	38(2)	27(2)	-4(2)	1(2)	-9(2)
S3	27(1)	54(1)	28(1)	2(1)	2(1)	-9(1)
S4	30(1)	48(1)	26(1)	0(1)	0(1)	-7(1)
C5	32(2)	35(2)	25(2)	-5(2)	5(2)	-12(2)
C6	35(2)	30(2)	26(2)	-2(2)	0(2)	-11(2)
C7	30(2)	40(2)	29(2)	-2(2)	4(2)	-12(2)
C8	34(2)	32(2)	24(2)	0(2)	-2(2)	-9(2)
S9	28(1)	52(1)	31(1)	3(1)	0(1)	-6(1)
S10	29(1)	44(1)	27(1)	-1(1)	2(1)	-6(1)
S11	37(1)	48(1)	29(1)	3(1)	1(1)	-1(1)
S12	28(1)	43(1)	29(1)	-1(1)	2(1)	-7(1)
C13	47(3)	42(2)	30(2)	1(2)	2(2)	-17(2)
C14	37(2)	46(2)	25(2)	-5(2)	3(2)	-10(2)
C15	47(3)	46(3)	36(2)	-9(2)	12(2)	-19(2)
C16	41(2)	42(2)	31(2)	-10(2)	-2(2)	-11(2)
S17	30(1)	61(1)	40(1)	0(1)	7(1)	-14(1)
S18	31(1)	48(1)	28(1)	1(1)	-1(1)	-3(1)
C21	28(2)	37(2)	27(2)	-3(2)	-4(2)	-8(2)
C22	28(2)	38(2)	25(2)	-2(2)	-2(2)	-8(2)
S23	26(1)	51(1)	25(1)	0(1)	0(1)	-5(1)
S24	28(1)	49(1)	24(1)	2(1)	-2(1)	-6(1)
C25	29(2)	31(2)	26(2)	-4(2)	2(2)	-8(2)
C26	30(2)	29(2)	24(2)	1(2)	-3(2)	-7(2)
C27	34(2)	30(2)	29(2)	-1(2)	0(2)	-10(2)
C28	29(2)	32(2)	25(2)	-4(2)	1(2)	-7(2)
S29	28(1)	51(1)	27(1)	0(1)	-2(1)	-5(1)
S30	28(1)	51(1)	26(1)	2(1)	0(1)	-5(1)
S31	33(1)	45(1)	25(1)	2(1)	-1(1)	-5(1)
S32	28(1)	47(1)	30(1)	4(1)	1(1)	-8(1)
C33	44(2)	40(2)	28(2)	6(2)	-1(2)	-14(2)
C34	35(2)	46(2)	27(2)	-3(2)	4(2)	-12(2)
C35	40(2)	46(3)	33(2)	-9(2)	10(2)	-18(2)
C36	41(2)	33(2)	33(2)	5(2)	-2(2)	-14(2)
S37	30(1)	49(1)	37(1)	6(1)	7(1)	-6(1)
S38	30(1)	47(1)	28(1)	6(1)	-3(1)	-4(1)
Fe	29(1)	31(1)	24(1)	-1(1)	2(1)	-12(1)
N41	53(2)	39(2)	40(2)	-2(2)	-1(2)	-11(2)
N42	48(2)	61(3)	41(2)	-8(2)	2(2)	-31(2)
N43	42(2)	48(2)	37(2)	-5(2)	11(2)	-20(2)
C41	36(2)	39(2)	25(2)	-5(2)	6(2)	-17(2)
C42	35(2)	38(2)	29(2)	-2(2)	6(2)	-17(2)
C43	29(2)	27(2)	31(2)	-2(2)	-1(2)	-8(2)
Cl1	74(1)	83(1)	56(1)	-12(1)	-10(1)	-18(1)
Cl2	88(1)	66(1)	106(1)	-20(1)	-10(1)	-18(1)
C44	52(3)	59(3)	58(3)	-2(2)	-14(2)	-17(2)

Appendix Table D-5: Hydrogen coordinates (x 10^4) and isotropic displacement parameters ($Å^2$ x 10^3) for **15**.

Atom	x	y	z	$U_{(eq)}$
H13A	3389(5)	21014(4)	-8034(2)	49
H13B	4191(5)	21592(4)	-7580(2)	49
H14A	1253(4)	17008(4)	-856(2)	46
H14B	1972(4)	15827(4)	-1289(2)	46
H15A	5864(5)	19603(4)	-7916(2)	52
H15B	4870(5)	18842(4)	-7482(2)	52
H16A	3762(4)	16292(4)	-727(2)	46
H16B	3306(4)	17677(4)	-1266(2)	46
H33A	-1051(4)	26701(4)	-8884(2)	48
H33B	-395(4)	27005(4)	-8237(2)	48
H34A	-2502(4)	23300(4)	-2029(2)	45
H34B	-3551(4)	22505(4)	-1733(2)	45
H35A	1371(4)	25203(4)	-8762(2)	47
H35B	350(4)	24377(4)	-8474(2)	47
H36A	-1924(4)	20752(4)	-2342(2)	45
H36B	-1177(4)	20936(4)	-1684(2)	45
H44A	5632(5)	11824(5)	118(3)	69
H44B	4275(5)	11425(5)	463(3)	69

LIST OF REFERENCES

(1) Kittel, C. *Introduction to Solid State Physics;* 6th ed.; John Wiley & Sons: New York, 1986.

(2) Rouxel, J. *Acc. Chem. Res.* **1992**, *25*, 328-336.

(3) *The Physics and Chemistry of Organic Superconductors*; Springer: Berlin, 1990; Vol. 51.

(4) Williams, J. M.; Ferraro, J. R.; Thorn, R. J.; Carlson, K. D.; Geiser, U.; Wang, H. H.; Kini, A. M.; Whangbo, M.-H. *Organic Superconductors*; Prentice-Hall: Englewood Cliffs, NJ, 1992, 400 pp.

(5) Morosin, B.; Graeber, E. J. *Acta Cryst.* **1967**, *23*, 766.

(6) Heger, G.; Deiseroth, H. J.; Schulz, H. *Acta Cryst.* **1978**, *B34*, 725-731.

(7) Carlin, R. L. *Magnetochemistry;* 1st ed.; Springer-Verlag: Berlin, 1986.

(8) Wagner, H. Ph.D. Thesis, Karlruhe, 1974.

(9) Bonner, J. C.; Fisher, M. E. *Phys. Rev.* **1964**, *135*, 640-658.

(10) Weng, C. Y. Ph.D. Thesis, Carnegie Mellon University, 1968.

(11) de Jongh, L. J.; Miedema, A. R. *Adv. Phys.* **1974**, *24*, 1-260.

(12) Haldane, F. D. M. *Phys. Lett.* **1983**, *93A*, 464-468.

(13) Haldane, F. D. M. *Phys. Rev. Lett.* **1983**, *50*, 1153-1156.

(14) Renard, J. P.; Verdaguer, M.; Regnault, L. P.; Erkelens, W. A. C.; Rossat-Mignod; Ribas, J.; Stirling, W. G.; Vettier, C. *J. Appl. Phys.* **1988**, *63*, 3538-3542.

(15) Renard, J. P.; Regnault, L. P.; Verdaguer, M. *Journal De Physique* **1988**, *C8*, 1425-1429.

(16) Takeuchi, T.; Hori, H.; Date, M.; Yosida, T.; Katsumata, K.; Renard, J. P.; Gadet, V.; Verdaguer, M. *J. Magn. Magn. Mater.* **1992**, *104*, 813-814.

(17) Avenel, O.; Xu, J.; Xia, J. S.; Xu, M.-F.; Andraka, B.; Lang, T.; Moyland, P. L.; Ni, W.; Signore, J. C.; van Woerkens, C. M. C. M.; Adams, E. D.; Ihas, G. G.; Meisel, M. W.; Nagler, S. E.; Sullivan, N. S.; Takano, Y.; Talham, D. R.; Goto, T.; Fujiwara, N. *Phys. Rev. B* **1992**, *46*, 8655-8658.

(18) Katsumata, K.; Hori, H.; Takeuchi, T.; Date, M.; Yamagishi, A.; Renard, J. P. *Phys. Rev. Lett.* **1989**, *63*, 86-88.

(19) Takeuchi, T.; Ono, M.; Hori, H.; Yosida, T.; Yamagishi, A.; Date, M. *J. Phys. Soc. Jpn.* **1992**, *61*, 3255-3261.

(20) Meyer, A.; Gleizes, A.; Girerd, J. J.; Verdaguer, M.; Kahn, O. *Inorg. Chem.* **1982**, *21*, 1729-1739.

(21) Renard, J. P.; Gadet, V.; Regnault, L. P.; Verdaguer, M. *J. Magn. Magn. Mater.* **1990**, *90*, 213-216.

(22) Chou, L.-K.; Abboud, K. A.; Talham, D. R.; Kim, W. W.; Meisel, M. W. *Physica B* **1994**, *194-196*, 311-312.

(23) Chou, L.-K.; Abboud, K. A.; Talham, D. R.; Kim, W. W.; Meisel, M. W. *Chem. Mater.* **1994**, *6*, 2051-2055.

(24) Date, M.; Kindo, K. *Phys. Rev. Lett.* **1990**, *65*, 1659-1662.

(25) Nightingale, M. P.; Blote, H. W. J. *Phys. Rev. B* **1986**, *33*, 659.

(26) Granroth, G. E.; Meisel, M. W.; Chaparala, M.; Ward, B. H.; Talham, D. R. *Phys. Rev. Lett* **1996**, *77*, 1616; and references therein.

(27) Cowan, D. O.; Wiygul, F. M. *Chem. Eng. News* **1986**, 28-45.

(28) Torrance, J. B. *Acc. Chem. Res.* **1979**, *12*, 79-86.

(29) Melby, L. R.; Harder, R. J.; Hertler, W. R.; Mahler, W.; Benson, R. E.; Mochel, W. E. *J. Am. Chem. Soc.* **1962**, *84*, 3374.

(30) Cooper, W. F.; Kenny, N. C.; Edmonds, J. W.; Nagel, A.; Wudl, F.; Coppens, P. *J. Chem. Soc., Chem. Commun.* **1971**, 889.

(31) Wudl, F.; Wobschall, D.; Hufnagel, E. J. *J. Am. Chem. Soc.* **1972**, *94*, 670-672.

(32) Ferraris, J.; Cowan, D. O.; Jr., W., V. V.; Perlstein, J. H. *J. Am. Chem. Soc.* **1973**, *95*, 948.

(33) Bechgaard, K.; Cowan, D. O.; Bloch, A. N. *J. Chem. Soc., Chem. Commun.* **1974**, 937-938.

(34) Bechgaard, K.; Jacobsen, C. S.; Mortensen, K.; Pedersen, M. J.; Thorup, N. *Solid State Commun.* **1980**, *33*, 1119-1125.

(35) Jerome, D.; Mazaud, A.; Ribault, M.; Bechgaard, K. *Journal de Physique Lettres* **1980**, *41*, L95-L98.

(36) Bechgaard, K.; Carneiro, K.; Rasmussen, F. G.; Olsen, K.; Rindorf, G.; Jacobsen, C. S.; Pederson, H. J.; Scott, J. E. *J. Am. Chem. Soc.* **1981**, *103*, 2440.

(37) Jerome, D. *Science* **1991**, *252*, 1509-1514.

(38) Ferraro, J. R.; Williams, J. M. *Introduction to Synthetic Electrical Conductors*; Academic Press: San Diego, 1987.

(39) Mizuno, M.; Garito, A. F.; Cava, M. P. *J. Chem. Soc., Chem. Commun.* **1978**, 18-19.

(40) Parkin, S. S. P.; Engler, E. M.; Schumaker, R. R.; Lagier, R.; Lee, V. Y.; Scott, J. C.; Greene, R. L. *Phys. Rev. Lett.* **1983**, *50*, 270-273.

(41) Williams, J. M.; Schultz, A. J.; Geiser, U.; Carlson, K. D.; Kini, A. M.; Wang, H. H.; Kwok, W.-K.; Whangbo, M.-H.; Schirber, J. E. *Science* **1991**, *252*, 1501-1508.

(42) Obertelli, S. D.; Friend, R. H.; Talham, D. R.; Kurmoo, M.; Day, P. *J. Phys.: Condens. Matter 1* **1989**, 5671-5680.

(43) Williams, J. M.; Kini, A. M.; Wang, H. H.; Carlson, K. D.; Geiser, U.; Montgomery, L. K.; Pyrka, G. J.; Watkins, D. M.; Kommers, J. M.; Boryschuk, S. J.; Strieby Crouch, A. V.; Kwok, W. K.; Schirber, J. E.; Overmyer, D. L.; Jung, D.; Whangbo, M. H. *Inorg. Chem.* **1990**, *29*, 3272-3274.

(44) Kurmoo, M.; Graham, A. W.; Day, P.; Coles, S. J.; Hursthouse, M. B.; Caulfield, J. L.; Singleton, J.; Pratt, F. L.; Hayes, W.; Ducasse, L.; Guionneau, P. *J. Am. Chem. Soc.* **1995**, *117*, 12209-12217.

(45) Chou, L. K.; Quijada, M. A.; Clevenger, M. B.; de Oliveira, G. F.; Abboud, K. A.; Tanner, D. B.; Talham, D. R. *Chem. Mater.* **1995**, *7*, 530-534.

(46) Ward, B. H.; Granroth, G. E.; Abboud, K. A.; Meisel, M. W.; Talham, D. R. *submitted to Chemistry of Materials* **1997**.

(47) Kawamoto, A.; Tanaka, J.; Tanaka, M. *Acta Cryst.* **1987**, *C43*, 205-207.

(48) Mori, T.; Inokuchi, H. *Solid State Commun.* **1987**, *62*, 525-529.

(49) Mori, T.; Wang, P.; Imaeda, K.; Enoki, T.; Inokuchi, H. *Solid State Commun.* **1987**, *64*, 733-737.

(50) Abboud, K. A.; Chou, L. K.; Clevenger, M. B.; de Oliveira, G. F.; Talham, D. R. *Acta. Cryst.* **1995**, *C51*, 2356-2362.

(51) Kobayashi, H.; Kobayashi, A.; Sasaki, Y.; Saito, G.; Inokuchi, H. *Chem. Lett.* **1984**, 183-186.

(52) Porter, L. C.; Wang, H. H.; Beno, M. A.; Carlson, K. D.; Pipan, C. M.; Proksch, R. B.; Williams, J. M. *Solid State Commun.* **1987**, *64*, 387-390.

(53) Mallah, T.; Hollis, C.; Bott, S.; Kurmoo, M.; Day, P.; Allan, M.; Friend, R. H. *J. Chem. Soc. Dalton Trans.* **1990**, 859-865.

(54) Parkin, S. S. P.; Engler, E. M.; Lee, V. Y.; Schumaker, R. R. *Mol. Cryst. Liq. Cryst.* **1985**, *119*, 375-387.

(55) Bu, X.; Cisarova, I.; Coppens, P. *Acta Cryst.* **1992**, *C48*, 1558-1560.

(56) Bu, X.; Cisarova, I.; Coppens, P. *Acta Cryst.* **1992**, *C48*, 1562-1563.

(57) Frere, P.; Carlier, R.; Boubekeur, K.; Gorgues, A.; Roncali, J.; Tallec, A.; Jubault, M.; Batail, P. *J. Chem. Soc., Chem. Commun.* **1994**, 2071.

(58) Mori, T.; Inokuchi, H. *Chem. Lett.* **1986**, 2069-2072.

(59) Geiser, U.; Wang, H.-H.; Budz, S. M.; Lowry, M. J.; Williams, J. M.; Ren, J.; Whangbo, M.-H. *Inorg. Chem.* **1990**, *29*, 1611-1614.

(60) Geiser, U.; Wang, H. H.; Gerdom, L. E.; Firestone, M. A.; Sowa, L. M.; Williams, J. M. *J. Am. Chem. Soc.* **1985**, *107*, 8305-8307.

(61) Kobayashi, H.; Kato, R.; Kobayashi, A.; Sasaki, Y. *Chem. Lett.* **1985**, 191-194.

(62) Mallah, T.; Hollis, C.; Bott, S.; Day, P.; Kurmoo, M. *Synthetic Metals* **1988**, *27*, A381-A386.

(63) Liu, H.; Chou, L.; Abboud, K. A.; Ward, B. H.; Fanucci, G. E.; Granroth, G. E.; Canadell, E.; Meisel, M. W.; Talham, D. R.; Tanner, D. B. *Chem. Mater.* **1997**, *9*, 1865-1877.

(64) Suzuki, T.; Yamochi, H.; Srdanov, G.; Hinklemann, K.; Wudl, F. *J. Am. Chem. Soc.* **1989**, *111*, 3108-3109.

(65) Suzuki, T.; Yamochi, H.; Isotalo, H.; Fite, C.; Kasmai, H.; Liou, K.; Srdanov, G.; Wudl, F. *Synthetic Metals* **1991**, *41-43*, 2225-2228.

(66) Horiuchi, S.; Yamochi, H.; Saito, G.; Sakaguchi, K.; Kusunoki, M. *J. Am. Chem. Soc.* **1996**, *118*, 8604-8622.

(67) Yamochi, H.; Horiuchi, S.; Saito, G.; Kusunoki, M.; Sakaguchi, K.; Kikuchi, T.; Sato, S. *Synthetic Metals* **1993**, *55-57*, 2096-2101.

(68) Bellitto, C.; Regnault, L. P.; Renard, J. P. *J. Magn. Magn. Mater.* **1991**, *102*, 116.

(69) Hagiwara, M.; Katsumata, K. *J. Magn. Magn. Mater.* **1995**, *140-144*, 1665-1666.

(70) Goodwin, H. A.; Sylva, R. N. *Aust. J. Chem.* **1965**, *18*, 1743-1749.

(71) Goodwin, H. A.; Sylva, R. N. *Aust. J. Chem.* **1967**, *20*, 629-637.

(72) Perlepes, S. P.; Blackman, A. G.; Huffman, J. C.; Christou, G. *Inorg. Chem.* **1991**, *30*, 1665-1668.

(73) Lis, T. *Acta Cryst.* **1980**, *B36*, 2042-2046.

(74) Sheldrick, G. M. *SHELXTL5*; Siemens Analytical X-ray Instruments Incoporated: Madison, 1995.

(75) Kennedy, B. J.; Murray, K. S. *Inorg. Chem.* **1985**, *24*, 1552-1557.

(76) Hiller, W.; Strähle, J.; Datz, A.; Hanack, M.; Hatfield, W. E.; ter Haar, L. W.; Gütlich, P. *J. Am. Chem. Soc.* **1984**, *106*, 329-335.

(77) Poole Jr., C. P. *Electron Spin Resonance*; Interscience: New York, 1967.

(78) Hagiwara, M.; Katsumata, K.; Affleck, I.; Halperin, B. I.; Renard, J. P. *Phys. Rev. Lett.* **1990**, *65*, 3181-3184.

(79) Stults, B. R.; Marianelli, R. S.; Day, V. W. *Inorg. Chem.* **1975**, *14*, 722-730.

(80) Stults, B. R.; Day, R. O.; Marianelli, R. S.; Day, V. W. *Inorg. Chem.* **1979**, *18*, 1847-1852.

(81) Bonadies, J. A.; Kirk, M. L.; Lah, M. S.; Kessissoglou, D. P.; Hatfield, W. E.; Pecoraro, V. L. *Inorg. Chem.* **1989**, *28*, 2037-2044.

(82) Williams, J. M.; Wang, H. H.; Emge, T. J.; Geiser, U.; Beno, M. A.; Leung, P. C. W.; Carlson, K. D.; Thorn, R. J.; Schultz, A. J.; Whangbo, M. *Prog. Inorg. Chem.* **1987**, *35*, 51-218.

(83) *Organic Superconductivity*; Kresin, V. Z.; Little, W. A., Ed.; Plenum Press: New York, 1990, pp 386.

(84) Adrian, F. J.; Cowan, D. O. *Chem. Eng. News* **1992**, 24-41.

(85) Wang, H. H.; Geiser, U.; Williams, J. M.; Carlson, K. D.; Kini, A. M.; Mason, J. M.; Perry, J. T.; Charlier, H. A.; Crouch, A. V. S.; Heindl, J. E.; Lathrop, M. W.; Love, B. J.; Watkins, D. M.; Yaconi, G. A. *Chem.Mater.* **1992**, *4*, 247-249.

(86) Abboud, K. A.; Clevenger, M. B.; de Oliveira, G. F.; Talham, D. R. *J. Chem. Soc., Chem. Commun.* **1993**, 1560-1562.

(87) Beno, M. A.; Firestone, M. A.; Leung, P. C. W.; Sowa, L. M.; Wang, H. H.; Williams, J. M.; Whangbo, M. *Solid State Commun.* **1986**, *57*, 735-739.

(88) Ugawa, A.; Yakushi, K.; Kuroda, H.; Kawamoto, A.; Tanaka, J. *Synthetic Metals* **1988**, *22*, 305-315.

(89) Larsen, J.; Lenoir, C. *Synthesis* **1988**, *2*, 134.

(90) Parker, I. D.; Friend, R. H.; Kurmoo, M.; Day, P. *J. Phys.: Condens. Matter 1* **1989**, 5681-5688.

(91) Schroeder, L. W.; Ibers, J. A. *Inorg. Chem.* **1968**, *7*, 594-599.

(92) Kuchen, W.; Mootz, D.; Somberg, H.; Wunderlich, H.; Wussow, H. *Angew. Chem. Int. Ed. Engl.* **1978**, *17*, 869-870.

(93) Atwood, J. L.; Bott, S. G.; Coleman, A. W.; Robinson, K. D.; Whetstone, S. B.; Means, C. M. *J. Am. Chem. Soc.* **1987**, *109*, 8100-8101.

(94) Atwood, J. L.; Bott, S. G.; Means, C. M.; Coleman, A. W.; Zhang, H.; May, M. T. *Inorg. Chem.* **1990**, *29*, 467-470.

(95) Kobayashi, H.; Kato, R.; Mori, T.; Kobayashi, A.; Sasaki, Y.; Saito, G.; Enoki, T.; Inokuchi, H. *Chem. Lett.* **1984**, 179-182.

(96) Beno, M. A.; Geiser, U.; Kostka, K. L.; Wang, H. H.; Webb, K. S.; Firestone, M. A.; Carlson, K. D.; Nunez, L.; Whangbo, M.; Williams, J. M. *Inorg. Chem.* **1987**, 1912-1917.

(97) Mori, T.; Inokuchi, H. *Bulletin of the Chemical Society of Japan* **1988**, *61*, 591-593.

(98) Umland, T. C.; Allie, S.; Kuhlmann, T.; Coppens, P. *J. Phys. Chem.* **1988**, *92*, 6456-6460.

(99) Day, P.; Kurmoo, M.; Mallah, T.; Marsden, I. R.; Friend, R. H.; Pratt, F. L.; Hayes, W.; Chasseau, D.; Gaultier, J.; Bravic, G.; Ducasse, L. *J. Am. Chem. Soc.* **1992**, *114*, 10722-10729.

(100) Kurmoo, M.; Talham, D. R.; Day, P.; Howard, J. A. K.; Stringer, A. M.; Obertelli, D. S.; Friend, R. H. *Synthetic Metals* **1988**, *22*, 415-418.

(101) Lines, M. E. *J. Phys. Chem. Solids* **1970**, *31*, 101-116.

(102) Kato, R.; Kobayashi, H.; Kobayashi, A.; Sasaki, Y. *Chem. Lett.* **1985**, 1943-1946.

(103) Wudl, F.; Yamochi, H.; Suzuki, T.; Isotalo, H.; Fite, C.; Kasmai, H.; Liou, K.; Srdanov, G. *J. Am. Chem. Soc.* **1990**, *112*, 2461-2462.

(104) Beno, M. A.; Wang, H. H.; Kini, A. M.; Carlson, K. D.; Geiser, U.; Kwok, W. K.; Thompson, J. E.; Williams, J. M.; Ren, J.; Whangbo, M. H. *Inorg. Chem.* **1990**, *29*, 1599-1601.

(105) Beno, M. A.; Wang, H. H.; Carlson, K. D.; Kini, A. M.; Frankenbach, G. M.; Ferraro, J. R.; Larson, N.; McCabe, G. D.; Thompson, J.; Purnama, C.; Vashon, M.; Williams, J. M.; Jung, D.; Whangbo, M. *Mol. Cryst. Liq. Cryst.* **1990**, *181*, 145-159.

(106) Kahlich, S.; Schweitzer, D.; Heinen, I.; Lan, S. E.; Nuber, B.; Keller, H. J.; Winzer, K.; Helberg, H. W. *Solid State Commun.* **1991**, *80*, 191-195.

(107) Zhilyaeva, E. I.; Lyubovskaya, R. N.; Torunova, S. A.; Konovalikhin, S. V.; Dyachenko, O. A.; Lyubovskii, R. B. *Synthetic Metals* **1996**, *80*, 91-93.

(108) Zhilyaeva, E. I.; Torunova, S. A.; Lyubovskaya, R. N.; Konovalikhin, S. V.; Dyachenko, O. A.; Lyubovskii, R. B.; Pesotskii, S. I. *Synthetic Metals* **1996**, *83*, 7-11.

(109) Subrayan, R. P.; Francis, A. H.; Kampf, J. W.; Rasmussen, P. G. *Chem. Mater.* **1995**, *7*, 2213-2216.

(110) Granroth, G. E. Ph.D. Dissertation, University of Florida, 1997.

(111) Crabtree, G. W.; Carlson, K. D.; Hall, L. N.; Copps, P. T.; Wang, H. H.; Emge, T. J.; Beno, M. A.; Williams, J. M. *Phys. Rev. B* **1984**, *30*, 2958.

(112) Signore, P. J. C.; Andraka, B.; Meisel, M. W.; E., B. S.; Fisk, Z.; Giorgi, A. L.; Smith, J. L.; Gross-Alltag, F.; Schuberth, E. A.; Menovsky, A. A. *Phys. Rev. B* **1995**, *52*, 4446-4461.

(113) Laukhin, V. N.; Buravov, L. I.; Khomenko, A. G.; Kushch, N. D.; Schegolev, A. I.; Yagubskii, E. B. *Synthetic Metals* **1993**, *55-57*, 2877-2882.

(114) Kahlich, S.; Schweitzer, D.; Rovira, C.; Paradis, J. A.; Whangbo, M.-H.; Heinen, I.; Keller, H. J.; Nuber, B.; Bele, P.; Brunner, H.; Shibaeva, R. P. *Z. Phys. B* **1994**, *94*, 39-47.

(115) Yamochi, H.; Horiuchi, S. *Phosphorous, Sulfur, Silicon, and Related Elements* **1992**, *67*, 305.

(116) Dyson, F. J. *Phys. Rev.* **1955**, *98*, 349-359.

(117) Edmonds, R. N.; Harrison, M. R.; Edwards, P. P. *Ann. Rep. Prog. Chem.* **1985**, *82*, 265-309.

(118) Chapman, A. C.; Rhodes, P.; Seymour, E. F. W. *Proc. Phys. Soc.* **1957**, *B70*, 345-360.

(119) Venturini, E. L.; Azevedo, L. J.; Schirber, J. E.; Williams, J. M.; Wang, H. H. *Phys. Rev. B* **1985**, *32*, 2819-2823.

(120) Talham, D. R.; Kurmoo, M.; Day, P.; Obertelli, D. S.; Parker, I. D.; Friend, R. H. *J. Phys. C: Solid State Phys.* **1986**, *19*, L383-L388.

(121) Kinoshita, N.; Tokumoto, M.; Anzai, H. *J. Phys. Soc. Jpn.* **1990**, *59*, 3410-3411.

(122) Oshima, M.; Mori, H.; Saito, G.; Oshima, K. In *The Physics and Chemistry of Organic Superconductors*; G. Saito and S. Kagoshima, Ed.; Springer-Verlag: Berlin, 1990; Vol. 51; pp 257-261.

(123) Kinoshita, N.; Tokumoto, M.; Anzai, H. *J. Phys. Soc. Jpn.* **1991**, *60*, 2131-2134.

(124) Sugano, T.; Saito, G.; Kinoshita, M. *Phys. Rev. B* **1986**, *34*, 117-125.

(125) Drago, R. S. *Physical Methods in Chemistry*; W. B. Saunders Co.: Philadelphia, 1977.

(126) Ouahab, L. *Chem. Mater.* **1997**, *9*, 1909-1926.

(127) Kobayashi, H.; Tomita, H.; Naito, T.; Kobayashi, H.; Sakai, F.; Watanabe, T.; Cassoux, P. *J. Am. Chem. Soc.* **1996**, *118*, 368.

(128) Le Magueres, P.; Ouahab, L.; Conan, N.; Gomez-Garcia, C. J.; Delhaes, P.; Even, J.; Bertault, M. *Solid State Commun.* **1996**, *97*, 27-32.

(129) Le Magueres, P.; Ouahab, L.; Briard, P.; Even, J.; Bertault, M.; Toupet, L.; Ramos, J.; Gomez-Garcia, C. J.; Delhaes, P.; Mallah, T. *Synthetic Metals* **1997**, *86*, 1859.

(130) Ugawa, A.; Yakushi, K.; Kuroda, H.; Kawamoto, A.; Tanaka, J. *Chem. Lett.* **1986**, 1875-1878.

(131) Mori, T.; Sakai, F.; Saito, G.; Inokuchi, H. *Chem. Lett.* **1986**, 1037-1040.

(132) Kurmoo, M.; Talham, D. R.; Day, P.; Parker, I. D.; Friend, R. H.; Stringer, A. M.; Howard, J. A. K. *Solid State Commun.* **1987**, *61*, 459-464.

(133) Kobayashi, H.; Kobayashi, A.; Sasaki, Y.; Saito, G. *Bull. Chem. Soc. Jpn.* **1986**, *59*, 301-302.

(134) Kobayashi, H.; Kobayashi, A.; Sasaki, Y.; Saito, G.; Enoki, T.; Inokuchi, H. *J. Am. Chem. Soc.* **1983**, *105*, 297-298.

(135) Sugano, T.; Yakushi, K.; Kuroda, H. *Bull. Chem. Soc. Jpn.* **1978**, *51*, 1041-1046.

BIOGRAPHICAL SKETCH

Brian Howard Ward was born in Orlando, Florida on July 18, 1971, to John and Dorothy Ward. From the ages of 3 to 6 years old, Brian moved with his parents to several cities: Kansas City, MO, Ft. Worth, TX, and Fairfax, VA. In 1977, he and his parents moved back to Orlando, FL, where he graduated from Boone High School in 1988. In the Fall of 1988 he enrolled at Florida State University. Here Brian was a varsity cheerleader for the FSU Seminoles and received a Bachelor of Science degree in chemistry in April 1992.

Later that year, in August, he came to the University of Florida in Gainesville to work toward a Ph.D. in chemistry under the supervision of Dr. Daniel R. Talham. During his five years at the University of Florida, no one was able to convince him of becoming a Gator fan. Upon completing his doctorate, Brian plans to pursue a career of industrial research.

I certify that I have read this study and that in my opinion it conforms to acceptable standards of scholarly presentation and is fully adequate, in scope and quality, as a dissertation for the degree of Doctor of Philosophy.

Daniel R. Talham, Chairman
Associate Professor of Chemistry

I certify that I have read this study and that in my opinion it conforms to acceptable standards of scholarly presentation and is fully adequate, in scope and quality, as a dissertation for the degree of Doctor of Philosophy.

Khalil A. Abboud
Associate Scientist of Chemistry

I certify that I have read this study and that in my opinion it conforms to acceptable standards of scholarly presentation and is fully adequate, in scope and quality, as a dissertation for the degree of Doctor of Philosophy.

Mark W. Meisel
Associate Professor of Physics

I certify that I have read this study and that in my opinion it conforms to acceptable standards of scholarly presentation and is fully adequate, in scope and quality, as a dissertation for the degree of Doctor of Philosophy.

Gus J. Palenik
Professor of Chemistry

I certify that I have read this study and that in my opinion it conforms to acceptable standards of scholarly presentation and is fully adequate, in scope and quality, as a dissertation for the degree of Doctor of Philosophy.

John R. Reynolds
Professor of Chemistry

This dissertation was submitted to the Graduate Faculty of the Department of Chemistry in the College of Liberal Arts and Sciences and to the Graduate School and was accepted as partial fulfillment of the requirements for the degree of Doctor of Philosophy.

December, 1997

Dean, Graduate School